Table 10.1 Some Precipitation-Hardening Systems

Base Metal	Alloy	Sequence of Precipitates
Al	Al–Ag	Zones (spheres) —— γ' (plates) —— γ(Ag,Al)
	Al–Cu	Zones (disks) —— θ'' (disks) —— θ' —— θ ($CuAl_2$)
	Al–Zn–Mg	Zones (spheres) —— M′ (plates) —— ($MgZn_2$)
	Al–Mg–Si	Zones (rods) —— β' —— (Mg_2Si)
	Al–Mg–Cu	Zones (rods or spheres) —— S′ —— S(Al_2CuMg)
	Al–Li–Cu	Zones —— θ'' ——> θ' ——> θ ($CuAl_2$) Ti($CuAl_2Li$) δ' ——> δ (AlLi)
Cu	Cu–Be	Zones (disks) —— γ' —— γ (CuBe)
	Cu–Co	Zones (spheres) —— β
Fe	Fe–C	ε-Carbide (disks) —— Fe_3C(“laths”)
	Fe–N	α'' (disks) —— Fe_4N
Ni	Ni–Cr–Ti–Al	γ' (cubes) —— γ(Ni_2Ti)

general aging sequence as follows:

$$\text{supersaturated solid solution} \rightarrow \text{transition structures} \rightarrow \text{aged phase.}$$

In the initial stages of the aging treatment, zones that are coherent with the matrix appear. These zones are nothing but clusters of solute atoms on certain crystallographic planes of the matrix. In the case of aluminum–copper, the zones are a clustering of copper atoms on [100] planes of aluminum. The zones are transition structuring and are referred to as *Guinier–Preston zones*, or *GP zones*, in honor of the two researchers who first discovered them. We call them zones rather than precipitates in order to emphasize the fact the zones represent a small clustering of solute atoms that has not yet taken the form of precipitate particles. The GP zones are very small and have a very small lattice mismatch with the aluminum matrix. Thus, they are coherent with the matrix; that is, the lattice planes cross the interface in a continuous manner. Such coherent interfaces have very low energies, but there are small elastic coherency strains in the matrix. As these coherency strains grow, the elastic energy associated with them is reduced by the formation of semicoherent zones where dislocations form at the interface to take up the misfit strain. Further growth of the semicoherent zones, or precipitates, results in a complete loss of coherency: An incoherent interface forms between the precipitate and the matrix.

The nature of precipitate/matrix interface produced during the aging treatment can be coherent, semicoherent, or incoherent (Figure 10.15). Coherency signifies that there exists a one-to-one correspondence between the precipitate lattice and that of the matrix.

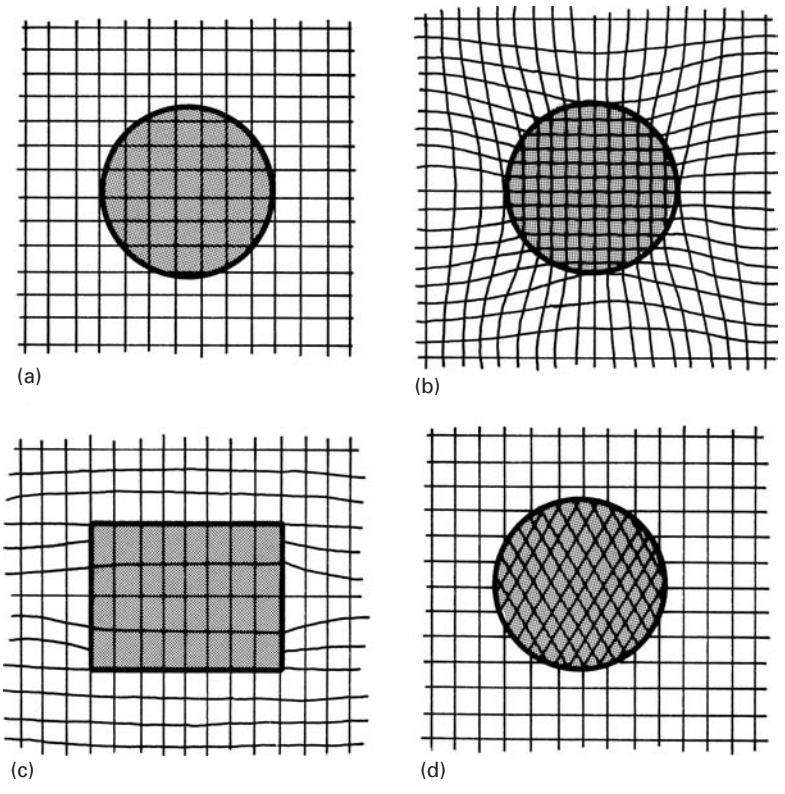

Fig. 10.15 Different crystallographic relationships between matrix and second phase. (a) Complete coherency. (b) Coherency with strained, but continuous, lattice planes across the boundary. (c) Semicoherent, partial continuity of lattice planes across the interface. (d) Incoherent equilibrium precipitate, θ; no continuity of lattice planes across the interface.

Fig. 10.16 Interfacial dislocations formed in a semicoherent precipitate. (From G. C. Weatherly and R. B. Nicholson, *Phil. Mag.*, 17 (1968), 801.)

(See Figure 10.15(a) and (b)). A semicoherent precipitate signifies that there is only a partial correspondence between the two sets of lattice planes. The lattice mismatch is accommodated by the introduction of dislocations at the noncorrespondence sites, as shown in Figure 10.15(c). Figure 10.16 shows such interfacial dislocations at semicoherent interfaces. An incoherent interface, shown in Figure 10.15(d), implies that there is no correspondence between the two lattices. Such an interface is also present in dispersion-hardened systems.

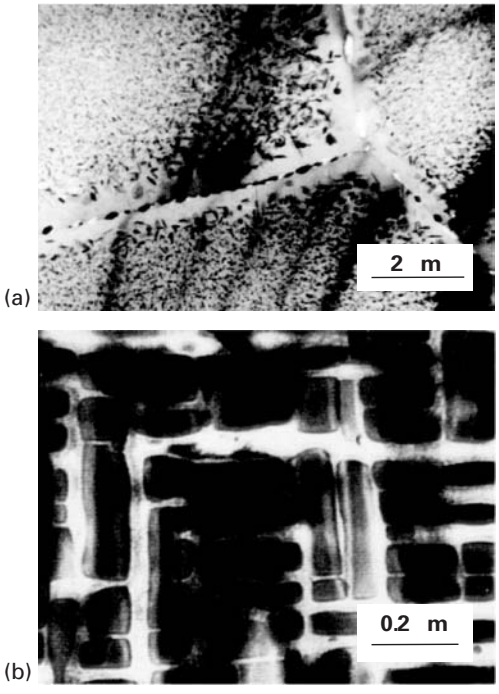

Fig. 10.17 (a) Al–Zn–Mg alloy showing precipitate-free zone along grain boundaries. (b) Spinodally decomposed Cu–Ni–Fe alloy resulting from aging within the ternary miscibility gap. The light phase is Cu rich, the dark phase, Ni–Fe rich. (Courtesy of G. Thomas.)

The shape of the aging curve (see Figure 10.12) can be explained as follows. Immediately after quenching, only solid-solution-hardening is present. As GP zones form, hardness or strength increases because extra stress is needed to make dislocations shear the coherent zones. The hardness increases as the size of the GP zones increases, making it ever more difficult for the dislocations to shear the zones. As time goes on, incoherent equilibrium precipitates start appearing, and the mechanism of Orowan bowing (see Section 10.5) of dislocations around the particles becomes operative. The peak hardness or strength is associated with a critical dispersion of coherent or semicoherent precipitates. Further aging results in an increase in the interparticle distance, and a lower strength results as dislocation bowing becomes easier.

Under certain conditions, precipitation may occur in a nonuniform manner, and often grain boundaries are favored sites. This may result in a region close to the grain boundary in which precipitation is virtually absent because the solute was used up in the formation of precipitates along the boundary. The aluminium–zinc–magnesium alloy shown in Figure 10.17(a) was used in the Comet aircraft. This TEM micrograph clearly shows the "precipitate-free zones" along both sides of the boundary, forming a rosary. The younger students might not remember this, but the British De Havilland company built the first commercial jet aircraft in 1952. Alas, after four accidents confidence in the new plane was destroyed and so was British supremacy in commercial aircraft. This costly mistake was attributed to two reasons:

(**a**) The plane used square windows, at whose corners fatigue cracks started to propagate. Square corners produce a high stress concentration. Interestingly, the U.S. Civil Aeronautics Administration (predecessor to the Federal Aviation Adminsitration, FAA) had doubts about the wisdom of using square windows and had refused to grant the Comet an air-worthiness certificate.
(**b**) The alloy and heat treatment used in the aircraft exhibited the microstructure shown in Figure 10.17(a).

Thomas and Nutting[5] showed quite clearly, using TEM, the occurrence of precipitate-free zone (PFZ) adjacent to grain boundaries, and a courser precipitate distribution adjacent to the PFZ, when compared to the surrounding matrix. This leads to intergranular corrosion and accelerates fatigue failure. One needs TEM to characterize such PFZs.

There is another mechanism of forming a second phase that does not involve nucleation and growth. It is called spinodal decomposition. It starts with fluctuations in composition that become gradually (with time) more pronounced. This eventually leads to phase separation. Spinodal decomposition is not as common as precipitation. Figure 10.17(b) shows the microstructure produced in a Cu–Ni–Fe alloy by spinodal decomposition.

Example 10.2

Dispersion-hardened materials have a stable microstructure at high temperatures, compared to precipitation-hardened materials. Is there any advantage, then, to strengthening by precipitation over that by dispersion of strong, inert particles?

Solution: In general a dispersion-hardened material, because it is very hard, can be very difficult to machine or work. A precipitation-hardened material, on the other hand, can be machined or worked before it is given the aging treatment, i.e., when it is soft. After machining, one can give the material the appropriate aging treatment to get the maximum strength and hardness.

Example 10.3

Figure E10.3 shows the Al–Mg phase diagram. For an alloy with 5% Mg by weight, calculate the Al_2Mg (β) equilibrium volume fraction of precipitate if the densities of Al and Al_2Mg are 2.7 and 2.3 g/cm^3, respectively.

Solution: Basically, we have to calculate the volume fraction of Al_2Mg at room temperature (25 °C). However, in this phase diagram, the data

[5] G. Thomas and J. Nutting, *J. Inst. Metals*, 88 (1959–60) 81; R. B. Nicholson, G. Thomas, and J. Nutting, *Acta Met.*, 8 (1960) 172.

are given to 100 °C. We assume that there is not much change between 100 °C and 25 °C. Applying the lever rule,[6] we find that the fraction of β (Al_2Mg) by weight is

$$\frac{5-1}{35-1} = 0.12.$$

Changing this into the volume fraction (divide the respective mass fraction by the density of each component) we have

$$f = \frac{0.12/2.3}{0.88/2.7 + 0.12/2.3} \left(= \frac{V_{Al_2Mg}}{V_{Al} + V_{Al_2Mg}} \right)$$
$$= 0.14 \quad \text{or} \quad 14\%.$$

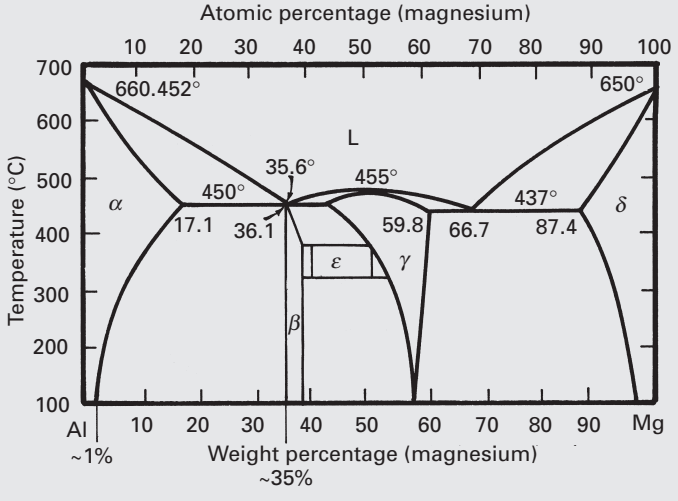

Fig. E10.3

10.5 Dislocation–Precipitate Interaction

Finely distributed precipitates present an effective barrier to the motion of dislocations. Two of the important models that explain the strengthening due to precipitates respectively involving (1) dislocations cutting through the particles in the slip plane and (2) dislocations circumnavigating around the particles in the slip plane. Depending on both the nature of the precipitate and the crystallographic relationship between the precipitate and the matrix, we can have two limiting cases:

1. *The precipitate particles are impenetrable to the dislocations*. Orowan pointed out that if a ductile matrix has second-phase particles interpenetrating the slip plane of dislocations, an additional stress

[6] The lever rule allows us to compute the relative phase amounts in a two-phase alloy. The student should consult any introductory book on materials engineering.

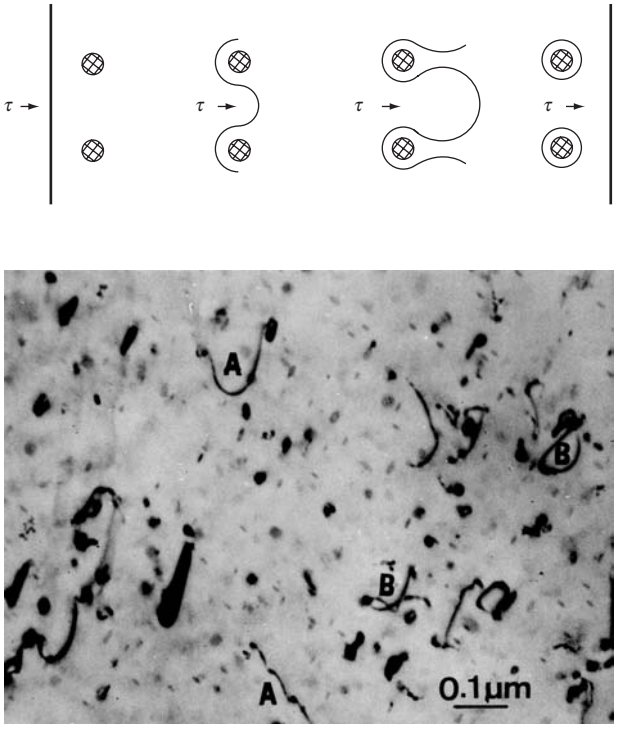

Fig. 10.18 (a) The Orowan model. (After E. Orowan, in *Internal Stresses in Metals and Alloys* (London: Institute of Metals, 1948), p. 451.) (b) Obstruction of dislocation motion by uniformly distributed nonshearing particles in an aluminum alloy (transmission electron microscope) (Courtesy of M. V. Heimendahl.)

will be necessary to make a dislocation expand between the particles. The applied stress should be sufficiently high to bend the dislocations in a roughly semicircular form between the particles. If so, the dislocations will extrude between the particles, leaving dislocation loops around them, as per the mechanism shown schematically in Figure 10.18(a). Under an applied shear stress τ, the dislocation bows in between the precipitate particles until segments of dislocation with opposite Burgers vector cancel each other out, leaving behind dislocation loops around the particle. An example of Orowan bowing is shown in a TEM in Figure 10.18(b). The material is an Al–0.2% Au alloy, solution annealed, followed by 60 hours at 200 °C and 5% plastic deformation. At points marked *A* in this figure, one can see dislocations pinned by the precipitates and Orowan bowing of dislocation segments. At point *B*, the dislocations have left the slip plane and formed prismatic dislocation loops. The dislocations in the micrograph are characteristically very short and have been severely impeded in their movement.

Now, the stress necessary to bend a dislocation to a radius r is given roughly by (see Section 4.4.5, Equation 4.22d)

$$\tau \approx Gb/2r \tag{10.4}$$

Let x be the average separation between two particles in the slip lane. Then a dislocation, under a shear stress τ, must be bent to a radius on the order of $x/2$ for it to be extruded between the particles instead

of cutting them. The shear stress to do this is given by making $r = x/2$ in Equation 10.4; that is,

$$\tau \approx \frac{Gb}{2r} = Gb/x. \tag{10.5}$$

Should the stress necessary to cause the particle shear be greater than Gb/x (rigorously speaking, $2T/bx$, where T is the dislocation line tension), the dislocation will bow between the particles rather than shear them. This, in essence, is the Orowan model of strengthening due to dispersion or incoherent precipitates. The increase in the yield stress because of the presence of particles is given by Equation 10.5, so that, as long as there is no particle shear, the total yield stress for an alloy strengthened by a dispersed phase or an incoherent precipitate is given by

$$\tau_y = \tau_m + Gb/x, \tag{10.6}$$

where τ_m is the critical shear stress for matrix yielding in the absence of a precipitate. Note that more precise formulations of the Orowan stress have been made, involving more accurate expressions for the dislocation line tension T and taking into account the effect of the finite particle size on the average interparticle spacing.

Ashby[7] improved on the original Orowan equation and proposed the following form, incorporating the radius of the precipitate, r_0:

$$\tau_y = \tau_m + \left[\frac{Gb}{2.38\pi(1-\nu)^{1/2}} \ln\left(\frac{r_0}{b}\right)\right]/x.$$

The above equation predicts results that are about one-half of the Orowan equation, for $x = 10$ nm, $b = 0.3$ nm, and $\nu = 0.3$.

The comparison of the predicted Orowan–Ashby equation and experimental values for a Cu–0.74% Ni–0.14% P alloy is shown in Figure 10.19. The experimental precipitation strengthening is qualitatively similar to the Orowan equation. The strengthening decreases with precipitate size, because this corresponds to an increase in the spacing (at a constant volume fraction of 0.009). However, the actual increase in strength is only about half of the predicted value. This was attributed to microstructural effects. It is very seldom that theoretical predictions are quantitatively obeyed in materials and therefore the calculations are considered satisfactory.

2. *The precipitate particles are penetrable to dislocations*; that is, the particles are sheared by dislocations in their slip planes. If the extra stress (in addition to τ_m) necessary for particle shear is less than that for bending the dislocation between the particles ($= Gb/x$), the particles will be sheared by dislocations during yielding, and we can write

$$\tau_y < \tau_m + Gb/x.$$

[7] M. F. Ashby, in *Oxide Dispersion Strengthening*, G. S. Ansell, ed. (New York: Gordon and Breach, 1968) p. 431.

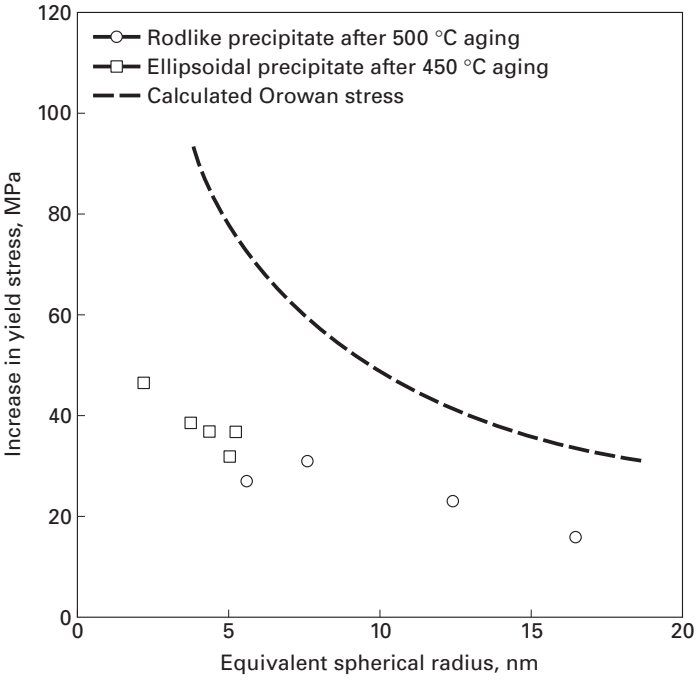

Fig. 10.19 Comparison of Orowan–Ashby calculated increase in strength in aluminium alloy with experimental results, for different partical diameters (and spacings) at a constant volume fraction *f*. (Adapted from J. Miyake and M. E. Fine, *Acta Met.*, 40 (1992) 733.)

Thus, we see that the strength of the particle and the crystallographic nature of the particle/matrix interface will determine whether dislocations will cut the particles. In internally oxidized alloys (e.g., Cu + SiO_2), where the obstacles to dislocation motion are small, very hard ceramic particles with a very high shear modulus and an incoherent interface, the initial flow stress is controlled by the stress necessary to extrude the dislocations between the hard and impenetrable particles, as per the Orowan mechanism. Since the shear strength of the obstacles is generally very much higher than that of the matrix, very large stresses will be required for particle shear to occur. The initial yield stress is then controlled by the interparticle spacing. Such behavior is also shown by precipitation-hardened alloys when the equilibrium precipitate is an intermetallic compound (e.g., $CuAl_2$ in the system Al–Cu). However, in the initial stages of aging, the small precipitates or zones are coherent with the matrix and thus can be sheared by dislocations. A vivid example of particle (Ni_3Al) shear by dislocation is illustrated in Figure 10.20: a Ni–19% Cr–69% Al alloy aged at 750 °C for 540 hours and strained 2%.

Consider the encounter of a dislocation such as that at *A* in Figure 10.21(a) with spherical particles (radius r_0 in the slip plane) that are interpenetrating the slip planes. Let x be the separation between particles in the slip plane. If the interface is coherent and the particles are not strong enough to support the Orowan stress, the dislocation will cut the particles (of radius r_0) in moving from position *A* to position *B*, as shown in Figure 10.21(a). The passage of a matrix dislocation, which generally will not be a slip dislocation for the precipitate,

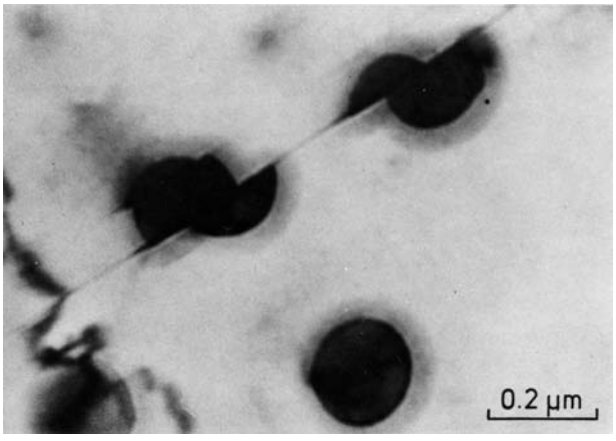

Fig. 10.20 γ'-precipitate particles sheared by dislocations in a Ni–19% Cr–69% Al alloy aged at 750 °C for 540 hours and strained 2%. The arrows indicate the two slip-plane traces (transmission electron microscopy) (Courtesy of H. Gleiter.)

will result in a faulted plane or an interface, say, of specific energy γ. Figure 10.21(b) shows schematically the formation of such an interface. The increase in the energy of the particle is $\pi r_0^2\gamma$. Then, in the absence of any thermally activated process, the stress τ_{shear} necessary to move a dislocation of length x from A to B by particle shear can be obtained as follows. A dislocation under an applied stress τ_{shear} has a force per unit length of $\tau_{\text{shear}}\ b$ on it; therefore, the dislocation of length x will have a force of $\tau_{\text{shear}}\ bx$ on it. When the dislocation moves through a distance equal to the particle diameter ($2r_0$), the work done by this force is $\tau_{\text{shear}}\ bx\ 2r_0$. This work must equal the surface energy of the interface created by cutting of the particle, viz., $\pi r_0^2\gamma$. Thus, we can write

$$\tau_{\text{shear}} bx\ 2r_0 = \pi r_0^2\gamma,$$

or

$$\tau_{\text{shear}} = \pi r_0\gamma/2bx. \tag{10.7a}$$

We can make an estimate of interparticle spacing as follows. The particle spacing x is shown in Figure 10.22: a simplified array of precipitates in a cubic arrangement. It is possible to express the volume fraction of precipitate as

$$f = \left(\frac{4}{3}\pi r_0^3\right)/x^3. \tag{10.7b}$$

It is assumed that each corner precipitate contributes one-eighth to the total volume; the eight corner precipitates together count as one. Expressing Equation 10.7b in terms of r_0/x, we have

$$r_0/x = [(3/4\pi)f]^{1/3}. \tag{10.7c}$$

Inserting equation 10.7c into 10.7a yields

$$\tau_{\text{shear}} = \text{constant}\ f^{1/3}.$$

Hence, the stress required to shear precipitates is a function only of the volume fraction of the particle that has been transformed. However, in the early stages of precipitation, the volume fraction

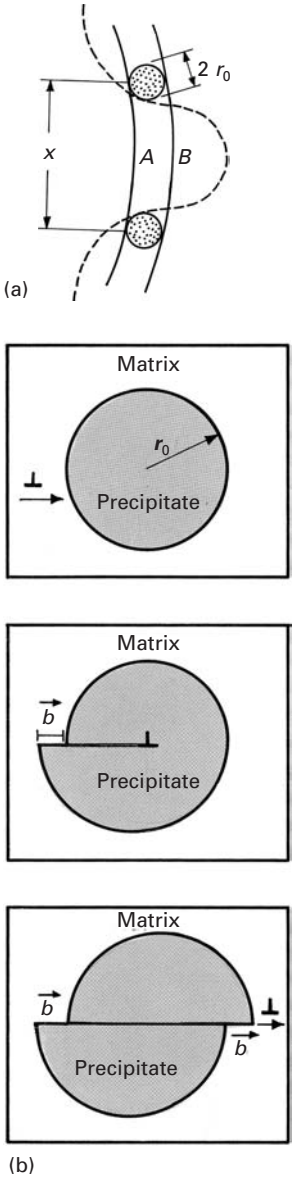

Fig. 10.21 (a) Dislocation at two successive positions A and B. (b) Dislocation shearing precipitate.

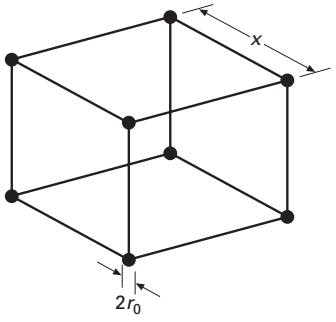

Fig. 10.22 An array of precipitates (diameter $= 2r_0$) in a cubic arrangement with the cube side $= x$.

transformed increases with time until it reaches the equilibrium value, which is determined from the phase diagram.

We discuss next the transition between the particle shear and Orowan bowing mechanisms. In the initial stages, as precipitation or aging continues, the precipitate particles increase in size and volume. As the size and amount of particles increase, more work needs to be done by the dislocation in shearing the particles. It turns out[8] that the shear strength τ of the alloy depends on the particle radius r and the particle volume fraction f according to the proportionality

$$\tau \propto \sqrt{rf}.$$

With aging of the precipitates, both r and f increase. Soon, however, a stage is reached in which the precipitate volume fraction does not increase any more. Actually, the maximum precipitate volume fraction is dictated by the alloy phase diagram. The precipitate size, however, continues to increase on further aging, because larger particles tend to grow at the expense of smaller particles. This growth is called *precipitate coarsening*. In nickel-based superalloys, the term Ostwald ripening is also used for this phenomenon. The thermodynamic driving force for precipitate coarsening is the decrease in surface area, and thus, surface energy of the precipitate with increasing size. In the initial stages of aging, both r and f increase, and the strength of the alloy increases. This, however, does not go on indefinitely, because, as precipitate coarsening occurs, the interparticle distance x increases. In fact, x becomes so large, that an alternative deformation process begins, viz., dislocation bowing or looping around the particles via the Orowan mechanism. This happens because the shear stress required to bow the dislocation between the particles is less than that required to shear them.

The stress necessary to bend a dislocation in between the particles, τ_{Orowan}, is given by Equation 10.5. If $\tau_{\text{shear}} > \tau_{\text{Orowan}}$, the dislocation will expand between the precipitate particles, and if $\tau_{\text{shear}} < \tau_{\text{Orowan}}$, the particles will be cut. Whether or not the particles will be sheared depends on r_0, the particle size, and on γ, the specific interface energy. For coherent precipitates – for example, the GP zones in Al alloys – the values of γ are expected to be on the order of the magnitude of antiphase domain boundaries, with a maximum value of about 100 mJ/m^2. Thus, from such values of γ, we can estimate that only very small particles ($2r_0 < 50$ nm) will be cut. With aging, the second-phase particles grow in size, so that the average spacing between them also increases (for a given precipitate volume fraction), and τ_{Orowan}, representing the stress necessary to bend a dislocation between particles, decreases monotonically (Figure 10.23) By contrast, the stress necessary to cut the particles increases with the particle size or aging time, because the fraction transformed increases until it reaches saturation. The figure shows the curves for dislocation bowing

[8] V. Gerold and H. Haberkorn, *Phys. Stat. Solidi*, 16 (1966) 67.

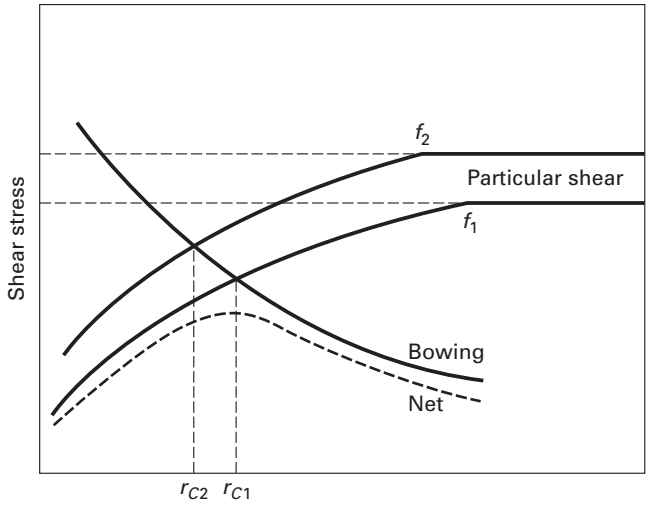

Fig. 10.23 Competition between particle shear and dislocation bowing mechanisms. f_1 and f_2 represent two volume fractions of precipitates ($f_2 > f_1$); the different volume fractions can be obtained by using different alloy compositions.

in between the particles and particle shear for two different equilibrium volume fractions, $f_2 > f_1$. These different volume fractions are obtained by changing the composition of the alloy. For instance, by increasing the Cu content of an Al–Cu alloy, we increase f. The corresponding transitions between the cutting and bowing mechanisms occur at r_{c1} and r_{c2}, respectively. The yield stress of the alloy as a function of aging time will then follow the dashed curve, a resultant of the two mechanisms. The transition between the shearing of the particle and bowing between the particles will occur at a critical radius, r_c, given by Equation 10.1, with r_c substituting for r_o.

10.6 Precipitation in Microalloyed Steels

Steels form one of the most important groups of engineering materials. Over the years, the physical and process metallurgy of steels has continually evolved to meet newer demands and challenges. The development of microalloyed steels in the second half of the twentieth century may be regarded as one of the greatest metallurgical achievements ever. This success can be attributed, in a large measure, to a clearer understanding of structure–property relations in low-carbon steels. Of course, the final product resulted from a fruitful combination of physical, mechanical, and process metallurgy. Microalloyed steels[9] have largely substituted the mild steel[10] as the basic structural material. A microalloyed steel is a low-carbon steel (0.05 to 0.2% C, 0.6 to 1.6% Mn) that contains about 0.1% of elements such as Nb,

[9] There is some confusion about the terminology in the literature. Earlier, the commonly accepted term was "high-strength low-alloy (HSLA) steels;" later the term "microalloyed steels" gained wider acceptance.

[10] Mild steel is the term used to denote a carbon steel with a carbon content between 0.1 and 0.3%.

Table 10.2 | Important Precipitates in High-Strength Low-Alloy (HSLA) Steels

Principal Element(s)	Main Precipitates
Niobium	Nb(C,N), Nb_4C_3
Vanadium	V (C,N), V_4C_3
Niobium + molybdenum	(Nb,Mo)C
Vanadium	VN
Copper + niobium	Cu,Nb(C,N)
Titanium	Ti(C,N), TiC
Aluminum	AlN

V, or Ti. Some other elements (e.g., Cu, Ni, Cr, and Mo) may also be present in small proportions (up to about 0.1%). Elements such as Al, B, O, and N have significant effects as well. Table 10.2 lists some important second phases generally encountered in high-strength low-alloy (HSLA) steels. Microalloyed steels are usually subjected to what is called a *controlled-rolling* treatment. Controlled rolling is nothing but a sequence of deformations by hot rolling at certain specific temperatures, followed by controlled cooling. The main objective of this treatment is to obtain a fine ferritic grain size. The ferritic grain size obtained after austenitization and cooling depends on the initial austenitic grain size, because ferrite nucleates preferentially at the austenite grain boundaries. The ferrite grain size also depends on the transformation temperature of the reaction austenite (γ) $\rightarrow$ ferrite (α). Lower transformation temperatures favor the nucleation rate that results in a large number of ferritic grains and, consequently, in a very small ferritic grain size (5 to 10 μm). Thus, to obtain a maximum of grain refinement, the controlled-rolling procedure modifies the hot-rolling process with a view toward exploiting the capacity of the microalloying elements so as to retard the recrystallization of the deformed austenite grains. The microalloyed additions result in the precipitation of second-phase particles during the austenitization treatment, and these particles impede the growth of the austenite grains. Hence, precipitates of, say, carbides or carbonitrides of Nb, V, or Ti can inhibit or retard the growth of these grains, resulting in a posterior ferrite grain refinement. The Hall–Petch relationship between the yield stress and the ferrite grain size (see Section 5.3) indicates the strengthening that is possible through grain size refinement. Besides grain size strengthening, some strengthening occurs due to carbide precipitation. In summary, then, during hot rolling, the fine carbide particles form in austenite and control its recrystallization. The result is a fine ferritic grain size. Secondly, carbides of Nb, V, or Ti precipitate during and soon after the $\gamma \rightarrow \alpha$ transformation and lead to a precipitation strengthening of the ferrite. Together, these two strengthening methods lead to steels with yield strengths in the range 400 to 600 MPa and with good toughness.

We saw earlier in this chapter that, in general, when the precipitates are dispersed through the matrix with very small interparticle spacing ($\leq$10 nm), the stress required to extrude the dislocations in between the particles will be very high, and dislocations will shear the particles. However, there is little evidence of such shear of precipitates in steels. The carbides, nitrides, and carbonitrides are very hard (Diamond Pyramid Hardness 2,500 to 3,000), and the presence of such hard particles in a matrix means that dislocations will be able to cut them only when they are extremely small. The critical particle size, which corresponds to a transition between the Orowan mechanism and the particle shear mechanism, decreases with an increase in the particle hardness, as shown schematically in Figure 10.24.

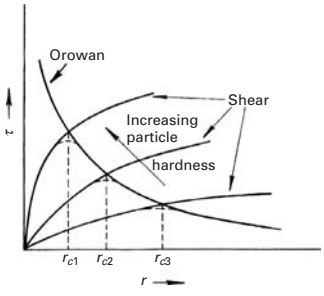

Fig. 10.24 Change in shear stress τ with increasing particle radius and hardness.

Example 10.4

Make a schematic of the precipitate volume fraction f as a function of time. Explain your diagram in terms of nucleation and growth of precipitate from a supersaturated solid solution.

Solution: The precipitates nucleate in the matrix after an initial incubation period, t_0, the time required to form stable nuclei. Following nucleation, the precipitate particles grow in size over time. Such nucleation and growth processes generally show very fast kinetics at first and then finish slowly because of the depletion of solute in the matrix. Figure E10.4 shows the desired schematic. Note the logarithmic time scale.

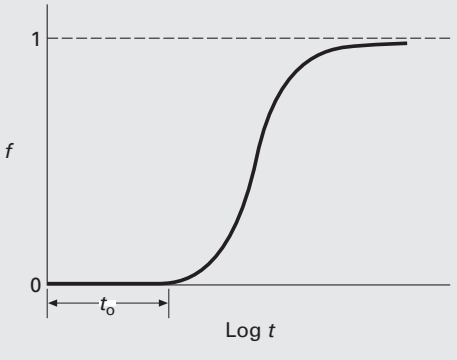

Fig. E10.4

Example 10.5

Consider a precipitation-strengthened aluminum alloy. After an appropriate heat treatment, the microstructure of the alloy consists of precipitates with a mean spacing of 0.2 μm. Compute the shear stress required for Orowan bowing of dislocations in this material.

For aluminum, we have the following data:

Lattice parameter $a_0 = 0.4$ nm,
Shear modulus = 30 GPa.

Solution: The shear stress for Orowan bowing is given by

$$\tau \approx \frac{Gb}{l} = \frac{Gb}{2r}.$$

The Burgers vector for aluminum (FCC) is

$$b = \frac{\sqrt{2}}{2}a = \frac{\sqrt{2}}{2}0.4 \text{ nm} = 0.29\,\text{nm}.$$

We can assume that a dislocation bowing around the precipitates becomes unstable when it becomes a semicircle – that is, when its radius is equal to half the interparticle spacing. Thus,

$$r = \frac{l}{2} = 0.1\,\mu\text{m},$$
$$\tau = \frac{30\,10^9 \times 0.28\,10^9}{2 \times 0.1 \times 10^{-6}} = 42.42\,\text{MPa}.$$

Example 10.6

Consider a dispersion-strengthened alloy with average interparticle spacing of λ. If N_v is the number of particles per unit volume, d is the mean particle diameter, and f is the volume fraction of particles, then show that

$$\lambda \approx d[(1/2f)^{1/3} - 1].$$

Solution: Let r be the mean radius of the particle, i.e., $2r = d$. Then the number of particles per unit volume, $N_v = f/(4\pi r^3/3)$, or $1/N_v = 4\pi r^3/3f$.

Taking the cube root of both sides, we obtain

$$1/(N_v)^{1/3} = (4\pi r^3/3f)^{1/3} = r(4\pi/3f)^{1/3} = 2r(\pi/6f)^{1/3} = d/(\pi/6f)^3.$$

Now, the interparticle spacing λ is the average center-to-center spacing between two particles, less a particle diameter, i.e.,

$$\lambda = 1/(N_v)^{1/3} - d.$$

Hence,

$$\lambda = d(\pi/6f)^{1/3} - d \approx d[(1/2f)^{1/3} - 1].$$

Example 10.7

For an alloy containing Al_2Mg precipitates, calculate the critical spacing of precipitates at which the mechanism of hardening changes from

particle shear to particle bypass. Take

$$\gamma_{Al_2Mg} = 1{,}400\,\text{mJ m}^{-2},$$
$$\text{Atomic radius (A1)} = 0.143\,\text{nm},$$
$$G_{Al} = 26.1\,\text{GPa}.$$

Solution: Assume that the precipitates are arrayed as SC (simple cubic). Therefore, the spacing x of precipitates is equal to the edge length, and for Al_2Mg in a cubic arrangement,

$$V_{Al_2Mg} = 4/3\ \pi r^3_{Al_2Mg}.$$

From Equation 10.7b, we calculate the volume fraction for precipitates:

$$f = 4/3\left(\pi r^3_{Al_2Mg}\right)/x^3.$$

Thus,

$$r_{Al_2Mg} = (3f/4\pi)^{1/3}x = 0.323x.$$

For particle shear,

$$\tau_{shear} = (\pi r_{Al_2Mg}\gamma_{Al_2Mg})/2bx.$$

For bypass,

$$\tau_{Orowan} = Gb/x.$$

The critical condition is obtained by setting $\tau_{shear} = \tau_{Orowan}$. Hence,

$$(\pi r_{Al_2Mg}\gamma_{Al_2Mg})/2bx = Gb/x.$$

Now, $r_{Al_2Mg} = 0.323x$ and $b = 2r_{Al}$ because Al is FCC. Substituting these values into the preceding equation, we get

$$(0.323\pi\gamma_{Al_2Mg}x)/4r_{Al}x = 2Gr_{Al}/x,$$

or

$$\begin{aligned} x &= \left(8Gr^2_{Al}\right)/0.323\,\pi\gamma_{Al_2Mg} \\ &= (8 \times 26.1 \times 10^9 \times 0.143 \times 10^{-9})/(0.323\pi\ 1{,}400 \times 10^{-7}/10^{-4}) \\ &= 3.0 \times 10^{-9}\,\text{m} \\ &= 3.0\,\text{nm}. \end{aligned}$$

Example 10.8

Steel is one of the most important engineering materials. Consider the different strengthening mechanisms discussed in this and earlier chapters, and make a list of different contributions to the strength of low-carbon steel.

Solution: Here is a list of the various possible contributions to the strength of steel:

1. Lattice friction stress, or the Peierls–Nabarro stress, σ_i.
2. Solid-solution strengthening, $k\sqrt{C}$, where k is a constant and C is the solute concentration.
3. Dislocation or strain hardening, $\alpha G b\sqrt{\rho}$, where α is a constant approximately equal to 0.5, G is the shear modulus, b is the Burgers vector, and ρ is the dislocation density. (This contribution is discussed in Chapter 6.)
4. Grain-size strengthening, $k_y D^{-0.5}$, where k_y is the Hall–Petch constant and D is the grain size. (This contribution is discussed in Chapter 5.)
5. A precipitation-hardening contribution if there are any precipitates present, such as carbides of iron, niobium, titanium, or vanadium.

10.7 Dual-Phase Steels

Dual-phase steels have a microstructure consisting of 5 to 20 vol.% of hard martensitic islands in a ductile ferritic matrix. The term dual-phase is a misnomer but that is the prevalent usage. Ferritic–martensitic steels would be a better name. As one would expect of such a particulate composite, the yield and ultimate tensile strength of dual-phase steels is a function of the volume fraction of martensite, the carbon content of martensite, cooling rate, etc. Frequently, depending on the cooling conditions used, there may be some retained austenite, bainite, pearlite, and new ferrite in these steels.

These steels are produced by an intercritical treatment; this involves quenching from a suitable temperature in the intercritical range between A_1 and A_3 in the Fe–C phase diagram (not shown here). In this intercritical treatment the austenite phase transforms to martensite giving us a ferrite–martensite structure instead of the conventional ferrite–pearlite microstructure. These steels are characterized by low yield strength, an absence of discontinuous yielding, and a very high strain hardening rate. These characteristics lead to a high strength component in the as-formed state. They also have excellent stretch-formability, which is exploited in automotive applications. Dual-phase steels, for a similar strength to conventional HSLA steels, offer better formability and enhanced crashworthiness. Typical composition for cold-rolled dual-phase steels (wt.%) is 0.08–0.18% C, 1.6–2.2% Mn, 0.4% (Cr + Mo). A hot-rolled dual-phase steel would be 0.05% C, 1% Si, 1.5% Mn, 0.6% Cr, and 0.4% Mo.

Suggested Reading

V. Gerold, in *Dislocations in Solids*, vol. 4, F. R. N. Nabarro, ed. New York, NY: Elsevier/North Holland, 1979, p. 219.

A. Kelly and R. B. Nicholson, eds. *Strengthening Methods in Crystals*. Amsterdam: Elsevier, 1971.

D. T. Llewellyn. *Steels: Metallurgy and Applications*, 2nd ed. Oxford: Butterworth-Heinemann, 1992.

J. W. Martin *Precipitation Hardening*. Oxford: Pergamon Press, 1968.
E. Nembach and D. G. Neite. *Precipitation Hardening of Superalloys by Ordered γ'-Particles*, Progress in Materials Science Series, vol. 29. Oxford: Pergamon Press, 1985, p. 177.
A. K. Vasudevan and R. D. Doherty, eds., *Aluminum Alloys: Contemporary Research and Applications*. Boston, MA: Academic Press, 1989.

Exercises

10.1 Compute the hydrostatic stress, in terms of an (r, θ) coordinate, associated with an edge and a screw dislocation in an aluminum lattice. Take $G = 26$ GPa and $b = 0.3$ nm. For a given r, what is the maximum value of this stress?

10.2 Consider the copper–zinc system that is used to make a series of brasses. The radius of solute zinc atom is 0.133 nm, while that of solvent copper atom is 0.128 nm. Calculate the dilational misfit ΔV for this alloy. Compute the hydrostatic stress σ_p for an edge and a screw dislocation in the system. Use the two quantities σ_p and ΔV to obtain the dilational misfit energy for the alloy. Also, compute the force exerted by a solute atom of zinc on a dislocation in copper.

10.3 The interaction energy between an edge dislocation (at the origin) and a solute atom (at r, θ) is given by

$$U = \frac{A}{r} \sin\theta,$$

where A is a constant. Transforming into Cartesian coordinates, plot lines of constant energy of interaction for different values (positive and negative) of $A/2U$. On the same graph, plot the curves for the interaction force. Indicate by arrows the direction in which the solute atoms, with ΔV positive, will migrate.

10.4 Consider a metal with shear modulus $G = 40$ GPa and atomic radius $r_0 = 0.15$ nm. Suppose the metal has a solute that results in a misfit of $\varepsilon = (R - r_0)/r_0 = 0.14$. Compute the elastic misfit energy per mole of solute.

10.5 Estimate the amount of solute (atomic percent) necessary to put one solute atom at each site along all the dislocations in iron. Assume that 1 mm^3 of iron contains about 10^6 mm of dislocation lines.

10.6 Compute the condensation temperature T_c for the following cases:

(a) Carbon in iron with C_0 (average concentration) = 0.01% and U_i (interaction energy) = 0.08 aJ (0.5 eV); note prefix "a" stands for "atto" = 10^{-18}.
(b) Zinc in copper with $C_0 = 0.01\%$ and $U_i = 0.019$ aJ (0.12 eV).

10.7 One of the Hume-Rothery rules for solid solutions[11] is that the solubility of solute B in solvent A becomes negligible when the atomic radii of A and B differ by more than 15%. Plot the maximum solubility (atomic percent) of

[11] W. Hume-Rothery and G. V. Raynor, *The Structure of Metals and Alloys* (London: Institute of Metals, 1956), p. 97.

Ni, Pt, Au, Al, Ag, and Pb as a function of the ratio of solute and solvent (Cu) radii, and verify that the solid solubility in Cu drops precipitously at a size ratio of about 1.15. Use the following data:

$r_{Ni} = 0.1246$ nm $\quad r_{Al} = 0.143$ nm
$r_{Ag} = 0.1444$ nm
$r_{Pt} = 0.139$ nm $\quad r_{Pb} = 0.1750$ nm
$r_{Cu} = 0.1278$ nm $\quad r_{Au} = 0.1441$ nm

10.8 A steel specimen is being tested at a strain rate of 3×10^{-3} s^{-1}. The cross-sectional length is 0.1 m. A Lüders band forms at the section, with an instantaneous strain of 0.2. What is the velocity of propagation of the two Lüders fronts?

10.9 An overaged, precipitation-hardenable alloy has a yield strength of 500 MPa. Estimate the interparticle spacing in the alloy, given that $G = 30$ GPa and $b = 0.25$ nm.

10.10 Consider a unit cube of a matrix containing uniform spherical particles (with radius r) of a dispersed second phase. Compute the average distance between the particles for a volume fraction f of particles equal to 0.001 and $r = 10^{-6}$ cm.

10.11 For a precipitation-hardenable alloy, estimate the maximum precipitate size that can undergo shear by dislocations under plastic strain. Take matrix shear modulus = 35 GPa, Burgers vector = 0.3 nm, and specific energy of precipitate–interface created by shear = 100 mJ/m^2.

10.12 An aluminum alloy contains 2% volume fraction of a precipitate that results in $\varepsilon = 5 \times 10^{-3}$. Determine the average spacing l between precipitates above which there will be a significant contribution to strength due to the difference in atomic volume of the matrix and the precipitate. Below this critical value of l, what will be the mechanism controlling yielding?

10.13 Calculate the critical radius of precipitates for which an Al–Mg alloy containing 10% Mg will be strengthened by Orowan looping instead of particle shear. Use the following data:

$$\gamma_{Al_2Mg} = 1.4\,J/m^2,$$
$$G_{Al} = 26.1\,GPa,$$
$$r_{Al} = 0.143\,nm.$$

10.14 An Al–Cu alloy with 4% weight Cu is aged to form θ precipitates ($CuAl_2$).

(a) Using Figure 10.14(a), determine the volume fraction of $CuAl_2$. Take $\rho_{Al} = 2.7 \times 10^3$ kg/m^3 and $\rho_{Cu} = 8.9 \times 10^3$ kg/m^3.
(b) Establish the stresses required for precipitate shearing and bypass by dislocations as a function of precipitate radius, given that $\gamma_{CuAl_2} = 2.7$ J/m^2, $G_{Al} = 26.1$ GPa, and $r_{Al} = 0.143$ nm.

10.15 Figure E10.3 shows the Al–Mg phase diagram. For an alloy with 10% Mg by weight, calculate the Al_2Mg equilibrium volume fraction of precipitates if the densities of Al and Al_2Mg are 2.7 and 2.3 g/cm^3, respectively.

10.16 An aluminum alloy is strengthened by dispersed alumina particles. These particles are spherical and have a diameter of 15 μm. The weight percentage of alumina in aluminium is 3%. Estimate the dispersion strengthening.

Given:

$G_{Al} = 28$ GPa,
Density (Al) $= 2.70$ g/cm^3,
Density (Al_2O_3) $= 3.96$ g/cm^3.

Chapter 11

Martensitic Transformation

11.1 Introduction

In this chapter, we discuss one important means of altering the mechanical response of metals and ceramics: martensitic transformation. Martensitic transformation is a highly effective means of increasing the strength of steel. An annealed medium-carbon steel (such as AISI 1040) has a strength of approximately 100 MPa. By quenching (and producing martensite), the strength may be made to reach about 1 GPa, a tenfold increase. The ductility of the steel is, alas, decreased.

A quite different effect is observed in ceramics. Martensitic transformation can be exploited to enhance the toughness of some ceramics. If a ceramic undergoes a martensitic transformation during the application of a mechanical load, the propagation of cracks is inhibited. For example, partially stabilized zirconia has a fracture toughness of approximately 7 MPa $m^{1/2}$. An equivalent ceramic not undergoing martensitic transformation would have a toughness less than or equal to 3 MPa $m^{1/2}$.

An additional, and very important, effect associated with martensitic transformations is the "shape-memory effect." Alloys undergoing this effect "remember" their shape prior to deformation. The three effects just described have important technological applications.

11.2 Structures and Morphologies of Martensite

Quenching has been known for over 3,000 years and is, up to this day, the single most effective mechanism known for strengthening steel. However, it is only fairly recently that the underlying mechanism has been studied in a scientific manner and understood. Initially attributed to a beta phase supposedly existing in the Fe–C system, the strengthening effect is now known to be due to a metastable phase: *martensite*. The term martensite was used in honor of a German scientist Martens. The investigations leading to the understanding of

Table 11.1 Systems in which Martensitic or Quasi-Martensitic Transformation Occurs[a]

Alloy	Structure Change
Co, Fe–Mn, Fe–Cr–Ni	FCC→HCP
Fe–Ni	FCC→BCC
Fe–C, Fe–Ni–C, Fe–Cr–C, Fe–Mn–C	FCC→BCT
In–Tl, Mn–Cu	FCC→FCT
Li, Zr, Ti, Ti–Mo, Ti–Mn	BCC→HCP
Cu–Zn, Cu–Sn	BCC→FCT
Cu–Al	BCC→distorted HCP
Au–Cd	BCC→orthorhomic
ZrO_2	tetragonal→monoclinic

[a] Adapted with permission from V. F. Zackay, M. W. Justusson, and D. J. Schmatz, *Strengthening Mechanisms in Solids*, (Metals Park, OH: ASM, 1962), p. 179.

the mechanisms governing, and factors affecting, martensitic transformations have posed a great challenge to researchers over the second half of the twentieth century. Out of a confusing maze of apparently contradictory phenomena, order has appeared. Martensitic-like transformations have been identified in a great number of systems, including pure metals, solid solutions, intermetallic compounds, and ceramics. In order to assess the mechanical behavior of martensite and take advantage of its unique responses in technological applications, one has to understand the fundamental aspects of the transformation. Table 11.1 presents a number of systems in which martensitic-like transformations have been observed.

The original use of the martensitic transformation was exclusively to harden steel. Other developments have led to its use in different contexts. In transformation-induced plasticity (TRIP) steels, the martensitic transformation occurs during deformation and strengthens the regions ahead of a crack or near the neck in a tensile specimen, the ductility of the material is enhanced, while the strength level remains high. This results in great toughness. Ceramics (zirconia) are toughened through the same principle; the fracture toughness of partially stabilized zirconia can be as high as three times that of conventional ceramics.

Another manifestation of the martensitic transformation is the shape-memory effect. Upon being plastically deformed, the material undergoes internal changes in the configuration of the martensite plates. Heating the material recomposes the initial shape. This effect

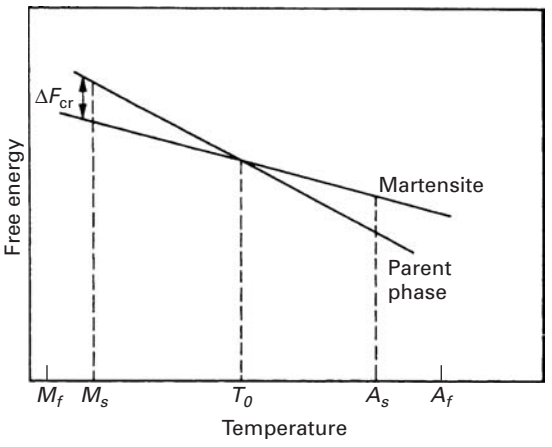

Fig. 11.1 Free energy versus temperature for austenitic and martensitic phases. M_s, M_f, A_s, and A_f marked on abscissa.

is discussed in detail in Section 11.5. More complex processing procedures involving the martensitic transformation, such as ausforming and maraging, have been developed for steels.

A martensitic transformation is a lattice-distortional, virtually diffusionless structural change having a dominant deviatoric component and an associated change in shape so that strain energy dominates the kinetics and morphology of the transformation. The requirement that there be no diffusion stems from thermodynamics: The driving energy required for martensitic transformation is much higher (in the case of irreversible martensites, especially) than that needed for diffusional decomposition (such as precipitation or spinodal decomposition). Hence, as the alloy is cooled, the diffusional transformations would take place at a higher temperature, where the free-energy difference between the two phases is not very large. Figure 11.1 shows the free energies of the parent and martensitic phase as a function of temperature. At T_0, the equilibrium temperature, the two phases have the same free energy. M_s is the highest temperature at which martensite starts to form spontaneously. The critical free energy required for the martensitic transformation is ΔF_{cr} and is around 1,200 kJ/mol for Fe–Ni and Fe–C alloys. Hence, if a diffusion-induced transformation competes with the martensitic transformation, the cooling in the region where $T_0 \rightarrow M_s$ has to be fast enough to avoid the diffusional transformation. On the other hand, if T_0 is low enough, there is essentially no diffusion, and slow cooling will produce martensite. Upon heating above austenite start temperature A_s, the martensite reverts to austenite. For irreversible martensites, the gap between M_s and A_s is a few hundred kelvins; for reversible martensite, the gap is of a few tens of kelvin.

The martensite phase can exhibit a variety of morphologies, depending on the composition of the alloy, the conditions in which it is formed, and its crystalline structure. The three most common morphologies are the lenticular (lens-shaped), the lath (a large number of blocks juxtaposed in a shinglelike arrangement), and the acicular (needle-shaped). These are shown in Figures 11.2 through 11.5. Lenticular martensite occurs in Fe–Ni and Fe–Ni–C alloys with

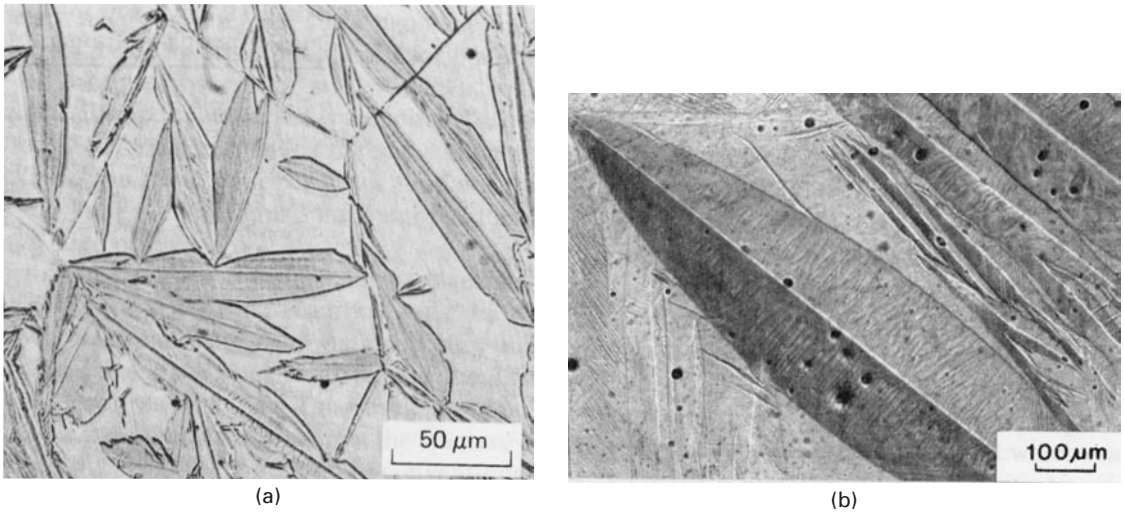

(a) (b)

Fig. 11.2 (a) Lenticular martensite in an Fe–30% Ni alloy. (Courtesy of J. R. C. Guimarães.) (b) Lenticular (thermoelastic) martensite in Cu–Al–Ni alloy. (Courtesy of R. J. Salzbrenner.)

approximately 30% Ni and in Fe–C alloys with over 0.6% C. The central region is called the *midrib* and etches preferentially. The substructure is characterized by twins, dislocations, or both. In the particular case of Figure 11.2(a), the region adjacent to the midrib is twinned, and the external parts are dislocated. Figure 11.2(b) shows lenticular martensite in a Cu–Al–Ni alloy. This material exhibits the shape-memory effect. Lath martensite, on the other hand, is quite different, consisting of small, juxtaposed blocks that are arranged in packets separated by low-angle grain boundaries. Each packet is composed of blocks with a thickness varying between a few micrometers and a few tens of micrometers; the blocks make specific angles with their neighbors. There is a repetitive pattern in each packet, leading to a 360° rotation and a resultant periodicity. Low-carbon steels and Fe–Ni alloys with less than about 30% nickel exhibit this morphology, shown in Figure 11.3.

In steels, there is a significant difference in the mechanical properties of twinned and dislocated martensites. Figure 11.4 shows a medium-carbon steel (0.3% C) that can exhibit both lath (dislocated) and lenticular (twinned) martensites. It can be seen that twinned martensite gives poor toughness, which is consistent with what we learned about twinning in Chapter 5. Mechanical twinning can give rise to microcracks, which are initiation sites for failure of the material (see Figure 8.6). The example of Figure 11.4 is a wonderful illustration of how the microstructure (in this case, inside the martensite lenses and laths) can have a dramatic effect on mechanical properties. This fact is often overlooked by engineers.

Acicular martensite is shown in Figure 11.5. This form occurs in austenitic stainless steel (Fe–Cr–Ni alloys) after deformation. Needles form at the intersection of the slip bands (either dislocations, stacking faults, twins, ε-martensite, or a combination thereof). Since the intersection of these bands is a thin "tube," the martensite forming in it has this specific shape (marked by arrows in the figure). Acicular martensite has the BCC or BCT structure and has a marked

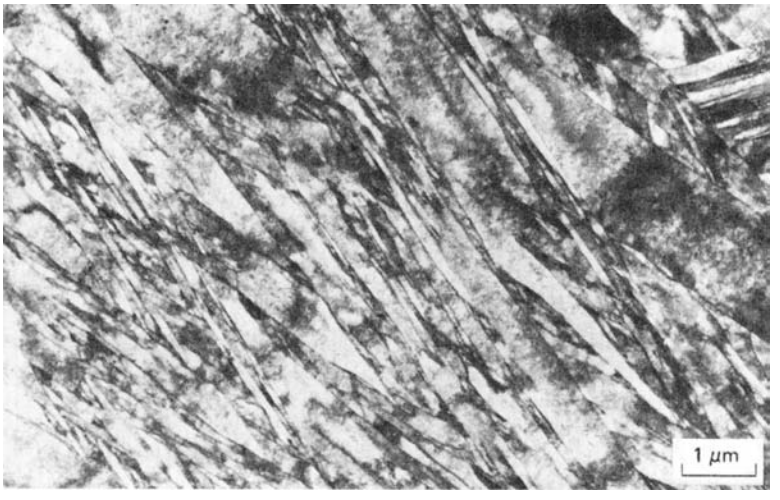

Fig. 11.3 Lath martensite. (Reprinted with permission from C. A. Apple, R. N. Caron, and G. Krauss, *Met. Trans*., 5 (1974) 593.)

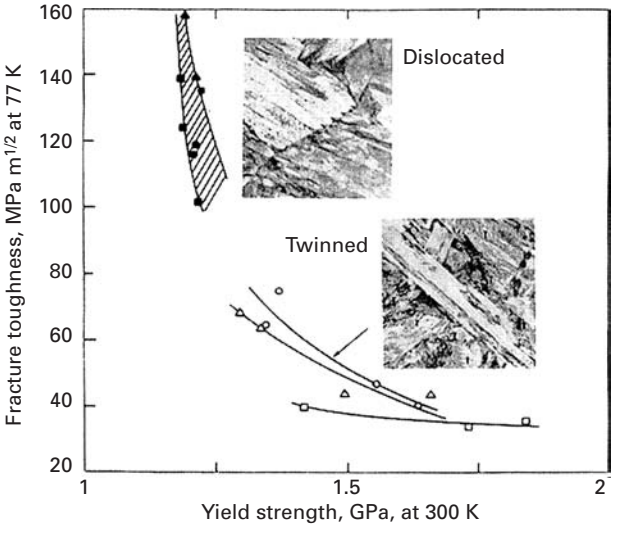

Fig. 11.4 Comparison of mechanical properties between twinned and dislocated martensite in medium-carbon (0.3% C) steel. (Courtesy of G. Thomas.)

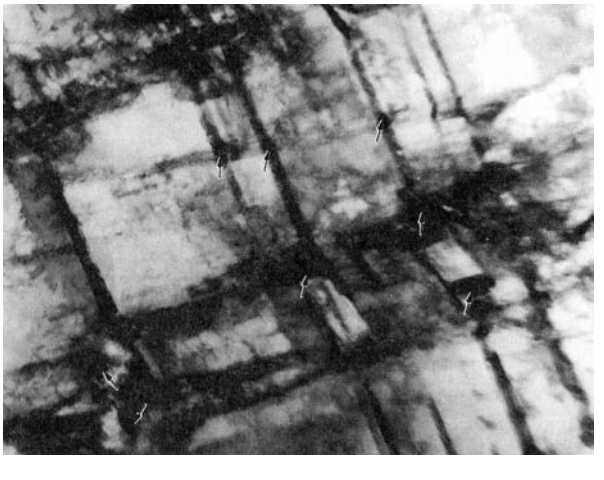

Fig. 11.5 Acicular martensite in stainless steel forming at intersection of slip bands (Courtesy of G. A. Stone.)

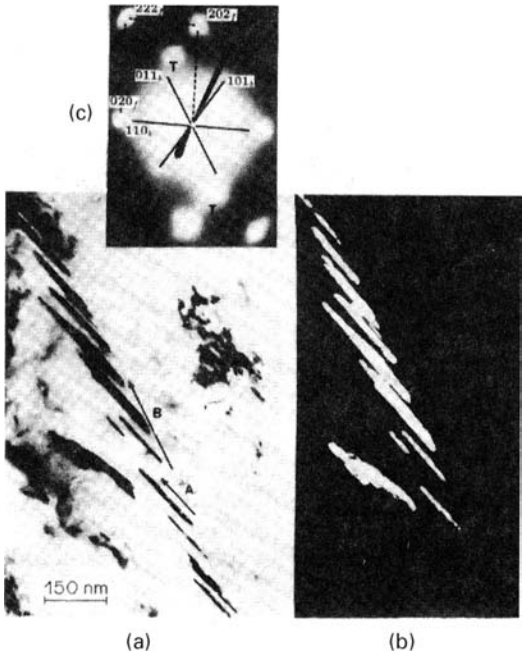

Fig. 11.6 (a) Transmission electron micrograph showing a group of twins inside martensite transformed at −140 °C and 2 GPa. (b) Dark-field image of twins on $(112)_b$ plane; (c) Stereographic analysis for habit (in FCC) and twin (in BCC) planes. (From S. N. Chang and M. A. Meyers, *Acta Met.*, 36 (1988) 1085.)

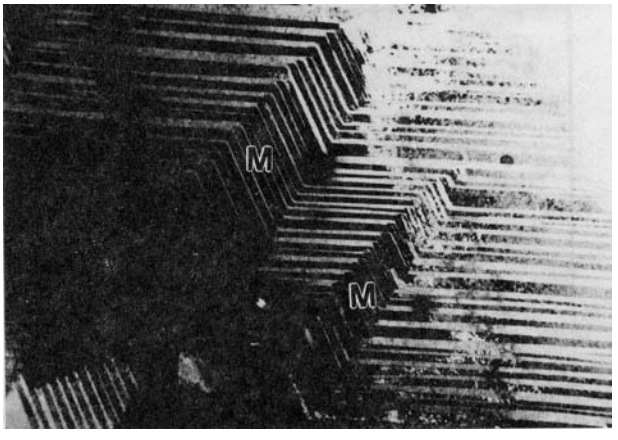

Fig. 11.7 Martensite lenses (M) being transversed by twins, which produce self-accommodation. (Courtesy of A. R. Romig.)

effect on the strength and work-hardening ability of the alloy. Other martensite morphologies have been observed also. ε-martensite is HCP and forms in plates. It can be produced in steel by subjecting the metal to a high pressure (>13 GPa) or in austenitic stainless steels by deformation. After substantial plastic deformation, sheaves of fine parallel laths were observed to form along the austenite slip bands in austenitic Fe–Ni–C alloys. Yet another morphology is the butterfly martensite, so called because two lenses form in a coupled manner; the resultant microstructure resembles a number of butterflies. The plastic deformation accompanying the martensite, constrained by the surrounding matrix, can occur by either slip or twinning. Examples of twinned martensite are shown in Figure 11.6 (for an Fe alloy with 22.5 wt.% Ni and 4 wt.% Mn) and Figure 11.7 (for a U–Re alloy). The transmission electron micrograph (Figure 11.6(a)) and dark-field

picture (Figure 11.6(b)) show the group of twins inside a martensite lens. Crystallographic analysis of the electron diffraction pattern of Figure 11.6(c) reveals the habit and twinning planes. In the case of the U–Re system (Figure 11.7), the twins propagate from the lenses into the matrix; the two martensite lenses are indicated by *M*.

In spite of these differences in morphology, some unique features are common to all martensites. The most important is the existence of an *undistorted and unrotated plane*. The crystallographic orientation relationship between parent and martensite phases is such that there *always* is a plane that has the same indices in the two structures. This undistorted and unrotated plane is called the *habit plane*; it is usually a plane with irrational indices. For a steel with 1.4% carbon, Kurdjumov and Sachs found the following relationships for habit plane (225):[1]

$$(111)_A || (011)_M$$
$$[10\bar{1}]_A || [01\bar{1}]_M .$$

Steels with less than 1.4% carbon exhibit the same relationship. This specific martensite is known as (225). Nishiyama investigated the Fe–Ni–C alloys and steels with carbon content greater than 1.4% and obtained the following relationship for habit plane (259):[2]

$$(111)_A || (011)_M$$
$$[11\bar{2}]_A || [01\bar{1}]_M .$$

11.3 Strength of Martensite

The martensitic transformation has the ability to confer a great degree of strength on steels; other alloys do not seem to have such strong martensites. The strength of martensite in steel is dependent on a number of factors, the most important being the carbon content of the steel. While the Rockwell *C* hardness of iron increases from 5 to 10 when it is transformed to martensite, it increases from 15 to 65 when the carbon content is 0.80% (eutectoid steel). The origin of the high hardness of martensite has been the object of great controversy in the past. It is now fairly well established that there is no single, unique mechanism responsible for it. Rather, a number of strengthening mechanisms operate, most of which we have described in chapters 5, 6, and 10. Nevertheless, the relative importance of these strengthening mechanisms and their interactions are still the object of controversy. It seems that interstitial solution-hardening and substructure strengthening (work-hardening) are the most important ones.

Most metals exhibit a dependence of yield stress on grain size; the martensite lenses divide and subdivide the grain when they

[1] G. Kurdjumov and G. Sachs, *Z. Phys.*, 64 (1930) 325.
[2] Z. Nishiyama, *Sci Rep. Tohoku Univ.*, 2B (1934) 627.

form. Hence, a small-grained alloy produces small martensitic plates, whereas a large-grained alloy produces a distribution of sizes whose mean is much larger. This is shown in Figure 11.8. Three commercial steels (AISI 4310, 4340, and 8650) exhibit a dependence of yield stress on prior austenitic grain size. The slope of the Hall–Petch plot seems to be the same for the three. However, for the range of grain sizes usually encountered, the contribution of grain size is not very important: The grain sizes are equal to 0.1 mm or more. Only in steels that have undergone thermomechanical processing to reduce the austenitic grain size is this strengthening mechanism of significance.

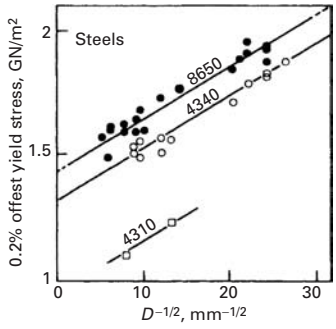

Fig. 11.8 Effect of prior austenite grain size on the yield stress of three commercial martensitic steels. (Adapted with permission from R. A. Grange, *Trans. ASM*, 59 (1966) 26.)

The contribution of substitutional solid-solution elements to the strength of ferrous martensites is relatively unimportant; additionally, it is difficult to separate it from other indirect effects, such as the change in M_s, and stacking-fault energy due to the addition of these elements.

On the other hand, interstitial solutes (carbon and nitrogen, for instance) can play an important effect. If we regard martensite as a supersaturated solution of carbon in ferrite, a great portion of its strength could be ascribed to solution-hardening. Foreman and Makin developed an equation of the following form to express the effect of the solute concentration C on the shear yield stress of the alloy if only the interaction between dislocations and single-atom obstacles is considered:[3]

$$\tau_0 = \left(1 - \frac{\phi'}{5\pi}\right) G \left(\frac{F_{\max}}{2T}\right)^{3/2} (3C)^{1/2}. \tag{11.1}$$

Here, $F_{\max}$ is the maximum force exerted by the obstacle on the dislocation, T is the line tension of the dislocation line, G is the shear modulus, and ϕ' is the angle turned through by the dislocation immediately before it frees itself from the obstacle. The interesting aspect of this equation is that the yield stress should increase with the square root of the solute concentration. And indeed, results obtained by Roberts and Owen confirm Equation 11.1, as can be seen in Figure 11.9. These researchers used alloys with very low M_s (below 77 K), to avoid any secondary effect of the carbon atoms, such as precipitation-hardening or the formation of a Cottrell atmosphere. The fact that the room-temperature tests exhibit the same slope as the ones conducted at 77 K shows that even at room temperature, solid-solution-hardening is operating and effectively strengthening martensite.

Snoek ordering consists of the reorientation of a system of point defects of tetragonal or lower symmetry that are randomly distributed in the stress field of a dislocation (see Section 10.3.5). Single jumps of carbon atoms can organize the atoms in such a way as to minimize their energy. Snoek ordering can take place in a much shorter time interval than does the formation of a Cottrell atmosphere, because no long-range diffusion is required.

[3] A. J. E. Foreman and M. J. Makin, *Phil Mag.*, 14 (1966) 191.

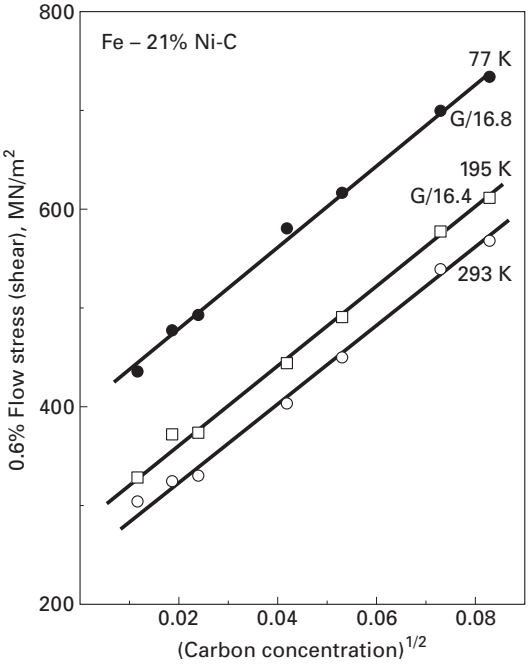

Fig. 11.9 Plot of 0.6% proof stress (one-half of tensile stress) versus $C^{1/2}$ for Fe–Ni–C lath martensite at various temperatures. The slopes are shown as fractions of the shear modulus, which is denoted by *G*. (Adapted with permission from M. J. Roberts and W. J. Owen, *J. Iron Steel Inst.*, 206 (1968) 37.)

The formation of a Cottrell atmosphere, on the other hand, requires that the atoms diffuse toward regions in the dislocation in which their strain energy will be minimized. Carbon atoms produce tetragonal distortions and shear stresses; hence, they seek regions around both edge and screw dislocations in which the shear strains cancel each other. Cottrell atmospheres produce both static and dynamic aging. A manifestation of the latter is the serrated flow (the Portevin–Le Chatelier effect: see also Section 10.3.4).

Carbon atoms have also been shown to exhibit a clustering behavior. Carbon-rich regions have been identified by transmission electron microscopy in steels that had been exposed to temperatures no higher than ambient temperature. These clusters do not change the crystalline structure of the martensite, but produce periodic strain fields, resulting in a "modulated" structure. In this sense, the clustering is closer to a spinodal decomposition than to a precipitation reaction. If the martensite is aged at higher temperatures, cementite and other metal carbides are precipitated. The latter process is called *tempering*.

Frequently, precipitation is observed in martensite. Quenched carbon steels with M_s above room temperature may contain precipitates that form during cooling. In certain low-carbon steels these precipitates have been identified as cementite. It seems that carbon is a more efficient strengthener as a precipitate than in solid solution. The contribution of precipitates in ferrous martensites exceeds that of a solid solution. A very important contribution is that of strain hardening. In twinned martensite, a very fine array of twins 5 to 9 nm thick presents a very effective barrier for additional deformation. These fine twins are the most important factor in the strength of martensite. When

martensite is dislocated, the density of dislocations is typically 10^{10} to 10^{11} cm^{-2}; the substructure resembles that of BCC steel that has been heavily deformed by conventional means.

The contributions to the strength of the martensite in a 0.4% carbon steel can be distributed as follows:[4]

Boundary strengthening	620 MPa
Dislocation density	270 MPa
Solid solution of carbon	400 MPa
Rearrangement of carbon in quench (Cottrell atmosphere Snoek effect, clustering, precipitation)	750 MPa
Other effects	200 MPa
Total	2,240 MPa

Williams and Thompson[4] point out that these effects are not necessarily additive; however, this simplified scheme shows the various contributions.

Yet another source of strengthening is the intrinsic resistance of the lattice to dislocation motion (Peierls–Nabarro stress). This type of resistance accounts for the temperature dependence of yield stress in martensite. Iron exhibits a strong temperature dependence of yield stress at low temperatures, as do other BCC metals. This same behavior is observed in martensite, independent of the existence of precipitates and solutes.

11.4 Mechanical Effects

A martensite lens introduces macroscopic strains in the lattice surrounding it. This is best seen by making fiducial[5] marks on the surface and transforming the material. The fiducial marks will be distorted by the strains. The strains introduced by a martensite lens can be decomposed into a dilational and a shear strain. The dilational strain is perpendicular to the midrib plane, and the shear strain is parallel to the midrib plane. In ferrous alloys, the dilation is approximately 0.05 and the shear strain γ is about 0.02. Figure 11.10 shows a fiducial mark made on the surface of a hypothetical alloy. The shear direction is such that the plane is not distorted. Hence, $\tan\theta = \gamma$, and θ is equal to 11°. The strain matrix can be expressed as

$$\begin{pmatrix} \varepsilon_{11} & \varepsilon_{12} & \varepsilon_{13} \\ \varepsilon_{12} & \varepsilon_{22} & \varepsilon_{23} \\ \varepsilon_{13} & \varepsilon_{23} & \varepsilon_{33} \end{pmatrix} = \begin{pmatrix} 0 & 0 & 0 \\ 0 & 0 & 0.10 \\ 0 & 0.10 & 0.05 \end{pmatrix}. \tag{11.2}$$

Recall that $\varepsilon_{23} = \gamma_{23}/2$. These strains are well beyond the elastic limit of the matrix, and there is plastic deformation in the region

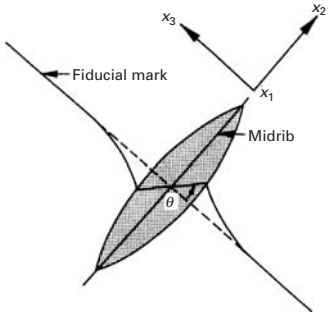

Fig. 11.10 Distortion produced by martensite lens on fiducial mark on surface of specimen.

[4] J. C. Williams and A. W. Thompson, in *Metallurgical Treatises*, J. K. Tien and J. F. Elliott, eds. (Warrendale, PA: TMS-AIME, 1981), p. 487.

[5] A fiducial linear marking is a straight line, imaginary or real, drawn before the transformation.

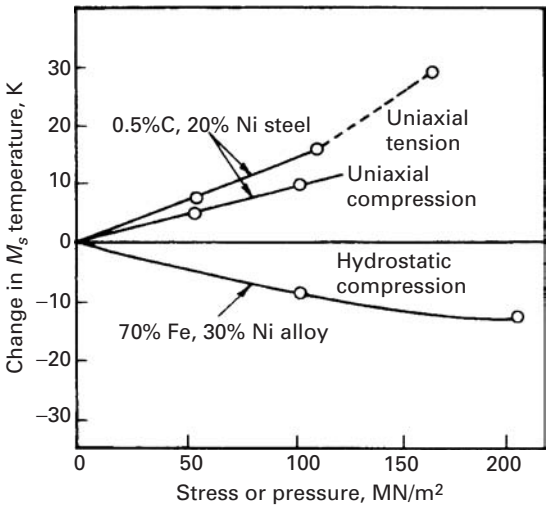

Fig. 11.11 Change in M_s temperature as a function of loading condition. (Adapted with permission from J. R. Patel and M. Cohen, *Acta Met.*, 1 (1953) 531.)

surrounding the martensitic lens. This is reflected in Figure 11.10 by the distortion of the fiducial line.

The dilational and shear stresses and strains imposed by the martensitic transformation interact with externally applied stresses, and very special responses ensue. The effects of externally applied tensile, compressive, and hydrostatic stresses are shown in Figure 11.11. The uniaxial tension and compression increase M_s, whereas hydrostatic compression lowers it. The explanation is that, under the effect of the applied stress, the mechanical work done by the transformation, which can be decomposed into the dilational and shear components, $\sigma\varepsilon$ and $\tau\gamma$, is either increased or decreased:

$$W = \sigma\varepsilon + \tau\gamma. \tag{11.3}$$

The hydrostatic stress counters the lattice expansion produced by martensite, but does not affect the shear stress. Hence, a greater amount of free energy is required to trigger the transformation. Referring to Figure 11.1 we can see that a greater ΔF will require a lowering of M_s. For the tensile test, the applied stress can be decomposed into a normal (positive) stress and a shear stress, both of which aid the transformation. The shear stress aids the martensite variants aligned with the direction of maximum shear (45° to the tensile axis). These variants will form preferentially; hence, the free-energy requirement is decreased and M_s is increased. In the compressive test, the normal portion of the stress is negative and counters the dilational stress of the transformation, whereas the shear stress favors it. (There are always favorably oriented variants.) Since the shear stress term dominates the expression (because of the greater shear strain γ), the tensile stress should be more effective in increasing M_s than the compressive stress is. This is exactly what is shown in Figure 11.11.

Another experimental procedure consists of conducting tensile tests at temperatures above M_s. When the stress level reaches the value at which martensite forms at the test temperature, a significant

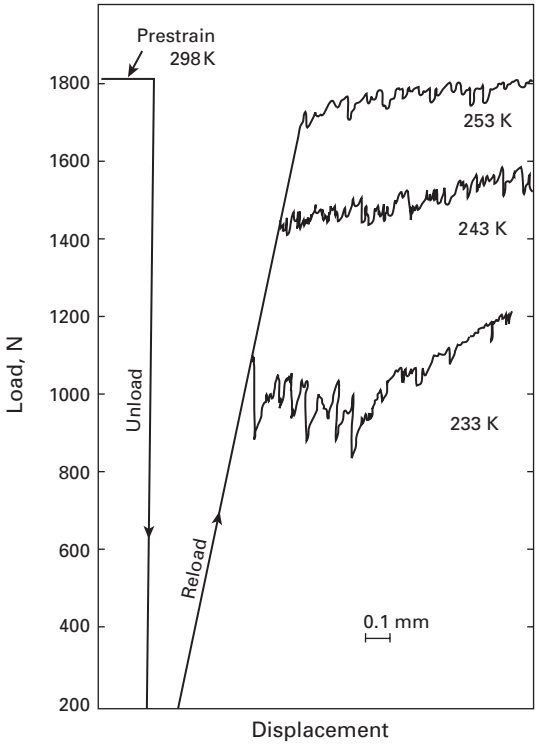

Fig. 11.12 Tensile curves for Fe–Ni–C alloy above M_s, showing martensite forming in elastic range (stress assisted). (Courtesy of J. R. C. Guimarães.)

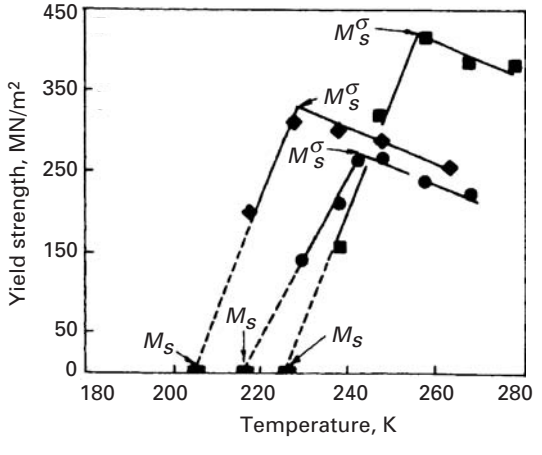

Fig. 11.13 Temperature dependence of the yield strength of Fe–31% Ni–0.1% C. ■, predeformed by shocking; ●, larger grain size; ◆, smaller grain size. (Adapted with permission from J. R. C. Guimarães, J. C. Gomes, and M. A. Meyers, *Supp. Trans. Japan Inst. of Metals*, 17 (1976) 41.)

load drop is observed. Figure 11.12 shows this effect. The load drop is attributed the shear strain of the martensite, which produces an instantaneous increase in strain of the martensite, which produces an instantaneous increase in length of the specimen. As the difference between the test temperature and M_s increases, the stress at which martensite starts forming increases; this can be directly inferred from Figure 11.12. In Figure 11.13 the yield strength is plotted as a function of temperature; when martensite forms in the elastic line, the stress at which it forms is equal to the yield strength (as in Figure 11.12, for instance). The temperature dependence of the stress for martensite transformation is clearly shown by the three straight lines in

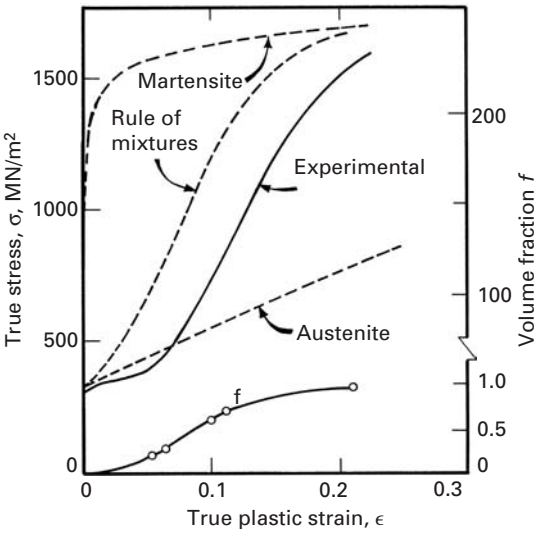

Fig. 11.14 Volume fraction transformed (right-hand side), *f*, and stress (left-hand side) as a function of plastic strain for an austenitic (metastable) steel deformed at –50 °C; experimental and idealized stress–strain curves for austenite, martensite, and mixture. (After R. G. Stringfellow, D. M. Parks, and G. B. Olson, *Acta Met.*, 40 (1992) 1703.)

Figure 11.13. At M_s, as expected, martensite forms spontaneously, without any stress. The plots of yield strength versus temperature for three different conditions have inverted-V shapes. At the point marked M_s^σ, the slope of the curve changes, and above this temperature, the yield stress is produced by conventional dislocation motion; hence, it shows the regular increase with decreasing temperature. Between M_s and M_s^σ, on the other hand, we have *stress-assisted martensite* establishing yield, and the temperature dependence is inverted, leading to a yield stress of zero at M_s. It is worth noting that the three alloys in Figure 11.13 have the same composition, but different processing histories. M_s temperature is affected by grain size. M_s increases with increasing grain size and predeformation; in the case shown in the figure, predeformation was accomplished by shock loading.

The formation of strain-induced martensite occurs in the temperature range above M_s^σ in Figure 11.13. Substantial plastic deformation, in which the substructure has to be sensitized, is required before the first martensite forms. This kind of martensite is called *strain induced*, to differentiate it from *stress-assisted* martensite. Figure 11.14 illustrates the effect of strain-induced martensite on the stress–strain curve of an austenitic stainless steel at -50 °C. The austenite has a low yield stress and work-hardening rate; the transformation to martensite is also shown (right-hand axis). The experimentally obtained curve reflects the fact that an increase in martensite volume fraction is accompanied by plastic strain; the simple rule-of-mixtures curve is higher than the experimental curve because there are complex synergistic processes between the two phases (α and γ).

Strain-induced martensite is responsible for a very beneficial effect: the transformation-induced plasticity (TRIP). Remarkable combinations of high strength and toughness have been obtained in TRIP steels. The high strength is due to work-hardening, carbide precipitation, and dislocation pinning by solutes during thermomechanical

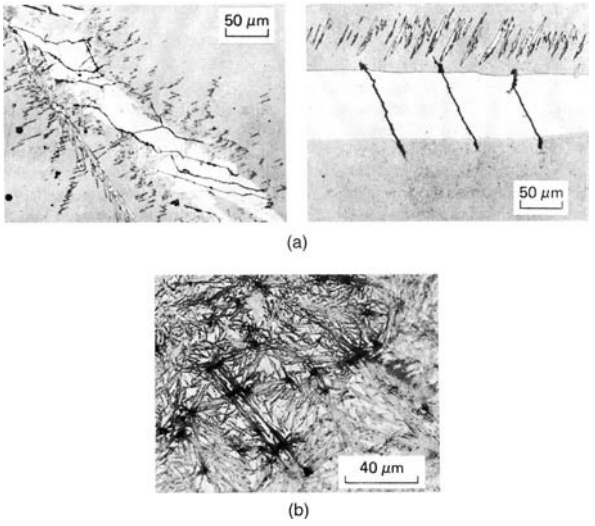

Fig. 11.15 Microcracks generated by martensite. (a) Fe–8% Cr–1% C (225 martensite sectioned parallel to habit plane). (Courtesy of J. S. Bowles, University of South Wales.) (b) Carburized steel. (Reprinted with permission from C. A. Apple and G. Krauss, *Met. Trans.*, 4 (1973) 1195.)

treatment. The high toughness comes from a combination of high strength and high ductility. The ductility is a direct consequence of the strain-induced martensite transformation. If a certain region in the metal is severely deformed plastically, strain-induced transformation takes place, increasing the local work-hardening rate and inhibiting an incipient neck from further growth. On the other hand, if a crack has already formed, martensitic transformation at the crack tip will render its propagation more and more difficult. In Section 11.6, the toughening of a ceramic (ZrO_2) by stress-assisted martensite will be described.

Another mechanical aspect of importance is the fracture of martensite. Fracture is usually initiated in a martensitic alloy along the martensite–austenite or martensite–martensite boundaries. Indeed, upon investigating the fracture surfaces of Fe–31% Ni–0.1% C alloy, Chawla *et al.*[6] found that the density of dimples increased as a function of the amount of martensite in the cross section; the same result was obtained by decreasing the grain size. Hence, the dimple size was tied to the density of interfaces. In carbon-free or low-carbon steels, martensite is fairly soft, and the fracture is, consequently, ductile. In high-carbon steels, on the other hand, martensite is hard and brittle, and the fracture surface takes a cleavage appearance, with the fracture path traversing the plates (or laths). Of great importance in the initiation of fracture is the existence of microcracks in the structure. Marder *et al.*[7] found a great number of microcracks in Fe–C martensites; when the grain size was decreased, the incidence of microcracks decreased. The microcracks were formed when one lens impinged on another. Figure 11.15 shows how these cracks occur. The microcracks act as stress-concentration sites when the specimen is loaded; they are initiation sites for macrocracks.

[6] K. K. Chawla, J. R. C. Guimarães, and M. A. Meyers, *Metallography*, 10 (1977) 201.
[7] A. R. Marder, A. D. Benscoter, and G. Krauss, *Met. Trans.*, 1 (1970) 1545.

Tempering of martensite[8] in steels is performed to improve toughness. However, the tempering process might induce embrittlement. *Temper martensite embrittlement* (TME) results from the segregation of impurities to the previous austenitic grain boundaries, providing a brittle path for propagation of the fracture. The fracture takes on the intergranular morphology. Temper embrittlement (TE) is caused by the impurities such as antimony, phosphorus, tin, and arsenic (less than 100 ppm required) or larger amounts of silicon and manganese. TME and TE occur in different ranges of temperatures; TME is a much more rapid process.

11.5 Shape-Memory Effect

The *shape-memory effect* (SME) is the unique property that some alloys possess according to which, after being deformed at one temperature, they recover their original shape upon being heated to a second temperature. The built-in memory is produced by the martensitic transformation. The effect was first discussed by the Russian metallurgist Kurdjumov. In 1951, Chang and Read[9] reported its occurrence in an In–Ti alloy. However, wide exposure of this property came only after the development of the nickel–titanium alloy by the Naval Ordnance Laboratory (NiTiNOL) in 1968.[10] Since then, research activity in this field has been intense, and a number of β-phase SME alloys have been investigated, including AgCd, AgZn, AuCd, CuAl, CuZn, FeBe, FePt, NbTi, NiAl, and ternary alloys. The Nitinol family of alloys has found wide technological applications, and adjustments in composition can be made to produce M_s temperatures between -273 and 100 °C. This is an extremely helpful feature, and alloys are tailored for specific applications. In the majority of SME alloys the high-temperature phase is a disordered β-phase (body-centered cubic), while the martensitic phase is an ordered BCC structure with a superlattice or orthorhombic structure. Two separate mechanical effects characterize the response of SME alloys: *pseudoelasticity and strain-memory effect*. We describe these next, in connection with tensile and compressive tests.

Pseudoelasticity, or superelasticity, is the result of stress-induced martensitic transformation in a tensile test in which martensite reverts to the parent phase upon unloading. The individual martensite plates do not grow explosively, as in the ferrous martensites, and little irreversible damage is done to the lattice. The shear strain of one plate is accommodated by neighboring plates. The complex motion of the interfaces between the martensite plates along the various variants and within the same martensite plate takes place by the displacement of the interfaces between the different twins.

[8] Tempering consists of heating the martensitic structure to an intermediate temperature.

[9] L. C. Chang and T. A. Read, *Trans. Met. Soc. AIME*, 191 (1951) 49.

[10] W. J. Buehler and F. E. Wang, *Ocean Eng.*, 1 (1968) 150.

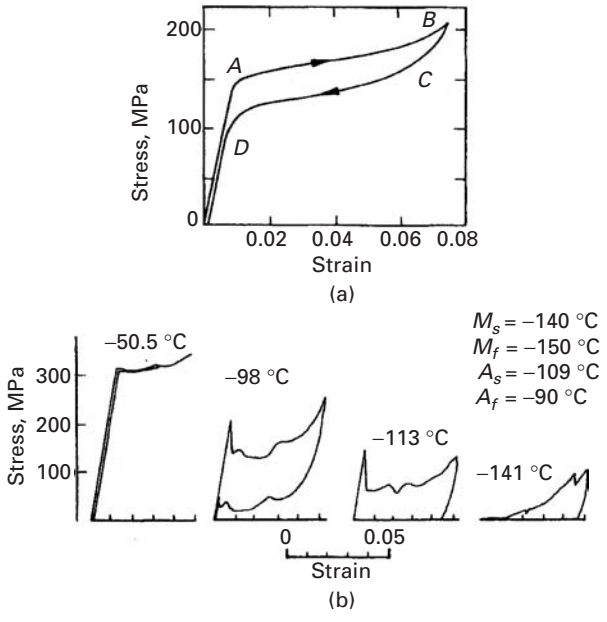

Fig. 11.16 (a) Pseudoelastic stress–strain curve for a single-crystal Cu–Al–Ni, alloy at 24 °C (72 °C above M_s). (b) Dependence on temperature of stress–strain characteristics along the characteristic transformation temperatures. Strain rate: 2.5×10^{-3} min^{-1}. (Reprinted with permission from C. Rodriguez and L. C. Brown, in *Shape Memory Effects*, (New York: Plenum Press, 1975), p. 29.)

Figure 11.16(a) shows the pseudoelastic effect for a Cu–Al–Ni alloy with $M_s = -48$ °C. The test was conducted at 24 °C (72 °C above M_s). At *A*, stress-induced martensite starts to form. At *B*, the martensitic transformation has been completed, and any straining beyond that point will produce irreversible plastic deformation or fracture. Upon unloading, the martensite reverts to the parent phase between *C* and *D*. Further unloading results in the return to the original length of the specimen. The pseudoelastic strain exceeds 6%. The magnitude of the pseudoelastic strain can be calculated from a knowledge of the habit plane of the martensite (and its orientation with respect to the tensile axis) and the magnitude of the shear strain for the transformation. Since the habit plane of martensite is irrational, it has a multiplicity of 24, and there is always a habit plane oriented very close to the plane of maximum shear.

The pseudoelastic (or superelastic) effect is illustrated in a very simplified fashion in Figure 11.17. A specimen with initial length L_0 is compressed. Stress-induced martensitic transformation takes place, and the austenite–martensite interfaces are glissile; that is, they can move under the applied stress. In Figure 11.17(c), two martensite lenses are shown. They continue to grow in Figure 11.17(d). When the stress is decreased, they shrink in the same order as the initial growth. When the stress is reduced to zero, all martensite has disappeared, and the specimen has returned to the original length L_0. Figure 11.17(g) shows the corresponding stages on a stress–strain curve, similar to the stress–strain curve in Figure 11.16(a). The stress–strain curve returns to the origin after the load is removed.

It is not sufficient for the temperature at which testing is conducted to be above M_s to obtain the pseudoelastic effect, as shown in Figure 11.16(b). These tests were conducted on a Cu–Al–Ni alloy. The

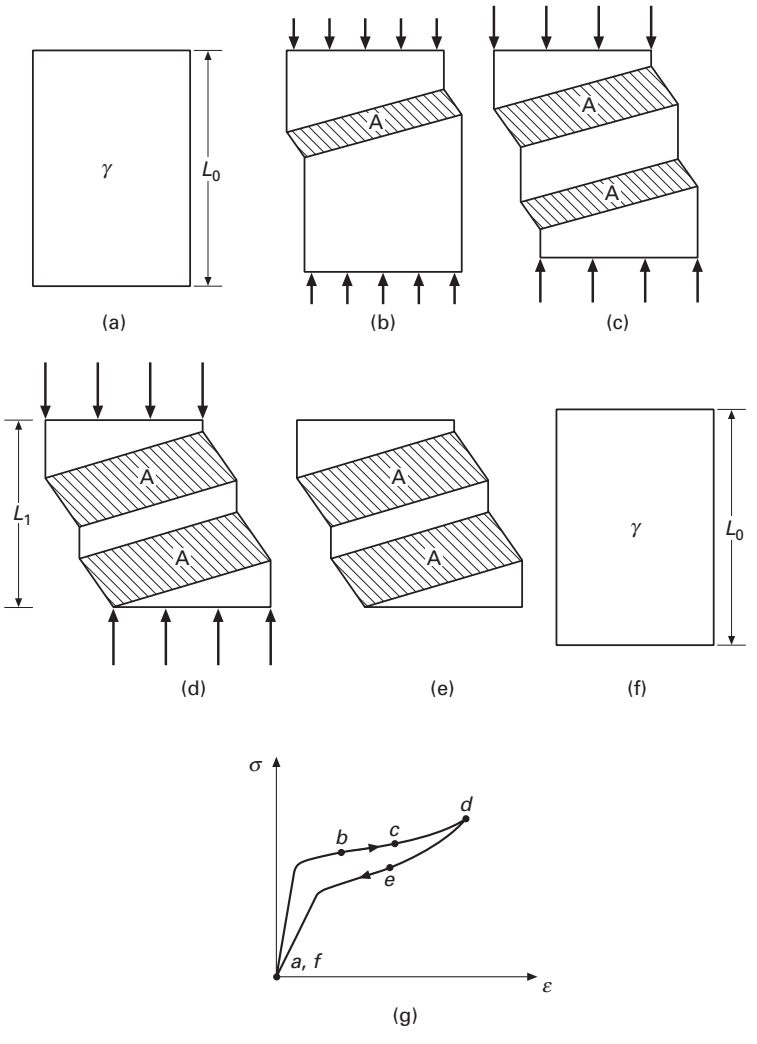

Fig. 11.17 Schematic representation of pseudoelastic (or superelastic) effect. (a) Initial specimen with length L_0. (b, c, d) Formation of martensite and growth by glissile motion of interfaces under increasing compressive loading. (e) Unloading of specimen with decrease in martensite. (f) Final unloaded configuration with length L_0. (g) Corresponding stress–strain curve with different stages indicated.

temperatures A_s and A_f (austenite start and finish, respectively) are also important. If the testing temperature is below A_s, the martensite will not revert to austenite upon unloading; the tests conducted at -141 °C and -113 °C show this irreversibility. For the test conducted at -50.5 °C and -98 °C, total reversibility is obtained, since this temperature is above A_f (-90 °C). Another observation that can be made in Figure 11.16(b) is that the stress at which martensite forms increases with increasing temperature.

When the deformation is irreversible (at -113 °C and -141 °C in Figure 11.16), the effect receives the name *strain-memory effect*. Additional heating is required to return the martensite to its original shape, since the deformation temperature is below A_s. Upon heating, the original dimensions will be regained, as the martensite interfaces move back to retransform the lattice. The sequences in which the plates form and in which they disappear are inverted: the first plate to form is the last to disappear.

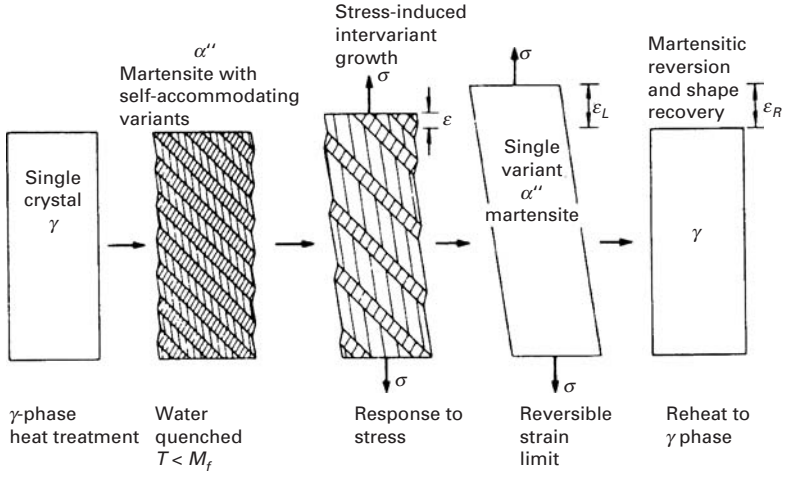

Fig. 11.18 Sequence showing how growth of one martensite variant and shrinkage of others results in strain ε_L. (Courtesy of R. Vandermeer.)

The strain-memory effect is also obtained when deformation is imparted at temperatures below M_s. This is actually the procedure used in most technological applications. In this case, the structure consists of thermally induced martensite; it is present in such a way that all variants occur. When the external stress is applied, the variants that have shear strains aligned with the applied shear strain tend to grow, and the unfavorably oriented variants shrink. Figure 11.18 shows schematically how this takes place. Only two variants are shown, for simplicity. The variant that favors the applied tensile strain grows at the expense of the unfavorably oriented one. Hence, all unfavorable variants disappear, and the favorable variant takes over the structure. On heating, the structure reverts to the original one, composed of equal distribution of the two variants, giving the strain recovery.

Figure 11.19 shows the strain-memory effect for compressive, tensile, and flexure loading. Only two martensite variants are shown: *A* and *B*. In this drawing, variant *B* favors tensile strains, whereas variant *A* produces compression in the direction of loading. Under compressive stresses, variant *A* grows at the expense of *B*. Under tensile loading, the opposite is true. And under bending, variant *B* grows on the outside, while variant *A* grows on the inside. The situation in a real material is much more complex, and polycrystalline effects come into play. Nevertheless, the simple scheme of Figure 11.19 shows the essential features of the strain-memory effect. Upon heating, the three specimens return to the original shape by the reverse motion of the martensite interfaces. Further heating would make the martensite revert to austenite.

When the strain-memory effect is obtained above M_s, a fully austenitic structure gradually becomes martensitic under stress. This is shown in the schematic representation of Figure 11.20. Only one variant of martensite is depicted. The loading stage is similar to that for the superelastic effect. However, upon unloading, the martensite remains in the material, and heating is required to return the

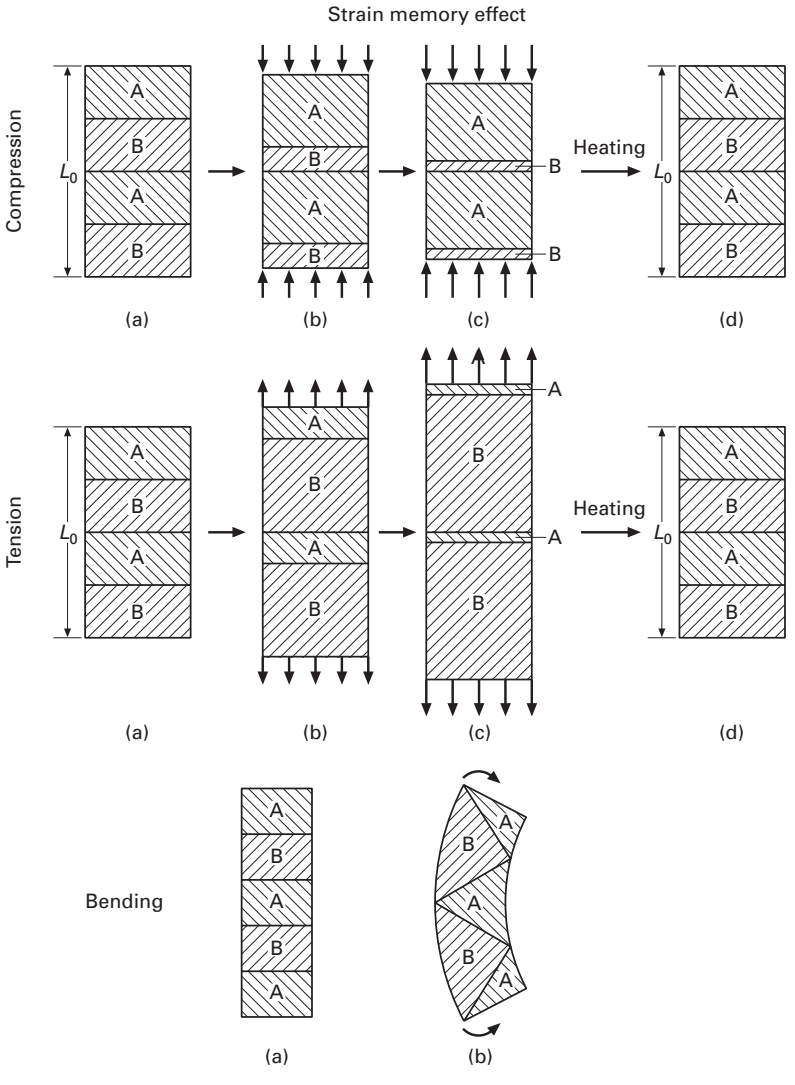

Fig. 11.19 Schematic representation of strain-memory effect in compression, tension, and bending. Variant *A* favors a decrease in dimension in the direction of its length, whereas variant *B* favors an increase in dimension.

martensite to its original dimensions. The reverse transformation occurs in the same order as the martensite transformation, and the specimen "remembers" its original slope.

Other potential benefits of the shape-memory effect involve the increased damping capacity of the material, which can become very large because of the work required to form the martensite. Circuit breakers, pseudoelastic wires for support in brassieres, overheat protection systems, sensors in heating and ventilation, components in the Hubble telescope, pseudoelastic dental arch wires, a pseudoelastic scoliosis correction system (a biomedical application), and porous pseudoelastic tissue are additional examples of applications of the pseudoelastic and strain-memory effects.

Structures containing their own sensors, actuators, and computational or control capabilities are called "smart," "adaptive," or

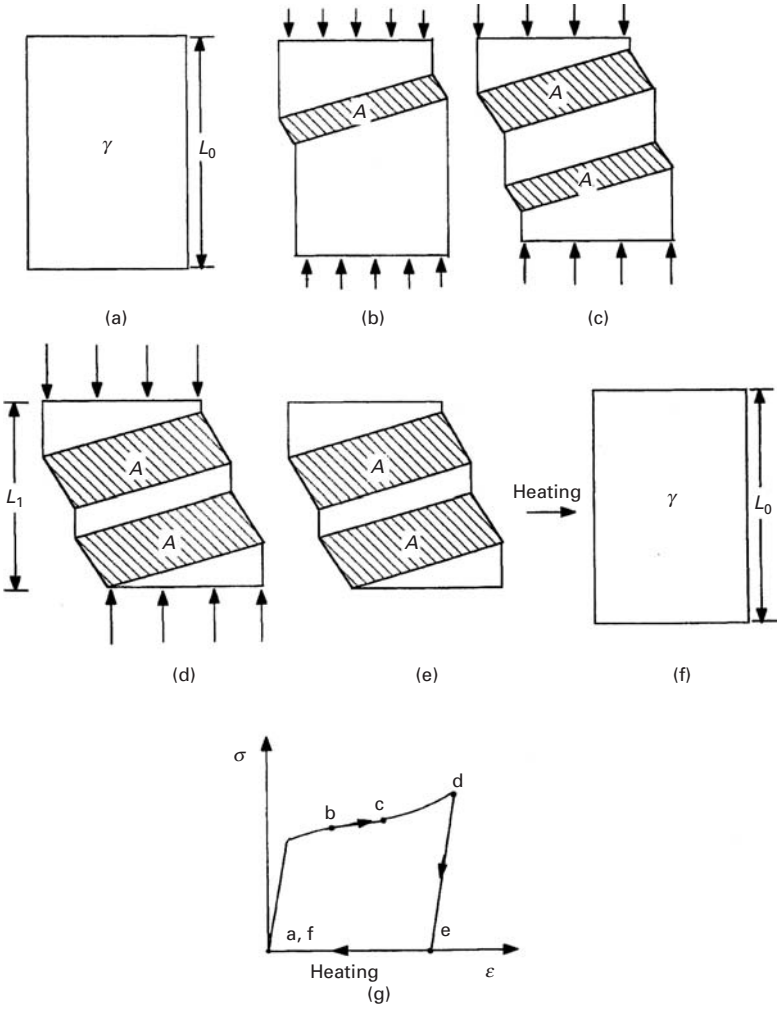

Fig. 11.20 Schematic representation of strain-memory effect. (a) Initial specimen with length L_0. (b, c, d) Formation of martensite and growth by glissile motion of interfaces under increasing compressive stresses. (e) Unloading of specimen. (f) Heating of specimen with reverse transformation. (g) Corresponding stress–strain curve with different stages indicated.

"intelligent" structures. Alloys with good strain-memory effects play an important role in the design of these structures, and novel uses are being continually introduced. Indeed, the shape-memory effect has found some unique uses. One is as a tight coupling for pneumatic and hydraulic lines. The F-14 jet fighter tube couplings are made of Nitinol that is fabricated at room temperature with a diameter 4% less than that of the tubes which will be joined. Then, the couplings are cooled below M_s (−120 °C) and expanded mechanically until their diameter is 4% larger than those of the tubes. They are held at this temperature until they are placed over the tube ends. Allowed to warm, they shrink to their initial diameter; impeded by the tube, they provide a tight fit. Electrical connectors that are opened and closed by changes in temperature are another application. Orthopedic and orthodontic aids have also been made of SME alloys, and Nitinol seems to react well in the body fluid environment. The pen-drive mechanism in recorders is a very successful application of the SME; many such drives are in service.

11.5.1 Shape-Memory Effect in Polymers

Some polymers can show a shape-memory effect, wherein they change their shape after we increase their temperature. In metallic alloys, the shape-memory effect has origin in a martensitic phase transformation. The story is a bit different in polymers. In polymers, we need two components at the molecular level to induce a shape-memory effect: cross-links that control the permanent shape and switching segments that allow us to fix the temporary shape. Above a critical temperature, T_c, we can deform the polymer. When we cool it below T_c and release the external stress, we get the temporary shape. When we heat the polymer to a temperature $T > T_c$, it regains its permanent shape. Lendlein *et al.*[11,12] showed this phenomenon in phase-segregated, multiblock copolymers wherein molecular parameters can be used to tailor macroscopic properties. One component, oligo(ε-caprolactone) dimethacrylate, furnishes the crystallizable "switching" segment that determines both the temporary and permanent shape of the polymer. By varying the amount of the comonomer, *n*-butyl acrylate, in the polymer network, the cross-link density can be adjusted. In this way, the characteristics of a polymer network can be exploited to tailor the mechanical strength and transition temperature over a wide range. It should be mentioned that homopolymers of both monomers are known to be biocompatible, which is of great importance for biomedical applications. The external stimulus, e.g. an increase in temperature, can be obtained by means of electrical current or light. This ability of polymers to take predetermined temporary shapes and then recover their original shape at ambient temperature by exposure to light could be useful in biomedical applications. Among the potential medical uses of these shape-memory polymers are: stents, used to keep blood vessels open, and catheters and sutures with more "give" than those currently available.

11.6 Martensitic Transformation in Ceramics

By far the most important, but not the only, martensitic transformation in a ceramic is the tetragonal-to-monoclinic transformation exhibited by zirconia (ZrO_2). This transformation leads to a significant enhancement in the toughness of ceramics if ZrO_2 is used either alone or as a distributed phase in other ceramics, such as alumina. Garvie *et al.* reported a very significant increase in tensile strength (from 250 to 650 MPa) and work of fracture (a measure of toughness) for tetragonal zirconia, in comparison with monoclinic zirconia.[13] They attributed this increase in strength to a martensitic transformation occurring during deformation, in a manner analogous to the TRIP

[11] A. Lendlein, H. Jiang, O Jünger, and R. Langer, *Nature*, 434 (2005) 879.
[12] A. Lendlein and R. Langer, *Science*, 296 (2002) 1673.
[13] R. C. Garvie, R. H. Hannink, and R. T. Pascal, *Nature*, 258 (1975) 703.

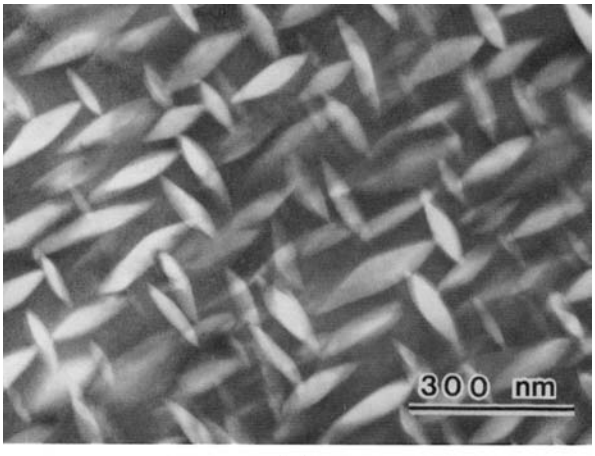

(a)

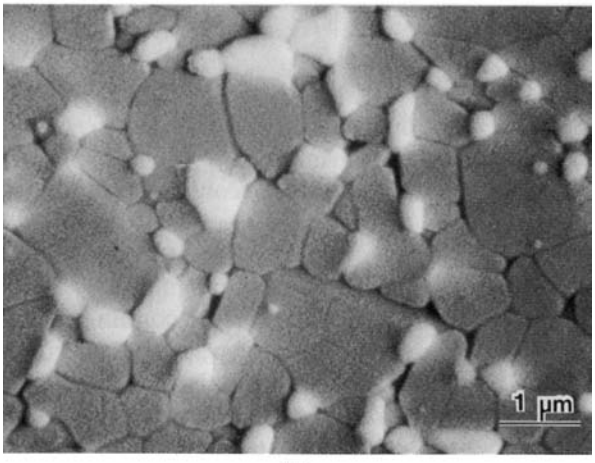

(b)

Fig. 11.21 (a) Lenticular tetragonal zirconia precipitates in cubic zirconia (PSZ). (b) Equiaxial ZrO_2 particles (bright) dispersed in alumina (ZTA). (Courtesy of A. H. Heuer.)

effect. The three most common ways in which this transformation is used are as follows:

1. Tetragonal zirconia polycrystals (TZPs), which are nearly single-phase polycrystalline ceramics. TZPs are fabricated from fine-grained zirconia powders by sintering.
2. Partially stabilized zirconia (PSZ), in which tetragonal-ZrO_2 is a precipitate phase and the matrix is cubic zirconia. The highest toughnesses reported in PSZ are around 18 MPa $m^{1/2}$.
3. Zirconia-toughened alumina (ZTA), in which zirconia is a dispersed phase in the alumina matrix. ZTA materials are fabricated by co-sintering Al_2O_3 and ZrO_2 powders. ZTA materials are relatively tough (K_{Ic} up to approximately 14 MPa $m^{1/2}$) and have high strength (1–2 GPa). This represents a significant enhancement in comparison with pure Al_2O_3 (K_{Ic} about 3 MPa $m^{1/2}$).

Figure 11.21(a) shows lenticular PSZ precipitates in cubic zirconia. The lens plane corresponds to the $\{100\}$ planes of the cubic phase; thus,

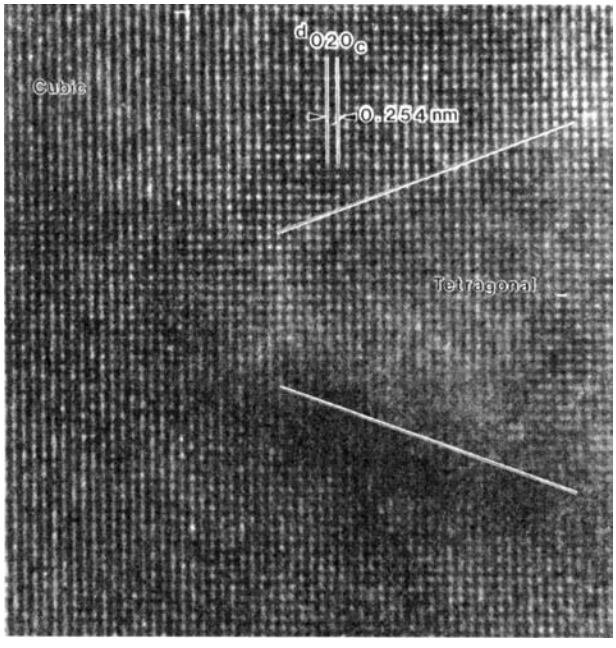

Fig. 11.22 Atomic-resolution transmission electron micrograph showing extremity of tetragonal lens in cubic zirconia; notice the coherency of boundary. (Courtesy of A. H. Heuer).

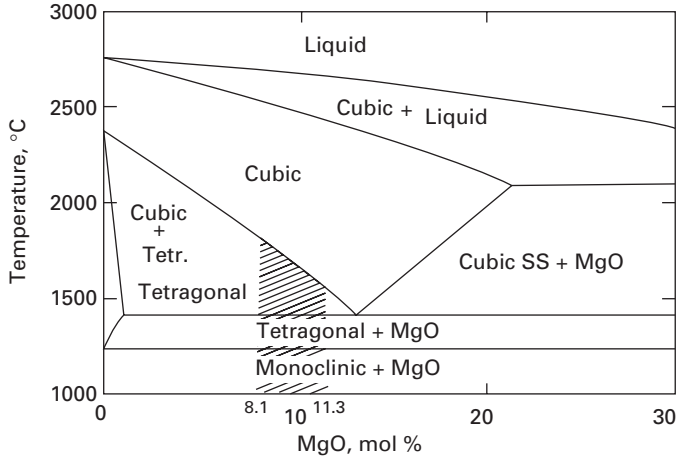

Fig. 11.23 ZrO_2-rich portion of ZrO_2–MgO phase diagram. Notice the three crystal structures of Zro_2: cubic, monoclinic, and tetragonal.

there are three possible variants for the precipitates. The tetragonal lens is coherent with the cubic matrix, and the atomic-resolution TEM of Figure 11.22 shows the correspondence between the planes; the (100) of the tetragonal and cubic phases are parallel. The lenses are shaped approximately as oblate spheroids with an aspect ratio of 5. Figure 11.21(b) shows ZrO_2 particles (bright) in an alumina ceramic.

Zirconia has three allotropic forms: cubic, tetragonal, and monoclinic. Figure 11.23 shows the ZrO_2–MgO phase diagram. In pure zirconia, only very small particles (approximately 60 nm across) can be retained at room temperature in the tetragonal structure. By using a stabilizing compound such as magnesia (MgO), calcia (CaO), yttria

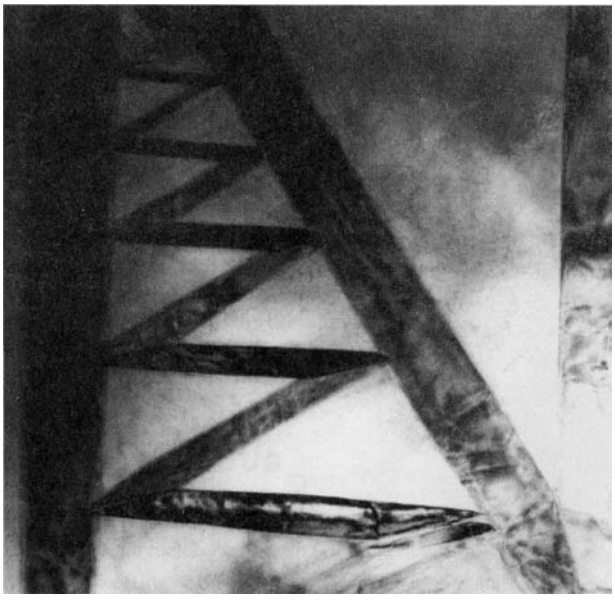

Fig. 11.24 TEM of martensitic monoclinic lenses in ZrO_2 stabilized with 4 wt% Y_2O_3 and rapidly solidified; the zigzag pattern of lenses is due to autocatalysis. (Courtesy of B. A. Bender and R. P. Ingel.)

(Y_2O_3), or ceria (CeO_2), it is possible to retain the tetragonal phase, generally stable only between 1,240 and 1,400 °C, at room temperature. The range of MgO additions for which this occurs is shown in the phase diagram by hatching. The tetragonal-to-monoclinic transformation, which takes place martensitically under applied stress, has a dilational (about 4–6%) and a shear (approximately 14%) component. The martensitic nature of the transformation is evident in the transmission electron micrograph of Figure 11.24. The martensite lenses form a zigzag pattern between two larger lenses; this is a typical autocatalytic nucleation sequence, in which one lens, impinging on a boundary, generates the defects that nucleate the subsequent lens. The process continues, leading to the characteristic pattern. The martensite shown in the figure was generated through rapid solidification.

The increase in toughness due to the martensitic tetragonal-to-monoclinic transformation can be qualitatively explained as follows. In the regions surrounding a propagating crack, the stresses induce the transformation, which has dilational and shear strain components. These strains work against the stress field generated by the crack, decreasing the overall stress intensity factor and, thereby, increasing the toughness. Figure 11.25(a) illustrates this behavior in ZTA; Figure 11.25(b) shows the effect in PSZ. The gray grains indicate tetragonal ZrO_2, whereas the black grains are transformed to the monoclinic phase. The crack, advancing from left to right, triggers the transformation; more black dots surround the crack, leading to its arrest. In Figure 11.25(b), the lenticular tetragonal ZrO_2 precipitates in the cubic matrix are transformed to monoclinic in the region surrounding the crack. They appear as brighter lenses in the TEM because of favorable transmission conditions.

Fig. 11.25
(a) Zirconia-toughened alumina (ZTA) traversed by a crack. The black regions represent monoclinic (transformed) zirconia, the gray regions tetragonal (untransformed) zirconia. (Courtesy of A. H. Heuer.) (b) Partially stabilized zirconia (PSZ) lenticular precipitates transformed from tetragonal to monoclinic in the vicinity of a crack. Notice the brighter transformed precipitates. (Courtesy of A. H. Heuer.)

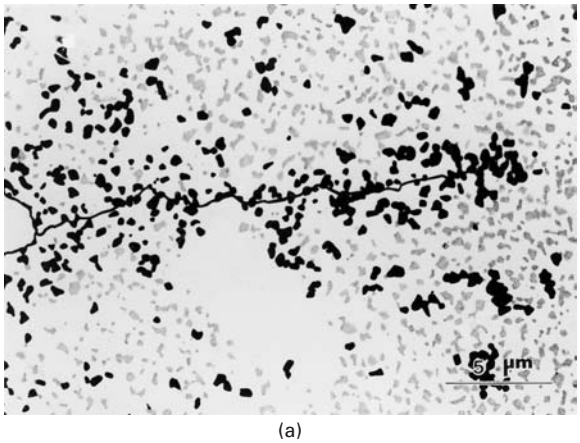

(a)

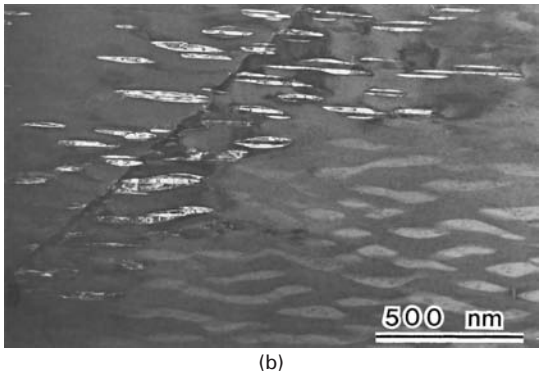

(b)

Suggested Reading

J. W. Christian. "The Strength of Martensite," in *Strengthening Methods in Crystals*, A. Kelly and R. B. Nicholson, eds. Amsterdam: Elsevier, 1971, p. 261.

J. W. Christian. *The Theory of Transformations in Metals and Alloys*, 2nd ed. Elmsford, NY: Pergamon Press, 1981.

D. J. Green, R. H. J. Hannink, and M. V. Swain. *Transformation Toughening of Ceramics*. Boca Raton, FL, CRC, 1989.

A. H. Heuer. "Fracture-Tough Ceramics," in *Frontiers in Materials Technologies*, M. A. Meyers and O. T. Inal, eds. Amsterdam: Elsevier, 1985, p. 265.

A. H. Heuer, F. F. Lange, M. V. Swain, and A. G. Evans. "Transformation Toughening: An Overview." *J. Am. Cer. Soc.*, 69 (1986) i–iv.

G. Krauss. *Principles of Heat Treatment of Steel*. Metals Park, OH: ASM, 1980.

Z. Nishiyama. *Martensitic Transformation*. New York, NY: Academic Press, 1978.

G. B. Olson and M. Cohen. "Principles of Martensitic Transformations," in *Frontiers in Materials Technologies*, M. A. Meyers and O. T. Inal, eds. Amsterdam: Elsevier, 1985, p. 43.

G. B. Olson and W. S. Owen, eds., *Martensite*, Metals Park, OH: ASM, 1992.

J. Perkins, ed. *Shape Memory Effects in Alloys*. New York, NY: Plenum Press, 1975.

G. Thomas. "The Physical Metallurgy and Alloy Design of Dual Phase Steel," in *Frontiers in Materials Technologies*, M. A. Meyers and O. T. Inal, eds. Amsterdam: Elsevier, 1985, p. 89.

Exercises

11.1 Martensitic transformation involves the Bain transformation, shown schematically in Figure Ex11.1. The FCC structure is transformed into the BCC structure. Assuming that there is a 5% expansion in volume during the FCC-to-BCC transformation, (a) calculate the lattice parameter of the BCC structure in terms of a_0, and (b) determine the strains in the three orthogonal directions.

11.2 Plot hydrostatic strain versus carbon content for the martensitic transformation in steel from the plot shown in Ex11.2.

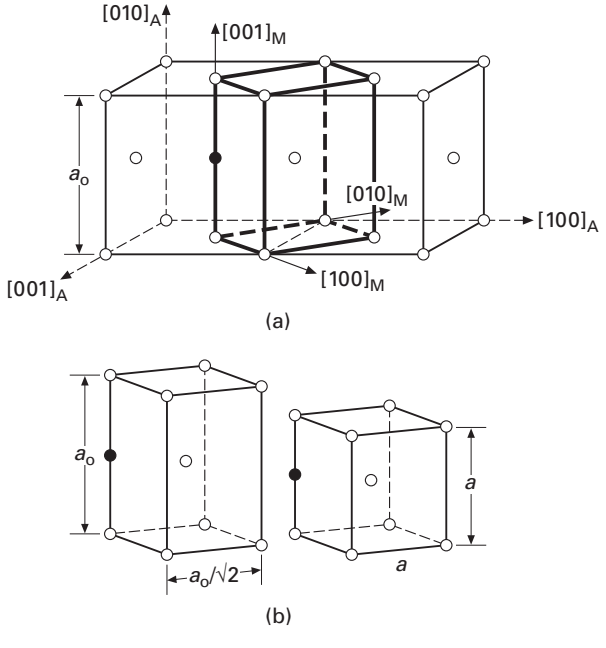

Fig. Ex11.1 Lattice correspondence for the formation of martensite in steels. (a) Body-centered tetragonal cell of axial ratio 2 outlined in austenite structure of cell size a_0. (b) Deformation carrying this structure into martensite cell with parameter a. Open circles are iron atoms; filled circles are one possible carbon site.

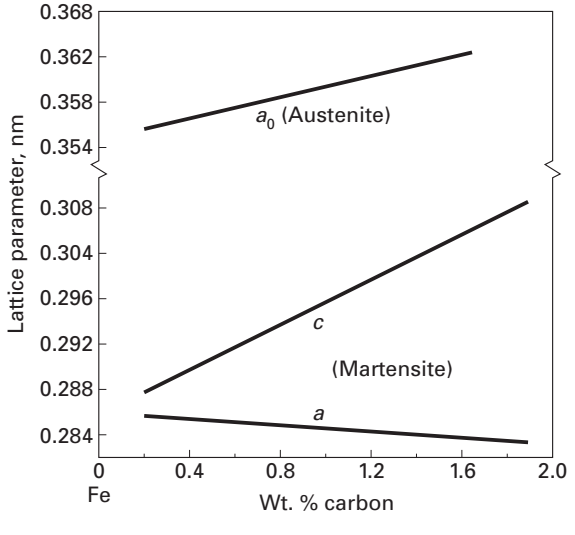

Fig. Ex11.2

11.3 From the data of Figure 11.12, estimate the M_s temperature of the alloy at zero stress.

11.4 The steel shown in Figure 11.15(b) has a plane strain fracture toughness of 110 MPa $m^{1/2}$ and a yield stress of 320 MPa. Will the cracks shown in the figure have a catastrophic effect if a specimen is stressed to 180 MPa?

11.5 Write down all the possible martensite variants for the Kurdjumov–Sachs orientation.

11.6 In addition to the commercial applications of shape-memory alloys described in the text, new developments are continuously taking place. Briefly describe three additional applications. (You may use L. M. Shetky, in *Intermetallic Compounds*, Vol. 2, J. L. Westbrook and R. L. Fleischer, eds. (New York: J. Wiley, 1994).)

11.7 Using Cu–Zn–Al, design a pen-drive system for an X–Y recorder. Based on the plot presented by L. M. Shetky (*Sci. Am.*, 241 (Nov., 1979) 74), what composition would you choose for the alloy?

11.8 Calculate the total strain energy associated with a martensite lens having a volume of 10 μm^3, assuming that all the energy is elastically stored. Specify the assumptions made; include both shear and longitudinal strain components from Equation 11.2.

11.9 Plot the stress required to form martensite as a function of temperature in Figure 11.16b.

11.10 (a) To what radius can a wire with diameter of 1 mm be curved using the superelastic effect if the maximum strain is approximately 0.05? (b) If the wire were made of a high-strength piano wire steel ($\sigma_y \sim$ 2GPa), what would be the minimum radius to which it could be curved? Take $E = 210$ GPa. (c) Discuss the differences obtained in (a) and (b).

11.11 What is the volume change associated with the tetragonal-to-monoclinic transformation in zirconia?
Given:

Monoclinic zirconia	Tetragonal zirconia
$a = 0.5156$ nm	$a = 0.5094$ nm
$b = 0.5191$ nm	$b = 0.5304$ nm
$c = 0.5304$ nm	
$\beta = 98.9^\circ$	

11.12 Give three technological applications (at least one of which is a bioengineering application) for shape-memory alloys.

Chapter 12

Special Materials: Intermetallics and Foams

12.1 Introduction

An intermetallic is a compound phase of two or more normal metals (ordered or disordered). Interest in intermetallics waned in the 1960s and 1970s. However, the demand for materials that are strong, stiff, and ductile at high temperatures has led to a resurgence of interest in intermetallics, especially silicides and ordered intermetallics such as aluminides. A testimony to this resurgence was the appearance in 1994 on the subject of a two-volume set by J. H. Westbrook and R. L. Fleischer, *Intermetallic Compounds: Principles and Practice* (New York: John Wiley). Intermetallic aluminides and silicides can be very oxidation and corrosion resistant, because they form strongly adherent surface oxide films. Also, intermetallics span a wide range of unusual properties. An important example outside the field of high-temperature materials involves the exploitation of martensitic transformations, exotic colors, and the phenomenon of shape memory in gold-based intermetallics in jewelry making. In what follows, we first describe the silicides, then the ordered intermetallics, and finally the basic structure and properties of foams.

12.2 Silicides

About 300 intermetallic compounds melt at temperatures above 1,500 °C. A survey of some silicide intermetallics for high-temperature applications showed that, based on criteria such as availability, phase changes in the temperature range of interest, and oxidation resistance, Ti_5S_3 and $MoSi_2$ seem to be the most promising materials: Ti_5Si_3 has the lowest density of all intermetallics, and $MoSi_2$ has a superior oxidation resistance. For service at temperature up to 1,600 °C, one needs characteristics such as high strength, creep resistance, fracture toughness, oxidation resistance, and microstructural stability. Figure 12.1 shows a plot of melting point vs. density for

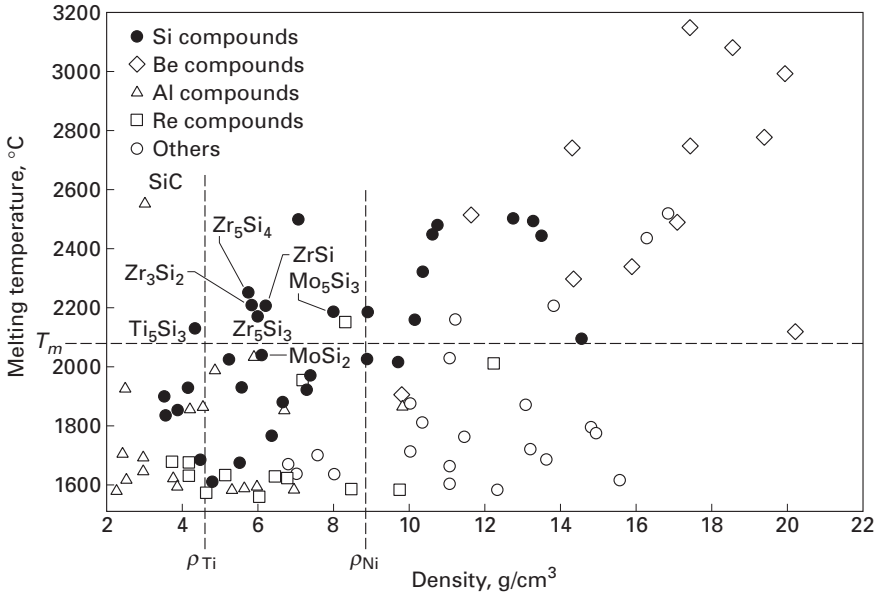

Fig. 12.1 A plot of melting point vs. density for intermetallics having $0.8T_m = 1{,}600$ °C. (After P. J. Meschter and D. S. Schwartz, *J. Minerals, Metals Materials Soc.*, 41 (Nov. 1989), 52.)

intermetallics having $0.8T_m = 1{,}600$ °C. Here we are assuming that intermetallics retain their strength up to temperatures of 80% T_m, the melting point of the material in K. This puts a lower limit on T_m equal to 2,067 °C for a service temperature of 1,600 °C. Also selected in the plot is an upper limit on density, viz., the density of nickel.

Molybdenum disilicide is a very promising intermetallic because of several of its characteristics. $MoSi_2$ has a tetragonal crystal structures, a high melting point, a relatively moderate density (6.31 g cm^{-3}), an excellent oxidation resistance, and a brittle-to-ductile transition at around 1,000 °C, which can result in high toughness at the service temperature. Among the problems associated with $MoSi_2$ are its rather low low-temperature toughness and low high-temperature strength. $MoSi_2$ shows a catastrophic oxidation behavior around 500 °C. In the literature, this problem has been termed pesting and is described as the retention of MoO_3 as an oxidation product at the grain boundaries. The expansion in volume accompanying the formation of MoO_3 results in severe microcracking. Among the efforts to ameliorate these problems, perhaps the most promising one is to use the approach of making a composite with $MoSi_2$ as a matrix. Table 12.1 summarizes the advantages and limitations of $MoSi_2$.

12.3 Ordered Intermetallics

In the simple description of crystal structure of metals given in Chapter 1, we tacitly assumed a *random* atomic arrangement of *A* and

Table 12.1 Advantages and Limitations of Monolithic $MoSi_2$

Advantages
Moderate density: 6.24 g/cm^3
High melting point: 2,020 °C
Outstanding oxidation resistance at <1,700 °C
Potential upper temperature limit: 1,600 °C
Deforms plastically above 1,000–1,200 °C
Amenable to electrodischarge machining (EDM)

Limitations
Low room-temperature fracture toughness (3.0 MPa m$^{1/2}$)
Low strength and creep resistance at elevated temperatures (e.g., 140 MPa at 1,200°C)

Table 12.2 Physical and Mechanical Properties of Important Intermetallic Compounds

	Density (g/cm^3)	Crystal Structure (Ordered)	Young's Modulus (GPa)	Coefficient of thermal expansion (10^{-6}/°C)	Tensile yield stress (MPa)	Melting point (°C)
Al_3Ti	3.4–4.0	DO_{22}(tetr.)	215	12–15	120–425	1350
TiAl	3.8–4.0	$L1_0$(tetr)	160–175	11.7	400–775	1480
Ti_3Al	4.1–4.7	DO_{19}(HCP)	120	12	700–900	1680
$MoSi_2$	6.1	Tetragonal	380–440	8.1–8.5	200–400	2020
Ni_3Al	7.4–7.7	$L1_2$(FCC)	180–200	14–16	200–900	1397
NiAl	5.9	B2(FCC)	177–190	14–16	175–300	1638
Ni_5Si_3	7.2		340	N/A	550	N/A
Fe_3Al	6.7	DO_3	140–170	19	600–1350	1540
FeAl	5.6–5.8	B2	160–250	21.5	500–700	N/A

B atoms in a unit cell of a metallic alloy consisting of atoms of species *A* and *B*. When *A* and *B* are arranged in a random manner, we have a *disordered alloy*. In such an alloy, equivalent crystallographic planes are statistically identical. Truly random – that is, completely disordered – alloys are not common, but there are many alloy systems that come close to having a random or disordered distribution of species *A* and *B*. It turns out that in a vast number of alloy systems, it is energetically favorable for atoms *A* and *B* to segregate to preferred lattice sites. Generally, such an ordered arrangement of atoms is obtained below a critical temperature T_c and in certain well-defined atomic proportions, i.e., stoichiometric compounds such as AB_3, *AB*, etc. Among examples of these systems, one may cite CuAu, Cu_3Au, Mg_3Cd, FeCo, FeAl, and aluminides of Ni and Ti. When the bonding is not totally metallic, but is partly ionic in nature, such an alloy is called an *intermetallic compound*. Table 12.2 gives a summary of important characteristics of

some intermetallics. In what follows, we examine (1) the differences in the dislocation behavior in ordered alloys vis-à-vis disordered, or ordinary, alloys, (2) the effect of ordering on mechanical behavior, and (3) efforts to enhance the low-temperature ductility of ordered alloys, with a special emphasis on nickel aluminide (Ni_3Al), which has some very unusual properties.

Example 12.1

Molybdenum disilicide shows a phenomenon called *pesting*. Describe this phenomenon and indicate some means of overcoming it.

Solution: It has been observed that at about 500 °C, $MoSi_2$ shows an accelerated oxidation. A product of this oxidation is MoO_3, which is accompanied by a rather large change in volume. This catastrophic oxidation can result in severe microcracking. Among some of the proposed remedies to overcome pesting are the following:

- Preoxidize the $MoSi_2$, to form a continuous SiO_2 surface film.
- Minimize porosity, to minimize the formation of MoO_3 at the pore surfaces.
- Use alloying to alter the oxidation characteristics of $MoSi_2$.
- Use metal coatings.

Example 12.2

There is some interest in the use of gold-based intermetallic alloys in the jewelry industry. Can you describe some other possibilities in this area?

Solution: Platinum-based intermetallic alloys represent a possibility. Platinum is a soft metal like gold, but has a silver-like color. Thus, platinum alloys based on a $PtAl_2$ intermetallic may be of interest because they show a higher hardness than Pt and they can range in color from orange through pink to the yellow of pure gold.[1]

12.3.1 Dislocation Structures in Ordered Intermetallics

There are some very important differences between the dislocation structures observed in common metals and those in ordered intermetallics. In FCC metals, dislocations split into partials, and the partials are separated by a stacking-fault ribbon. (See Chapter 4.) The partials, however, are confined to a single slip plane and do not have

[1] J. Hurly and P. T. Wedepohl, *J. Mater. Sci.*, 28 (1993) 5648.

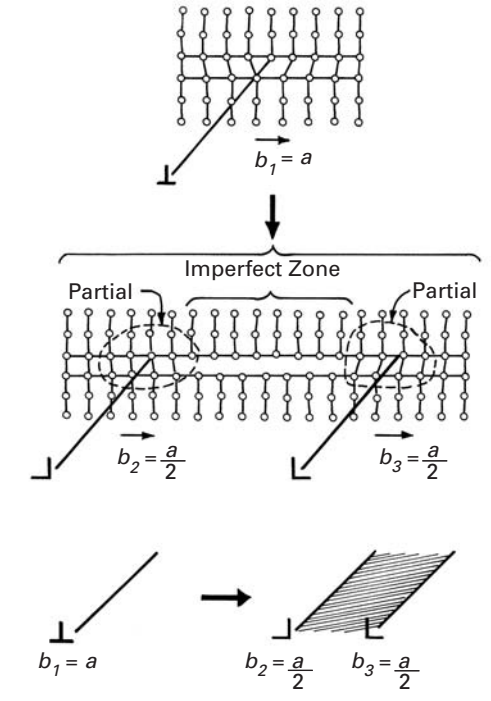

(a)

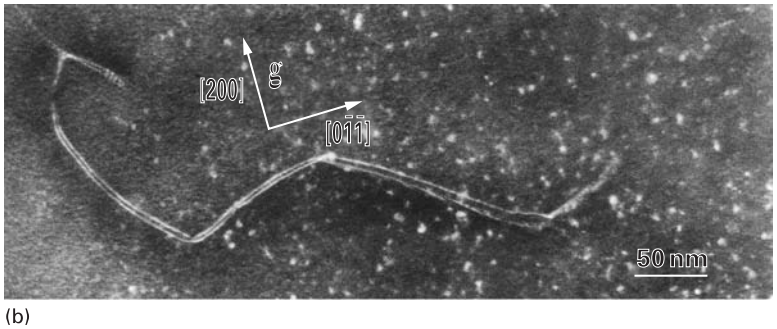

(b)

Fig. 12.2 The characteristic dislocation structure in an ordered alloy consists of two superpartial dislocations, separated by a faulted region or an antiphase boundary (APB). (b) Superpartial dislocations separated by approximately 5 nm in Ni_3Al deformed at 800 °C; $b = [110]$ and superpartials $b_1 = b_2 = \frac{1}{2}[110]$. (Courtesy of R. P. Veyssiere.)

parallel Burgers vectors. As illustrated in Figure 12.2, the characteristic dislocation structure in an ordered alloy consists of two partial dislocations separated by a faulted region or what is also called an *antiphase boundary* (APB). Figure 12.2(b) shows an example of partial dislocations separated by a faulted region of 5 nm width in Ni_3Al deformed at 800 °C.

An ordered structure results in some interesting characteristics. The ordered state in A_3B-type alloys is a low-energy state, so the movement of dislocations and vacancies results in a destruction of the local order; that is, a higher energy state is produced. Thus, activities such as dislocation motion and vacancy migration are subject to some restrictions. For example, in ordered structures, the dislocations

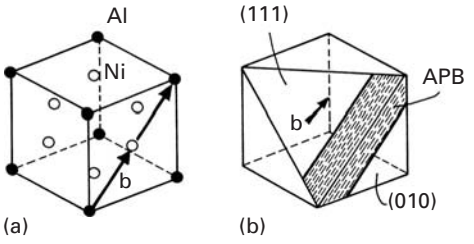

Fig. 12.3 (a) The $L1_2$ crystal structure of Ni_3Al. The aluminum atoms are located at the corners of a cube, while the Ni atoms are at the centers of the faces. (b) A (111) slip plane and the slip direction <010>, consisting of two 1/2<110> vectors, in Ni_3Al. Note that the APB in between the two superpartials lies partly on the (111) and partly on the (010) face.

must travel in pairs – a leading dislocation and a trailing dislocation. The passage of a leading dislocation destroys the order, while the passage of a trailing dislocation restores it. Also, thermally activated phenomena, such as diffusion via vacancies, suffer retardation.

Let us consider the ordered Ni_3Al intermetallic. The $L1_2$ crystal structure of Ni_3Al is shown in Figure 12.3(a). The aluminum atoms are located at corners of cubes, while the Ni atoms are at the centers of the faces of the cube. Figure 12.3(b) shows a (111) slip plane and the slip direction <010>, consisting of two $\frac{1}{2}$<010> vectors, in Ni_3Al. Note that the APB in between the two partials lies partly on the (111) and partly on the (110) face. Interestingly, the partials in this case have the same Burgers vectors (along the screw direction). These partials can extend to any slip plane that contains the dislocation line or Burgers vector. The APB can be transferred from one plane to the other by cross-slip of the partial screws. This situation allows the partials to reduce the energy of the intermetallic by extending to the plane with a minimum APB energy, because the configurational energy decreases with decreasing APB energy. When a pair of screw partials is fully transferred from the (111) plane to the cross-slip plane (010), we get what is called *Kear–Wilsdorf* lock.[2] We can estimate the energy change associated with this lock in the following way. The APB, a kind of stacking fault, results in an energy increase that is proportional to the quantity $(E_{AA} + E_{BB} - 2E_{AB})$, where E_{AA}, E_{BB}, and E_{AB} are the bonding energies of *AA*, *BB*, and *AB* pairs, respectively. The superpartials of a pair repel each other elastically, but are held together by the APB. If r is the separation between two superpartials, the interaction energy is given by $-K \ln r$, where K is a constant involving elastic constants of materials and the character of the dislocation. If γ is the surface energy of the APB, then the energy of an APB of width r is γr. Thus, the energy of a pair of superpartials with an APB of width r can be

[2] B. H. Kear and H. G. F. Wilsdorf, *Trans. AIME*, 224 (1962) 382.

written as

$$E(r) = \gamma r - K \ln r. \tag{12.1}$$

At the equilibrium separation r_0, the two components of the energy balance, and we can write

$$dE/dr = 0 = \gamma - K/r_0, \tag{12.2}$$

or

$$\gamma = K/r_0.$$

From Equations 12.1 and 12.2, we get, at $r = r_0$, the equilibrium energy

$$E(r_0) = (K/r_0)r_0 - K \ln(K/\gamma).$$

or

$$E(r_0) = K[1 + \ln(\gamma/K)]. \tag{12.3}$$

Applying Equation 12.3 to the primary and cross-slip planes, we can write:

For primary slip

$$E_p(r_0) = K[1 + \ln(\gamma_p/K)].$$

For cross-slip

$$E_c(r_0) = K[1 + \ln(\gamma_c/K)].$$

Hence

$$\Delta E(r_0) = E_c(r_0) - E_p(r_0) = K[\ln(\gamma_c/K) - \ln(\gamma_p/K)].$$

Thus, the energy associated with the Kear–Wilsdorf lock may be written as

$$\Delta E = K \ln \lambda,$$

where $\lambda = \gamma_c/\gamma_p$, in which the subscripts c and p represent the cross-slip and primary planes, respectively. Kear–Wilsdorf locks harden the intermetallic because they inhibit slip; as λ decreases, the tendency to form these locks increases.

There are some other differences between intermetallics and common alloys. Generally, common disordered alloys show an isotropic behavior, whereas most intermetallic compounds have anistropic elastic properties. This can result in excessive elastic strain on certain planes; in particular, it can introduce shear stresses perpendicular to screw dislocation lines. These dislocations not only will repel each

other along the radial directions, but also will exert a torque on each other.[3]

12.3.2 Effect of Ordering on Mechanical Properties

Mechanical properties of an alloy are altered when it has an ordered structure. We define the degree of long-range order (LRO) by means of a parameter

$$S = \frac{r - f_A}{1 - f_A}, \tag{12.4}$$

where r is the fraction of A sites occupied by A atoms and f_A is the fraction of A atoms in the alloy. Thus, S goes from 0 (completely disordered) to 1 (perfectly ordered). Different dislocation morphologies observed in ordered alloy.

A superdislocation (i.e., closely spaced pairs of unit dislocations bound together by an antiphase boundary) in a perfectly ordered crystal and a single dislocation in a completely disordered crystal will both experience less friction stress than either of them will experience at an intermediate degree of order S. Thus, qualitatively, one would expect a yield stress maximum at an intermediate degree of order (i.e., the change in yield stress is not directly related to the degree of ordering). For example, Cu_3Au crystals show a lower yield stress when fully ordered than when only partially ordered. Experiments showed that this results from the fact that the maximum in strength is associated with a critical domain size. Short-range order (SRO) results in a distribution of neighboring atoms that is not random. Thus, the passage of a dislocation will destroy the SRO between the atoms across the slip plane. The stress required to do this is large. A crystal of Cu_3Au in the quenched state (SRO) has nearly double the yield stress of that in the annealed (LRO). The maximum in strength is exhibited by a partially ordered alloy with a critical domain size of about 6 nm. The transition from deformation by unit dislocations in the disordered state to deformation by superdislocations in the ordered state gives rise to a peak in the curve of flow stress versus degree of order.

The presence of atomic order leads to a marked change in the flow curve of the alloy. Figure 12.4 shows the flow curves of a fully ordered FeCo alloy at low temperatures, where the order is not affected. Stage I is associated with a well-defined yield point. This is followed by a high linear work-hardening stage, II. Finally, there occurs stage III, with nearly zero work-hardening. The stress–strain curves of the same alloy in the disordered state are shown in Figure 12.5. The curves in Figure 12.4 (ordered) are markedly different from the ones in Figure 12.5 (disordered). The sharp yield point and stage II are absent in the disordered alloy, which goes straight into stage III after gradual yielding. Fully ordered alloys deform by means of the movement of superlattice dislocations at rather low stresses. However, the superdislocations

[3] M. H. Yoo, *Acta Met.*, 35 (1987) 1559.

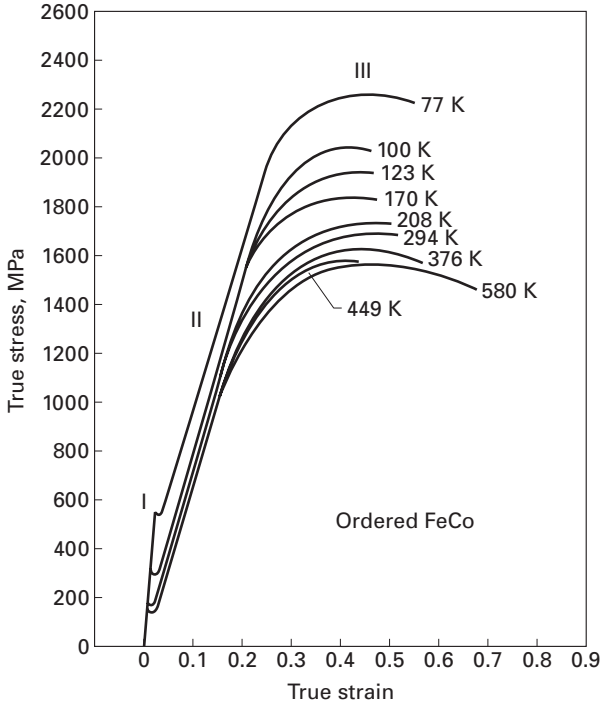

Fig. 12.4 Stress–strain curves of ordered FeCo alloys at different temperatures. (Adapted with permission from S. T. Fong, K. Sadananda, and M. J. Marcinknowski, *TransAIME*, 233 (1965) 29.)

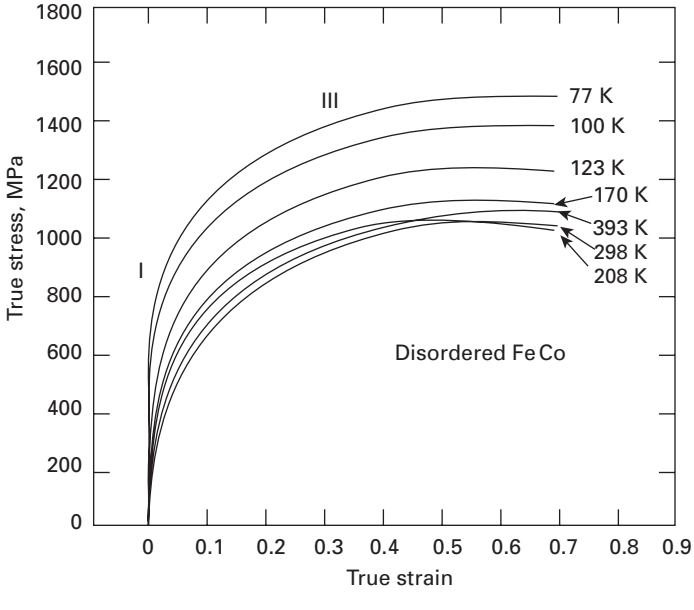

Fig. 12.5 Stress–strain curves of fully disordered FeCo alloys at different temperatures. (Adapted with permission from S. T. Fong, K. Sadananada, and M. J. Marcinkowski, *TransAIME*, 233 (1965) 29.)

must move as a group in order to maintain the ordered arrangement of atoms. This makes cross-slip difficult. Long-range order thus leads to high strain-hardening rates and frequently, to brittle fracture.

Figure 12.6 shows this effect of ordering on uniform elongation of FeCo–2% V at room temperature. The ductility of the alloy decreases with increasing LRO. Mg_3Cd is the only known exception to this

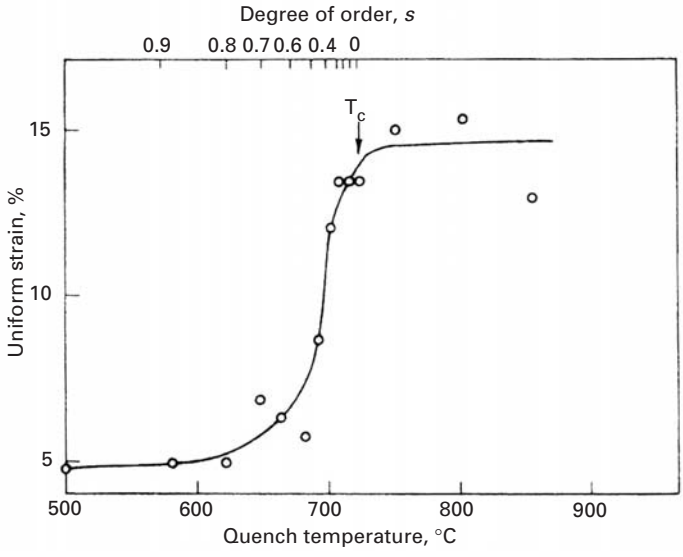

Fig. 12.6 Effect of atomic order on uniform strain (ductility) of Fe–Co–2% V at 25 °C. (Adapted with permission from N. S. Stoloff and R. G. Davies, *Acta Met.*, 12 (1964) 473.)

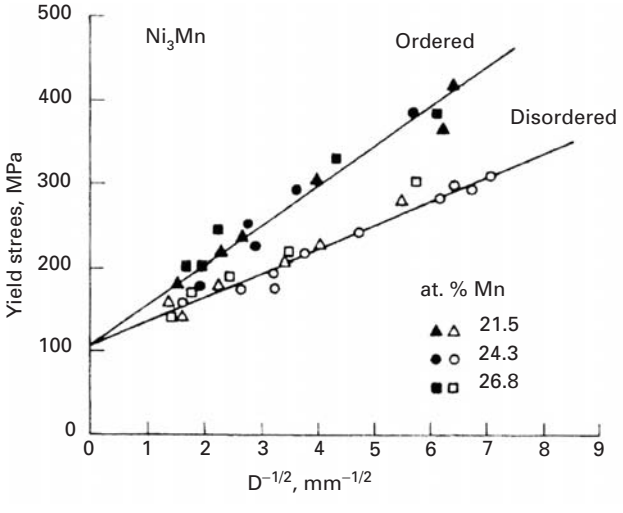

Fig. 12.7 Hall–Petch relationship for ordered and disordered alloys. (Adapted with permission from T. L. Johnston, R. G. Davies, and N. S. Stoloff, *Phil Mag.*, 12 (1965) 305.)

tendency toward brittleness, because of a restricted number of slip systems or less easy cross-slip.

Ordered alloys such as FeCo and Ni_3M obey the Hall–Petch relationship between flow stress and grain size; viz., (see Chapter 5)

$$\sigma = \sigma_0 + kD^{-1/2},$$

where σ is the flow stress at a given strain, σ_0 and k are constants for that strain, and D is the grain diameter. In these alloys, long-range order increases k, as shown in Figure 12.7 for Ni_3Mn. This increase in k with long-range order can be explained by the change in the number of slip systems with order, since the ease of spreading of slip across boundaries is controlled by the degree of order.

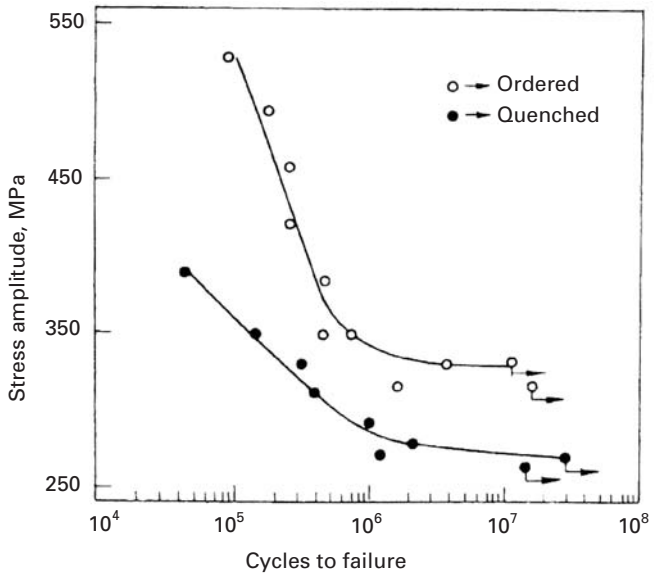

Fig. 12.8 Effect of atomic order on fatigue behavior of Ni_3Mn. (Adapted with permission from R. C. Boettner, N. S. Stoloff, and R. G. Davies, *Trans. AIME*, 236 (1968) 131.)

The effect of atomic ordering on fatigue behavior is shown in Figure 12.8 in the form of stress (S) vs. cycles to failure (N) (see Chapter 14 for S–N curves) for ordered and disordered Ni_3Mn. The improved fatigue performance in the ordered state is explained by difficulty of cross-slip and a decrease in slip-band formation in that state. Slip bands lead to the formation of extrusions and intrusions on the sample surface, which in turn lead to fatigue crack nucleation. (See Chapter 14.)

Gamma-prime-strengthened superalloys are an example of the effect of ordering on strength. The Ni_3Al precipitate produces very low coherency stresses and is coherent with the austenitic matrix. The strengthening effect is clearly evident in Figure 12.9(a), which shows the strength of the austenitic matrix and Ni_3Al separately, and the strength of MAR M-200, composed of 65 to 85% gamma prime (the ordered Ni_3Al). In ordered structures, it is energetically favorable for dislocations to move in groups, forming antiphase boundaries between them as seen in Section 12.3. The equilibrium distance between the pairs, as well as their form, was found to depend on the particle size, particle distribution, energy of the antiphase boundary, elastic constants, and external shear stress. The preceding parameters are part of the equations derived by Gleiter and Hornbogen[4] for the increase in the critical resolved shear stress, $\Delta\tau$ or ΔCRSS. The results of calculations are compared with observed results for a Ni–Cr–Al alloy in Fig. 12.9(b), where δ is the atomic percent aluminum. The experimental results are marked by dots and triangles; they refer to 0.5 and 1.8% aluminum, respectively. The correlation is good, and maximum strengthening is obtained for particles having a diameter of 10 nm.

[4] H. Gleiter and E. Hornbogen, *Phys. Status Solids*, 12 (1965), 235, 251.

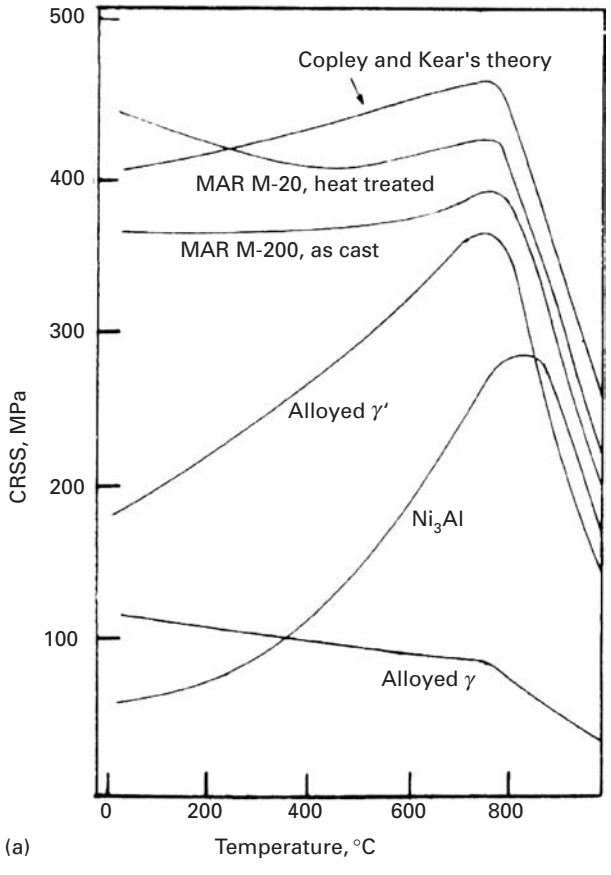

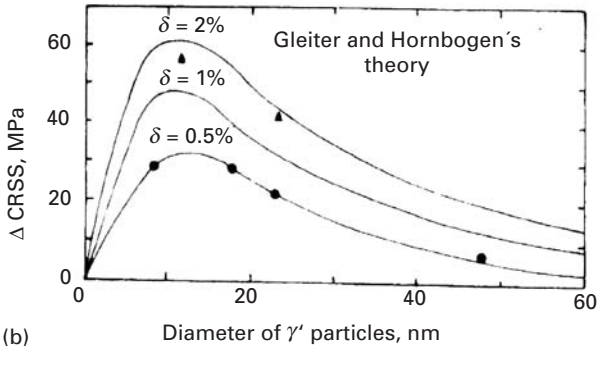

Fig. 12.9 (a) Effect of temperature on CRSS for Ni_3Al, γ, and Mar M-200 superalloy ($\gamma + \gamma'$). (Adapted with permission from S. M. Copley and B. H. Kear, *Trans. TMS-AIME*, 239 (1967) 987.) (b) Calculated and observed increase in the critical resolved shear stress (CRSS) in an Ni–Cr–Al alloy as a function of the diameter of the precipitate; full lines represent calculations (●, $\delta =$ 0.5% Al; ▲, $\delta =$ 1.8% Al); δ is atomic percent aluminum. (Adapted with permission from H. Gleiter and H. Hornbogen, *Phys. Status Solids*, 12 (1965) 235.

Another outstanding property of Ni_3Al and some other intermetallics is the increase in yield stress with temperature. As is seen from Figure 12.9(a), the yield stress increases by a factor of 5 when the temperature is raised from ambient temperature to 800 °C. This temperature dependence is unique and contrary to what would be expected on the basis of thermally activated motion of dislocations. (We discuss this and other aspects of ordered intermetallics in Section 12.3.3.) Thus, in spite of the normal temperature dependence

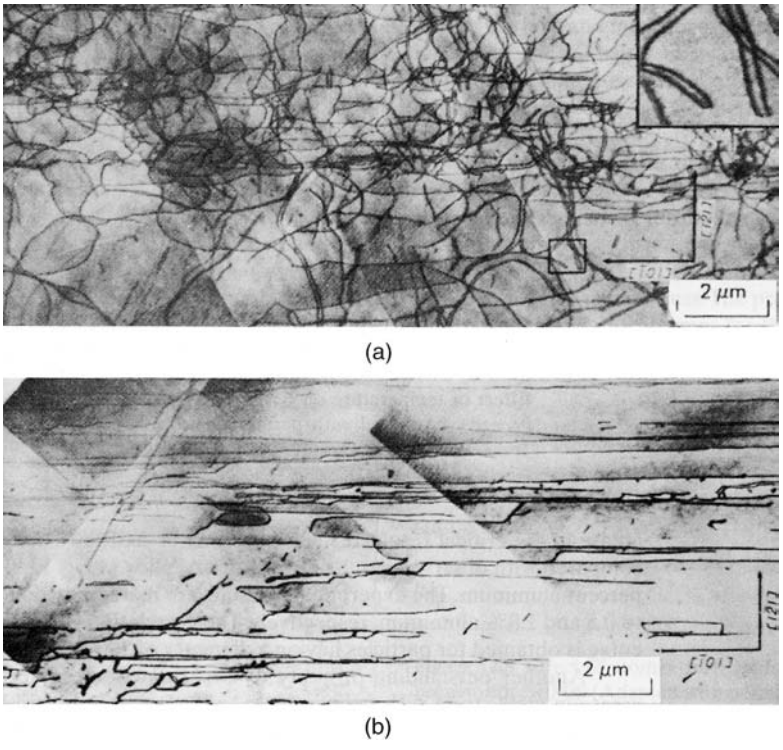

Fig. 12.10 Effect of deformation temperature on the dislocation arrangement in the {111} primary slip plane of ordered Ni_3Ge. (a) $T = -196\ ^\circ C$, $\varepsilon_p = 2.4\%$. (b) $T = 27\ ^\circ C$, $\varepsilon_p = 1.8\%$. (Courtesy of H.-R. Pak.)

of the austenite (also shown in Figure 12.9(a)), the alloy Mar M-200 exhibits a constant yield stress up to 800 °C; the decrease in the flow stress of γ is compensated for by the increase of γ' (Ni_3Al). It is interesting to note that other ordered alloys, such as Cu_3Au and Ir_3Cr, do not exhibit this unique behavior, while Ni_3Ge, Ni_3Si, Co_3Ti, and Ni_3Ga do. High voltage TEM work on Ni_3Ge has shown dramatic changes in dislocation configuration. For Ni_3Ge, it was found that the substructure at −196 °C consisted roughly of an equal number of edge and screw dislocations, while at 27 °C it consisted mostly of screw dislocations aligned along [101]. (See Figure 12.10.) Thus, the decreased mobility of screw dislocations with increasing temperature was responsible for the strengthening effect. At temperatures above the one providing maximum strength, the change in slip plane from {111} to {100} would be responsible for the decrease in strength. This explanation is different from the one previously provided.

It is this very unusual behavior – the increase in flow stress with temperature – that makes nickel aluminides very attractive for high-temperature applications. Ni_3Al remains ordered up to its melting point (1,400 °C) and also shows an increasing yield strength with temperature. A decrease in yield strength occurs at very high temperatures due to the start of thermally activated slip on {100} planes, and not because of disorder.

Long-range ordered alloys of the Ni_3Al type show some important and unique features alluded to earlier, such as an increasing yield stress with increasing temperature. The problem with these alloys,

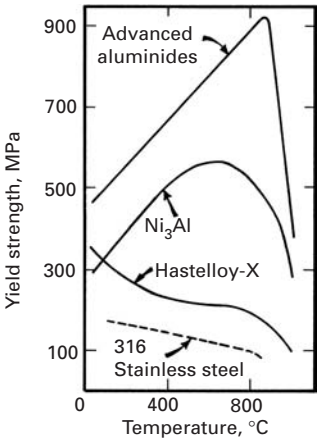

Fig. 12.11 Yield stress as a function of test temperatures for Ni_3Al-based aluminide alloys. Hastelloy-X, and type 316 stainless steel. (Adapted from C. T. Liu and J. O. Stiegler, *Science*, 226 (1984) 636.)

however, is their lack of ambient temperature ductility. Figure 12.11 shows yield strength as a function of temperature for Ni_3Al-based alloys, Hastelloy-X, and type 316 stainless steel. It is not surprising that $L1_2$-type intermetallics are major candidates for use at elevated temperatures, about 900–1000 °C.

The anomalous yield behavior of Ni_3Al has been the subject of a number of investigations. At temperatures $T < T_p$, slip occurs mainly on the octahedral {111} planes, while at temperatures $T > T_p$, slip becomes dominant on cubic {100} planes. T_p is the temperature corresponding to the maximum in strength ≈800 °C. Sun and Hazzledine used weak-beam TEM to identify dislocation structures with low mobilities in Ni_3Al-type ordered intermetallics.[5] They observed that in the region of yield stress anomaly, a kink mechanism unlocks the Kear–Wilsdorf locks described earlier. This mechanism leads to the formation of special kink configurations with switched superpartials, as well as the formation of what are called APB tubes. In summary, the increase in yield strength below T_p is related to the formation of K–W locks (lowering of λ) while the decrease in yield strength above T_p is attributed to the change of slip from {111} <110> to {100} <110>. (See Figure 12.3.)

12.3.3 Ductility of Intermetallics

As we have seen, many alloy systems of the general composition A_3B have an ordered structure formed by regular stacking of close-packed layers. The stacking sequence, however, can range from the more common cubic or hexagonal to less common and more complex transition structures with unit cells extending over 15 layers. Such intermetallics are generally quite brittle at low temperatures, which makes their processing very difficult. There are two common causes of brittleness in intermetallics:

1. The crystal structure is of low symmetry; that is, not enough slip systems are available for general plastic deformation to occur. As is well known, one needs at least five independent systems for an arbitrary change in shape to occur.
2. Enough slip systems are available, but there are crack propagation paths along the grain boundaries that are easy to take and that will cause embrittlement.

Generally, ordered hexagonal alloys have very limited ductility and ability to process while ordered cubic alloys have good ductility. Various researchers have tried to make ordered intermetallics more ductile by different approaches. Baker and Munroe[6] classify these attempts into four categories: microalloying, macroalloying, processing-induced microstructure control, and fiber reinforcement. We summarize these efforts next.

[5] Y. Q. Sun and P. M. Hazzledine, in *High Temperature Ordered Intermetallic Alloys* (Dordrecht, The Netherlands, Kluwer, 1992), p. 177.

[6] I. Baker and P. R. Munroe, *Journal of Metals*, 40 (Feb. 1988) 28.

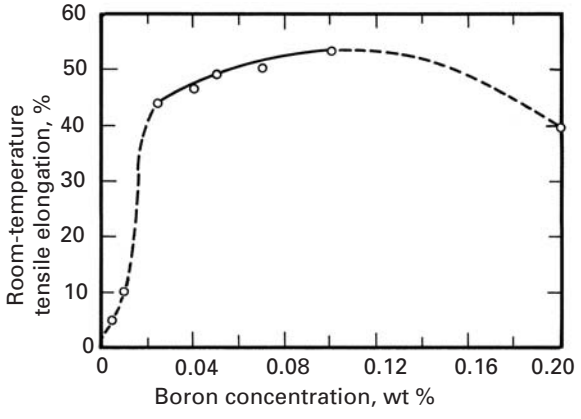

Fig. 12.12 Restoration of room-temperature ductility in Ni_3Al as a function of boron content. (After K. Aoki and O. Izumi, *Nippon Kinzoku Takkasishi*, 43 (1979) 1190.)

Microalloying

An examination of the Ni–Al phase diagram shows four intermetallics: $NiAl_3$, Ni_2Al_3, NiAl, and Ni_3Al. Ni_3Al is nothing but γ', the strengthening phase in many Ni-based superalloys meant for high-temperature use as described earlier. Ni_3Al has an $L1_2$ crystal structure with Al atoms at the cube corners and Ni atoms at the face-centered positions. (See Figure 12.3a.) Single-crystal Ni_3Al is very ductile at and below room temperature. Its ductility decreases with temperature until the peak in yield strength occurs. In polycrystalline form, nickel aluminide has practically no ductility at room temperature. Ni_3Al does possess five independent slip systems of the type <111> {110}, which is the condition for generalized plastic flow, as per von Mises criterion. Instead of high ductility, polycrystalline Ni_3Al shows intrinsic grain-boundary weakness, as evidenced by its tendency toward brittle, intergranular fracture at room temperature. It turns out that boron is a very effective dopant for restoration of ductility in Ni_3Al. Boron-free polycrystals fracture without any plastic yielding, and very small additions of boron can lead to dramatic results. As little as 0.05% wt.% B can improve the strain to failure from nearly 0 to 50% and can alter the fracture mode from intergranular to transgranular. Figure 12.12 shows this restoration of room-temperature ductility in Ni_3Al as a function of boron content. Note the very small amount of boron required to do the job. As the figure reveals, boron-doped Ni_3Al shows a broad maximum in strength. The poor ductility of intermetallics and the effect of boron are generally explained in terms of environmental effects, especially moisture. (See the end of this section.)

Intergranular failure at room temperature also has been attributed to the segregation of impurities such as sulfur to grain boundaries. In one experiment, a decrease in ductility was measured as the sulfur content of the Ni_3Al increased from 32 to 176 ppm by weight. Auger electron spectroscopy showed that sulfur did indeed segregate to grain boundaries. Attempts at purifying Ni_3Al to restore its ductility have not worked in practice.

Macroalloying

Macroalloying additions (less than 1 at.%) have been used to introduce modifications in intermetallics that lead to enhanced ductility. Such modifications include changing the crystal structure to one of higher symmetry, promoting the operation of additional or different slip systems, and other changes.

Alloys of the (Ni, Co, Fe)$_3$V system can have ordered structure (cubic, hexagonal, or more complex transitional). The ordered hexagonal structure is too brittle for processing. Macroalloying can be used to create a window in the composition space in the (Ni, Co, Fe)$_3$V system that has an intrinsically ductile, ordered cubic structure. An important parameter in the characterization of intermetallics is the electron concentration (e/a), which is the number of valence electrons per atom. Ordered structures of the type A_3B are built by stacking close-packed layers. The stacking sequence is influenced by the atomic radius ratio (R_a/R_0) and the electron concentration. In the (Ni, Co, Fe)$_3$V system, nickel, cobalt, and iron have about the same atomic size. Thus, these elements influence the crystal structure through their electronic effects. If a portion of Co in (Fe, Co)$_3$V is replaced by an equal number of Ni and Fe atoms, then we shall have altered the composition of the compound, but not the e/a ratio. In Co$_3$V, a six-layer stacking sequence occurs, with one-third of the layers having a hexagonal character (*ABABAB* . . .) and two-thirds of the layers having a cubic character (*ABCABC* . . .). Replacing Co by Ni gives a higher e/a ratio and a predominantly hexagonal stacking first, followed by fully hexagonal stacking. A reduction in the e/a ratio to 7.89 or less gives an cubic ordered structure ($L1_2$). Thus, one can choose a suitable combination of Ni, Co, and Fe to obtain the desirable cubic ordered structure (the same as that of Cu$_3$Au).

Titanium-based alloys are lighter than Co-based and Ni-based superalloys. However, the service temperature of Ti-based alloys is less than 500 °C. TiAl and Ti$_3$Al, the aluminides of titanium, have lower densities, higher stiffness, and higher use temperatures than nickel aluminides. Titanium aluminides show good oxidation resistance up to 900 °C, but have poor ductility and strength at low temperatures. Additions of β-stabilizing elements such as Nb, Mo, and W can result in some improvement in ductility in Ti$_3$Al. However, such macroalloying additions of heavier elements are accompanied by a penalty on density.

Processing–induced microstructural control

Polycrystalline nickel aluminides are brittle at room temperature. Single-crystal nickel aluminides, however, are ductile. One very straightforward approach would be to use single crystals of these materials. Another approach is to combine grain refinement with another ductility-enhancing feature, such as a martensitic transformation. A fine grain size would result in slip homogenization, eliminate grain boundary segregation, and allow enough deformation for

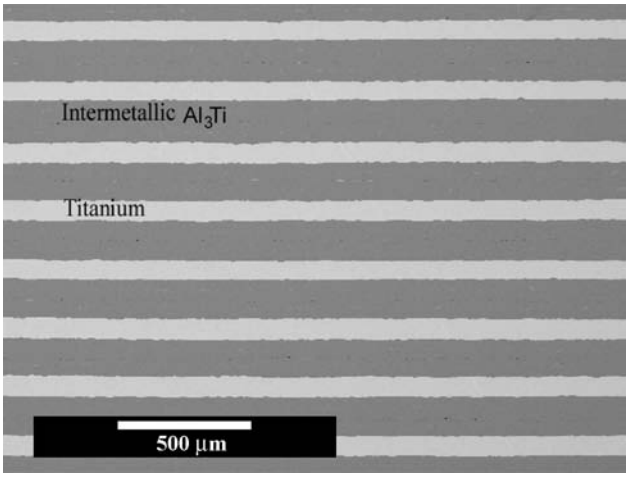

Fig. 12.13 Al_3Ti–Ti laminate composite. (Courtesy of K. S. Vecchio.)

the martensitic transformation to be induced. In principle, such a technique should work for any intermetallic. In practice, though, the grain size required for ductility may be too small (perhaps less than 1 μm) and thus difficult to achieve. An example of the beneficial effect of fine grain size is the use of rapid solidification technology to produce very fine grains in Ti_3Al. The reader should be cautioned, however, that although a grain refinement can lead to improvement in low-temperature properties, it can result in rather poor creep properties at high temperature because of the grain-boundary-related creep processes. (See Chapter 13.)

Ordered iron aluminides based on Fe_3Al also offer oxidation resistance and low material cost, but have limited ductility at ambient temperatures. In addition, the strength drops drastically above 600 °C. Sikka used thermomechanical processing to improve room-temperature ductility in iron aluminides.[7] A suitable combination of melting practice, processing, heat treatments, and test conditions resulted in 15–20% room-temperature elongation values. The recipe involves an alloy lean in alloying elements, vacuum melting, an unrecrystallized or only slightly recrystallized microstructure, oil quenching after heat treatment, higher-than-normal strain rates, and a moisture-free environment.

Composite route

This approach involves the use of fibers or layers to toughen the intermetallics. The idea is the same as that in ceramic matrix composites – viz., provide a weak interface ahead of a propagating crack, and thus bring into play a variety of energy-dissipating processes such as crack deflection, fiber pullout, etc. (See Chapter 15.)

Figure 12.13 shows a laminate composite in which the intermetallic compound Al_3Ti is the hard phase and titanium is the ductile

[7] V. K. Sikka, *Sampe Quarterly*, 22 (July 1991) 2.

component. The insertion of the metallic component increases the toughness of Al_3Ti dramatically. The propagation of cracks is hindered by the ductile component, which arrests them. An important problem to be considered with care when designing intermetallic-based composites is the mismatch in thermal expansion coefficient. When the composite is cooled down from the processing temperature to ambient temperature, the mismatch in thermal expansion coefficient can generate large internal stresses. One should design the composite in such a manner that the intermetallic matrix is not in tension. Putting the intermetallic in tension is not a desirable situation because intermetallics tend to be stronger in compression than in tension. This can generate tensile cracks within the intermetallic.

Environmental effects in intermetallics

There is evidence that the poor ambient ductility encountered in ordered intermetallics is due mainly to environmental effects.[8] Both moisture and hydrogen, at levels found in ambient air, are thought to be responsible for inducing embrittlement in ordered intermetallics. In the case of water vapor, the phenomenon involves the reaction of reactive elements in the intermetallics with the ambient water vapor, to form an oxide (or hydroxide) and generate atomic hydrogen, which leads to a loss of ductility accompanied by a change in fracture mode from transgranular to intergranular. In the case of H_2, atomic hydrogen is produced by dissociation of physisorbed hydrogen molecules on intermetallic surfaces. It would thus appear that the main reason for the efficacy of boron in rendering Ni_3Al more ductile is that boron suppresses the environmental embrittlement, possibly by slowing diffusion of hydrogen.

Iron aluminides based on Fe_3Al are also sensitive to environmental effects. A major problem again is the ever-present moisture in the air. The water vapor reacts with aluminum to produce hydrogen at the surface of the metal. This hydrogen is adsorbed in the aluminide during plastic deformation, leading to low ambient ductility.

Example 12.3

What is the source of the excellent high-temperature oxidation resistance shown by aluminides of nickel, cobalt, and iron?

Solution: Although the aluminides are quite brittle, they readily form a layer of alumina at high temperatures. The alumina layer provides the excellent oxidation resistance up to 1,000 °C. Such aluminides are used as coatings on gas turbine components. Kanthal alloys used for heating elements are also based on iron aluminides.

[8] E. P. George, C. T. Liu, H. Lin, and D. P. Pope, *Mater. Sci. & Eng.*, A192 (1995) 277; E. P. George, C. T. Liu, and D. P. Pope, *Acta Met.*, 44 (1996) 1757.

12.4 Cellular Materials

12.4.1 Structure

Many naturally occurring materials are not fully dense, i.e, they possess internal voids. This type of design is intentional, since it reduces the density. Examples are cork, bones, wood, sponge, and plant stalks and they are shown in Figure 12.14. Figure 1.32 shows also synthetic aluminum sponge as well as the cellular core in a toucan's beak. This form has been adopted in modern synthetic materials, and we have metallic, ceramic, and polymeric foams. Some are of common and every day usage, such as Styrofoam. Others are quite esoteric, such as the space shuttle tiles, which have a density of 0.141 g/cm^3 and can withstand a maximum temperature of 1260 °C. These tiles, made from silica fiber, prevent the shuttle from burning up during the reentry phase of space travel. The intense heat generated from friction with the atmosphere, at high velocities, would otherwise be fatal. This was demonstrated by the *Columbia* tragedy, in which a few tiles were knocked out during takeoff. Each space shuttle has 70% of its external surface protected by tiles (24,000 tiles per orbiter). Aluminum foam is commercially fabricated in relative densities (defined as the density of the cellular material/density of solid) varying between 0.033 and 0.1; the pore sizes can be varied independently. The aluminum foam shown in Figure 1.33 has a relative density of 0.07.

An example of a biological cellular material is bone. Bone is designed to have a variable density. Regions subjected to higher stress are denser. The outside surface is made of high density material and is called compact bone. The inside of bone tends to have a lower density and is termed cancellous bone. Figure 12.15 shows the cross section of a tibia and a glassy foam.

The mechanical properties of cancellous bone (and, for that matter of all cellular materials) are very sensitive to the relative density. Some marked effects shown by their stress–strain curves, are (see Figure 12.16):

a. Young's modulus increases with increasing relative density.
b. Plastic collapse plateau increases with relative density.
c. Densification stage.

There are numerous other examples of synthetic cellular materials. These cellular materials are used either by themselves or as a core in sandwich arrangements. Sandwich structures range from common cardboard used in packaging to important uses in the aircraft industry. The basic idea is to have a dense skin and a light-weight interior. They are briefly described in Section 1.3.8.

12.4.2 Modeling of the Mechanical Response

The compressive stress–strain curves of cellular materials have three characteristic regions: (a) an elastic region, (b) a collapse plateau, and

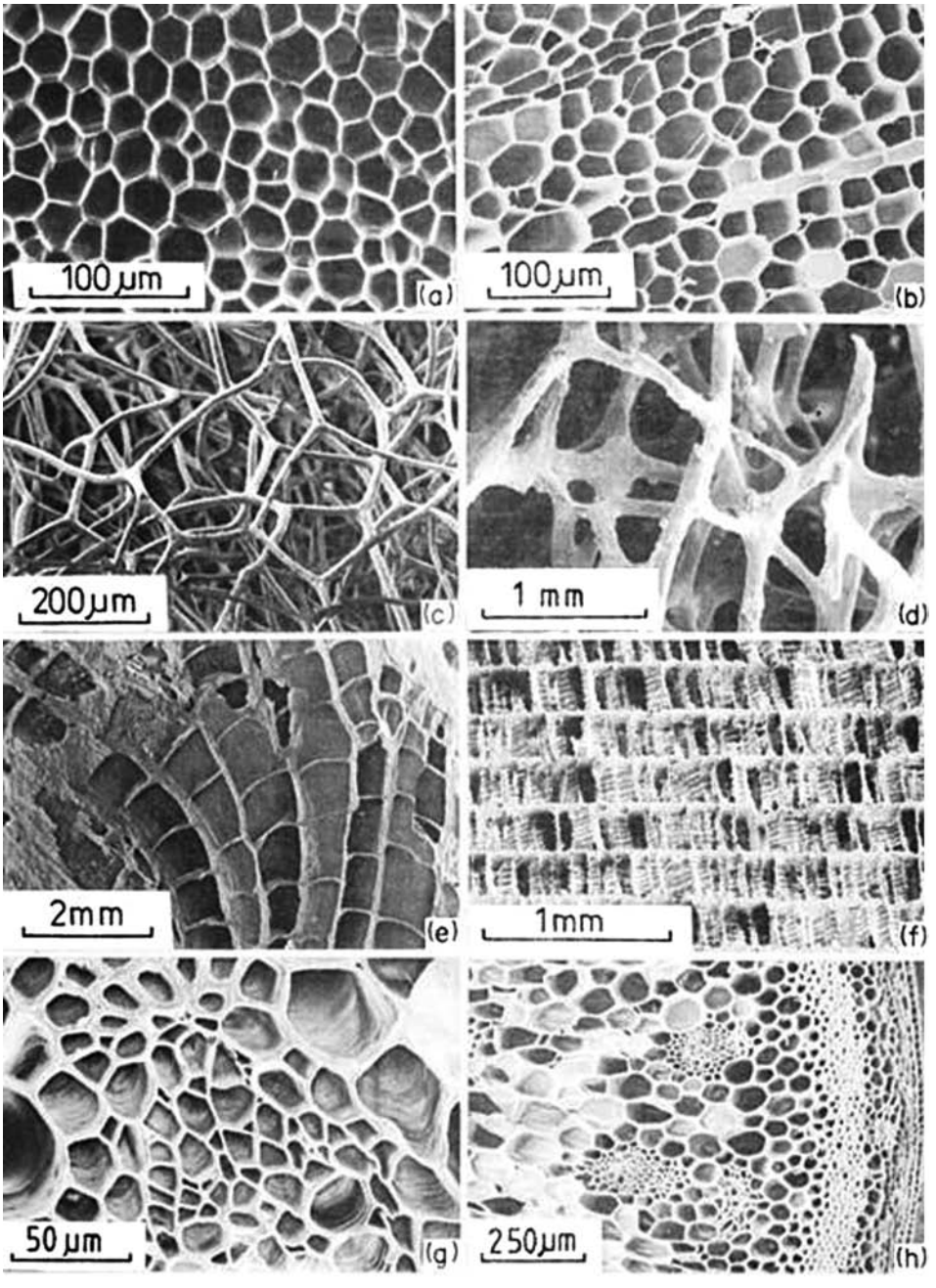

Fig. 12.14 Examples of cellular materials: (a) cork; (b) balsa; (c) sponge; (d) cancellous bone; (e) coral; (f) cuttlefish bone; (g) iris leaf; (h) stalk of plant. (From L. Gibson and M. F. Ashby, *Cellular Materials* (Cambridge, U.K.: Cambridge University Press, 1988).)

(c) a densification region. These are shown in Figure 12.17. The higher the initial density, expressed in Figure 12.17 by ρ^*/ρ_s, the smaller the collapse plateau region. It also occurs at a higher stress.

Following Gibson and Ashby we develop expressions that predict this behavior. They are developed for an open cell geometry that represents well cellular materials with a low relative density. Figure 12.18 represents this open-cell structure. It consists of straight beams with a square cross-section. The model is very simple but captures the

essential physics. There are two characteristic dimensions; the cell size, ℓ, and the beam thickness, t.

In order to characterize the elastic region of an isotropic foam, we can define three elastic constants:

Elastic Region

Three elastic constants are defined for an isotropic foam: E^*, G^*, and ν^*. The density of the cellular material is ρ^*, and that of the solid material is ρ. From Figure 12.18 we can obtain an expression for the density in terms of ℓ and t:

$$\frac{\rho^*}{\rho_s} = C_1 \left(\frac{t}{\ell}\right)^2, \tag{12.5}$$

where C_1 is a proportionality constant. When the cell is subjected to compressive loading, it will deflect as shown in Figure 12.19. The vertical columns push on the horizontal beams and cause them to bend. A force F on each column produces a deflection δ in the beam. The moment of inertia of a beam with a rectangular section (sides of b and h) is:

$$I = \frac{bh^3}{12}. \tag{12.6}$$

The student should consult a mechanics of materials text for the derivation of the above expression.

For a beam with a square cross section with side t:

$$I = \frac{t^4}{12}. \tag{12.7}$$

Beam theory states that the deflection, δ, is given by:

$$\delta = C_2 \frac{F\ell^3}{E_s I}, \tag{12.8}$$

(a)

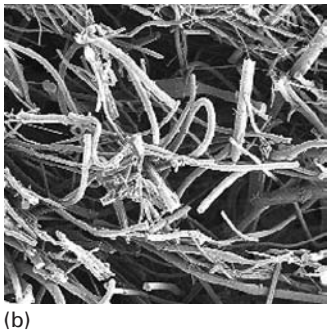

(b)

Fig. 12.15 (a) Cross section of tibia. (From L. Gibson and M. F. Ashby, *Cellular Materials* (Cambridge, UK: Cambridge University Press, 1988).); (b) Glassy SiO_2 foam for space shuttle tiles.

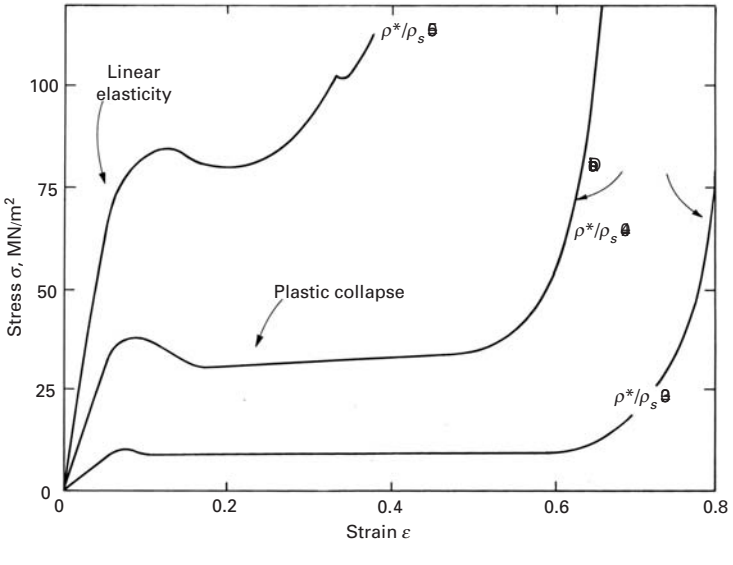

Fig. 12.16 Stress–strain curves for cancellous bone at three different relative densities, ρ^*/ρ_s: 0.3, 0.4, and 0.5. (From L. Gibson and M. F. Ashby, *Cellular Materials* (Cambridge, UK: Cambridge University Press, 1988).)

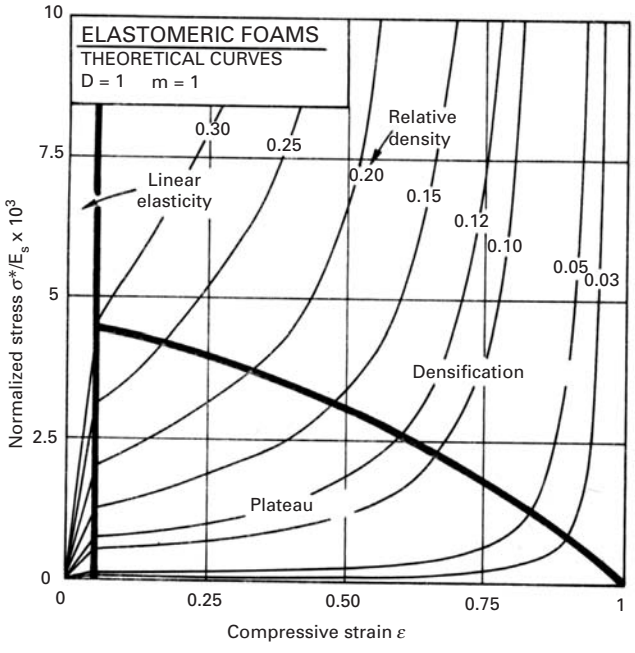

Fig. 12.17 Compressive stress–strain curves of elastomeric foams showing the three characteristic regions: (a) elastic region, (b) collapse plateau, (c) densification region.

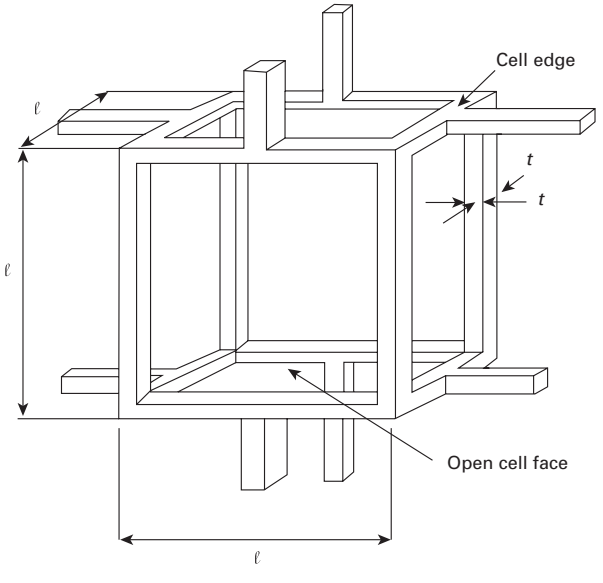

Fig. 12.18 Open-cell structure for cellular materials with low relative density. This is the structure upon which the Gibson–Ashby equations are based.

where C_2 is a constant, E_s is the Young's modulus of the solid. The stress acting on the cell is related to the force, F, by (each force F is shared by two neighboring cells):

$$\sigma = \frac{F}{\ell^2}.$$

The strain, ε, is related to the deflection by:

$$\varepsilon = \frac{2\delta}{\ell}.$$

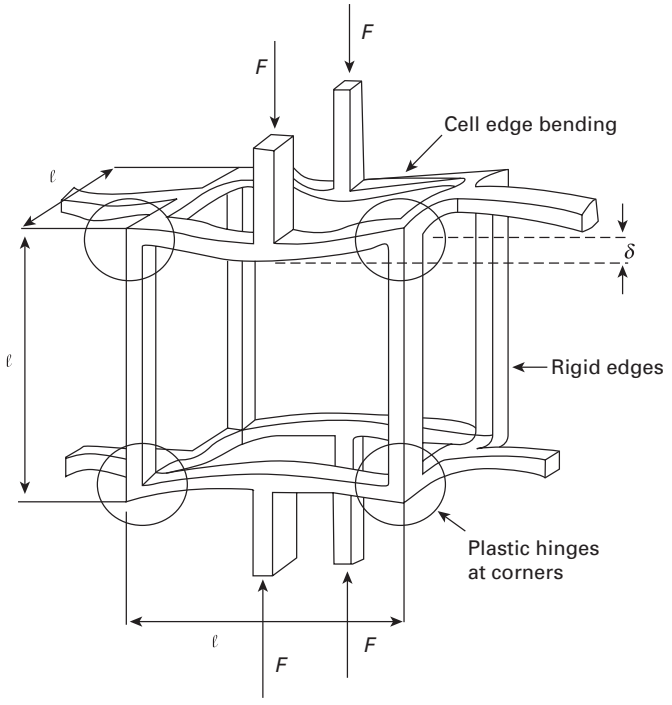

Fig. 12.19 Open-cell configuration under compressive loading. Note the deflection, δ.

Thus, the Young's modulus, E^*, is given by:

$$E^* = \frac{E_s I}{2C_2 \ell^4} = \frac{E_s t^4}{24C_2 \ell^4}.$$

This can be expressed as a function of density (Equation 12.5):

$$\frac{E^*}{E_s} = \frac{C_1}{24C_2} \left(\frac{\rho^*}{\rho_s} \right)^2. \tag{12.9}$$

Experimental measurements indicate that $C_1/24C_2$ should be approximately equal to one. Thus:

$$\frac{E^*}{E_s} \sim \left(\frac{\rho^*}{\rho_s} \right)^2. \tag{12.10}$$

Similarly, an expression for the shear modulus can be obtained:

$$\frac{G}{E_s} = \frac{3}{8} \left(\frac{\rho^*}{\rho_s} \right)^2. \tag{12.11}$$

Plastic Plateau

At a certain level of deformation, elastic behavior gives way to plastic deformation. The Gibson–Ashby equations are based on the formation of plastic hinges at the regions where the beams terminate. One of these plastic hinges is circled in Figure 12.19.

The student should recall the classic equation from mechanics of materials:

$$\sigma = \frac{Mc}{I}, \tag{12.12}$$

where M is the bending moment of a beam, I its moment of inertia, c the distance from neutral axis to external fiber, and σ is the maximum stress. For our case, we have, in the case of plastic deformation ($\sigma = \sigma_y$), the stresses acting on the cross section are uniform and tensile above the neutral axis and uniform and compressive below the neutral axis. Figure 12.19 shows the configuration.

The plastic moment, M_p, about the neutral axis is:

$$M_p = F\,\frac{t}{2}. \tag{12.13}$$

The yield stress is related to F by:

$$\sigma_y = \frac{F}{t\frac{t}{2}}. \tag{12.14}$$

Thus, substituting Equation 12.13 into 12.14:

$$M_p = \frac{1}{4}\sigma_y. \tag{12.15}$$

But, taking the beam with length $\ell/2$ and considering the force $F/2$ applied to each of the two hinges:

$$M_p = \frac{F}{2}\frac{\ell}{2} = \frac{1}{4}F\,\ell. \tag{12.16}$$

The global stress acting on the foam is the force F divided by the area upon which it acts, ℓ^2.

$$\sigma_p^* = \frac{F}{\ell^2} \tag{12.17}$$

From Equations 12.15, 12.16, and 12.17 we get:

$$\frac{\sigma_p^*}{\sigma_y} = \left(\frac{t}{\ell}\right)^3. \tag{12.18}$$

Substituting Equation 12.5 into Equation 12.18:

$$\frac{\sigma_p^*}{\sigma_y} = C_1^{-3/2}\left(\frac{\rho*}{\rho_s}\right)^{3/2}. \tag{12.19}$$

Densification

Densification starts when the plastic plateau comes to an end. This region is characterized by a complex deformation pattern. The stress required for the densification rises rapidly as the open spaces between the collapsed cell structure close up. The analytical treatment for the collapse of pores and voids will not be presented here. There are theories that address this problem. One of the best known, the Carroll–Holt theory, assumes a spherical hole inside a solid sphere. By applying an external pressure it is possible to collapse the internal hole. The smaller the hole, the higher the stress. The Gurson model addresses the same problem. This is discussed in Section 12.4.5.

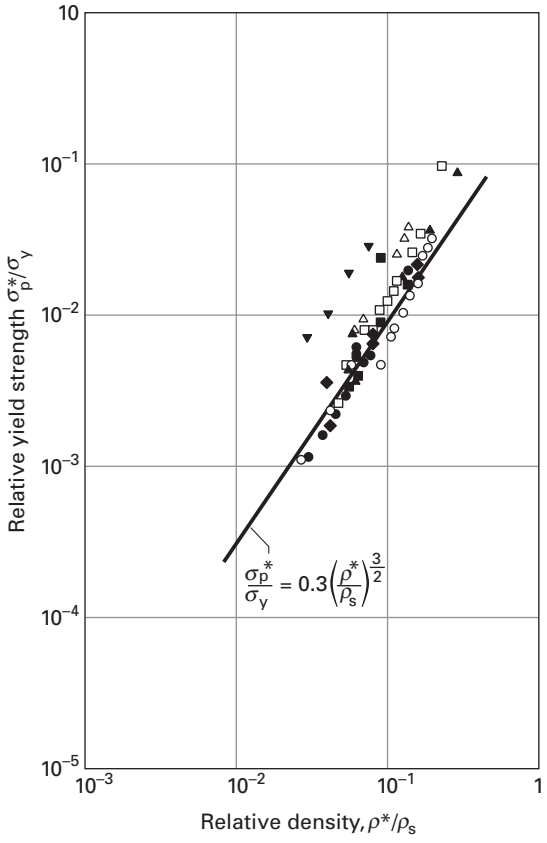

Fig. 12.20 Yield strength of foams as a function of relative density. Experimental results are for a number of materials: polyurethane, aluminum, polystyrene, polymethyl methacrylate, polyvinyl chloride. (Adapted from from L. Gibson and M. F. Ashby, *Cellular Materials*, Cambridge University Press, 1988.)

12.4.3 Comparison of Predictions and Experimental Results

Figure 12.20 shows experimental results for a number of foams undergoing plastic collapse after a stage of elastic deformation. These foams are made from aluminum, aluminum–7% magnesium, polyurethane, polyvinyl chloride, polystyrene, and polymethyl methacrylate. The 3/2 dependence on relative density is clearly seen in the figure. The best fit of Equation 12.19 with experimental results is obtained using a value of 0.3 for $C_1^{-3/2}$. The match between Equation 12.19 and the experimental results for a number of materials is considered excellent.

12.4.4 Syntactic Foam

The micrographs in Figure 12.21 show another type of cellular material called syntactic foam. The word *syntactic* comes from Greek meaning to arrange parts together in a unit. Syntactic foams are made by mixing hollow spheres or microballoons (glass, aluminum, or carbon) in a very small amount of resin. Microspheres, also called microballoons, can range in size from hundreds of nanometers to a few millimeters. Typically, the resin matrix phase in syntactic foam has a large amount of open voids. Strictly speaking, the matrix can be a polymer, metal, or ceramic. The polymer matrix can be epoxy,

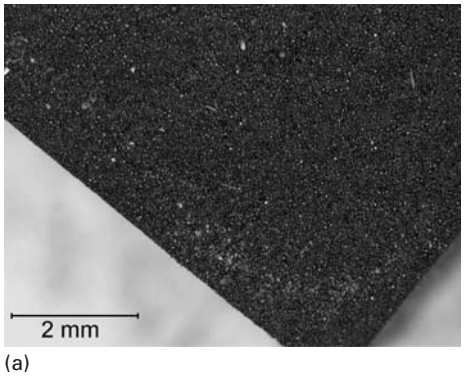

(a)

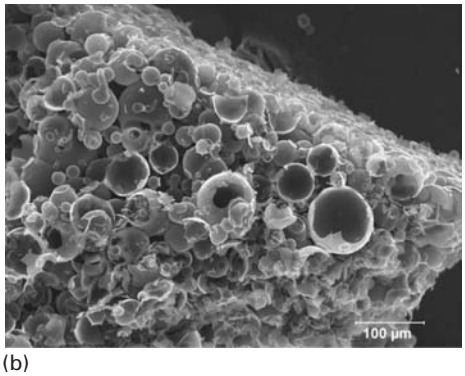

(b)

Fig. 12.21 (a) A low magnification optical picture of syntactic foam made of carbon microballoons dispersed in small amount of resin. (b) A higher magnification scanning electron micrograph of the foam in (a) showing the carbon microballoons. (From K. Carlisle, K. K. Chawla, G. Gouadec, M. Koopman, and G. M. Gladysz, in *Proceedings of the 14th International Conference on Composite Materials*, ICCM-14, San Diego, CA, 2003.)

phenolic, ester cyanate, etc. Figure 12.21(a) shows a carbon microballoon foam at low magnification while Figure 12.21(b) shows a higher magnification picture where the individual carbon microballoons can be seen. Such foams generally have over 90% voids; they show very high specific compressive strength and excellent insulating properties. They find extensive use in deep-sea applications where buoyancy effects become very important.

12.4.5 Plastic Behavior of Porous Materials

Porous materials are gaining in technological importance. Metals and ceramics frequently involve powders that most often have to be pressed. Metallic foams, cellular materials (such as wood) are examples of low-density materials used in structural applications.

We will discuss here briefly the plastic response of powders subjected to compressive loads. Figure 12.22 shows experimentally obtained pressure vs. green density for iron, copper, and nickel powders. The behavior is mostly linear, when the pressure is plotted against $\ln 1(1 - D)$, where D is the relative density of powder, $D = \rho/\rho_s$. At full consolidation, the cellular density is equal to the solid density and $D = 1$. This behavior can be represented by:

$$P = \frac{1}{k}\left[\ln \frac{1}{1-D} + B\right],$$

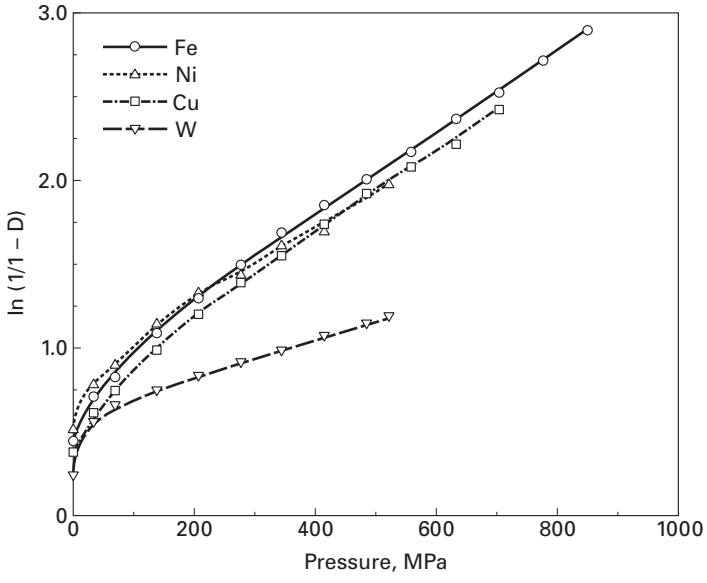

Fig. 12.22 Relationship between pressure and relative green density for several powders. (Adapted from R. M. German, *Powder Metallurgy Science* (Princeton, NJ: Powder Industries Federation), 1984.)

where k and B are experimental parameters. This is an empirical relationship, in which the strength of the powder is not incorporated. Except at low pressures, this equation is obeyed. The constant B is the intercept and k is the slope of the curve. Figure 12.23(a) shows a powder (spherical particles) prior to and during plastic deformation. The particles undergo deformation at the contact points as the external pressure is increased.

The model developed by Fischmeister and Arzt[9] and applied by Helle[10] et al. to sintering is presented here. It represents very well the densification of powders from the initial density (approximately, in many cases, from 0.5 to 0.65 of the theoretical density) to 0.9 of the theoretical density. This is the range in which the individual particles are recognizable. Beyond 0.9 the model proposed by Torre[11] and generalized by Carroll and Holt[12] is more realistic, since it describes the collapse of individual pores (voids) under hydrostatic pressure. Schematic representations of both models are shown in Figure 12.23.

We develop equations for both models. Fischmeister and Arzt assumed that each particle (assumed to be initially spherical) had Z neighbors, and that the number of neighbors increased with density. Again, the relative density $D = \rho/\rho_s$. For the solid, this coordination number is taken as 12. This is equal to the coordination number for atoms in the FCC and HCP structures. Thus:

$$Z = 12D\,.$$

[9] H. Fischmeister and E. Arzt, *Powder Met.*, 26 (1982) 82.
[10] A. S. Helle, K. E. Easterling, and M. F. Ashby, *Acta Met.*, 33 (1985) 2163.
[11] C. Torre, *Huttenmonats. Hochschule Leoben*, 93 (1948) 62.
[12] M. Carroll and A. C. Holt, *J. Appl. Phys.*, 43 (1972) 759.

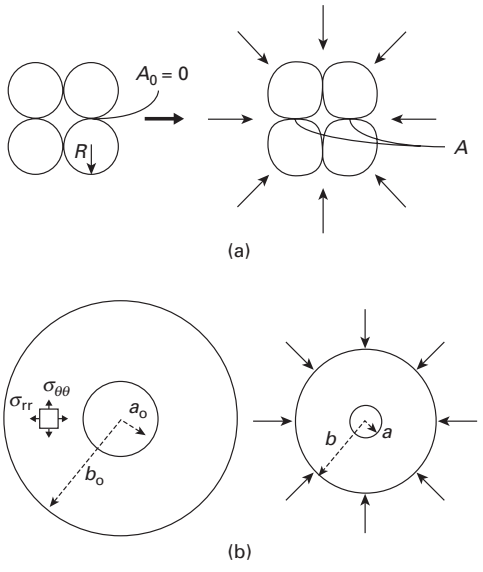

Fig. 12.23 (a) Particle flattening (Fischmeister–Arzt) densification mechanism; (b) Hollow sphere model (Torre and Carroll–Holt).

At D_0 (initial value of D) = 0.64, $Z = 7.7$; for $D = 1$, $Z = 12$. The average area of contact between neighbors, A, is shown in Figure 12.23(a). A increases from $A_0 = 0$ to one-twelfth (1/12) of the particle surface area, $4\pi r^2$, since, as the contact points are flattened, their surface area increases. The maximum area is equal to the total sphere surface divided by the number of neighbors. A simple expression for A is:

$$A = \frac{\pi(D - D_0)}{3(1 - D_0)} R^2.$$

When $D = D_0$, $A = 0$; when $D = 1$, $A = 4\ \pi R^2/12 = (\pi/3)R^2$. R is the radius of particles (Figure 2.23(a)).

The force applied to each contact region, F, is related to the external pressure by:

$$F = \frac{4\pi R^2}{ZD} P.$$

This force, divided by the contact area A, gives the average pressure on the particle at contact region, P_p:

$$P_p = \frac{F}{A} = \frac{4\pi R^2}{AZD} P. \tag{12.20}$$

It is shown in Chapter 3 (hardness testing) that the stress required to make an indentation on a surface is equal to $\approx 3\sigma_y$, where σ_y is the yield stress of the material. Thus:

$$3\sigma_y = \frac{4\pi R^2}{AZD} P; \tag{12.21}$$

and, substituting Equation 12.21 Into Equation 12.20:

$$P = Z\sigma_0 \frac{D(D - D_0)}{4(1 - D_0)}. \tag{12.22}$$

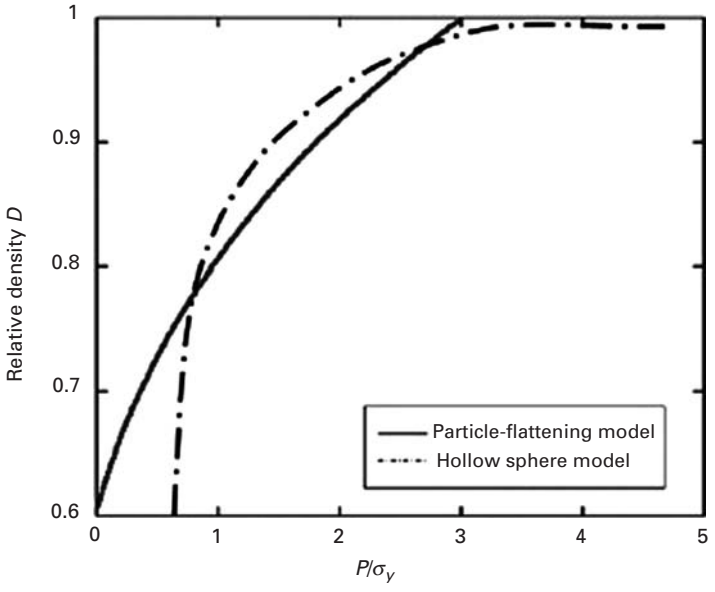

Fig. 12.24 Comparison of particle-flattening and hollow-sphere models for densification under hydrostatic stress.

Equation 14.22 gives a relationship between pressure and the relative density. It is plotted in Figure 12.24 from an initial relative density of 0.6.

The Torre–Carroll–Holt equation is obtained by the application of an analytical treatment to the configuration shown in Figure 12.23(b). The hollow sphere can be used to define a relative density:

$$D = \frac{b^3 - a^3}{b^3},$$

where b is the outer radius and a is the inner radius. In spherical coordinates, the equilibrium equation of stresses acting on an element (shown in Figure 12.23(b)) is:

$$\frac{d\sigma_r}{dr} + \frac{2}{r}(\sigma_r - \sigma_\theta) = 0, \tag{12.23}$$

where σ_r and σ_θ are the radial and circumferential stress components, respectively, and r is the radius. The boundary conditions are:

$$\sigma_r = -P \quad \text{at} \quad r = b;$$
$$\sigma_r = 0 \quad \text{at} \quad r = a.$$

We assume that Tresca's yield criterion holds, i.e., plastic flow occurs when:

$$\sigma_r - \sigma_\theta = \sigma_0,$$

where σ_0 is the flow stress. By integrating Equation 12.23 From a to b, we have:

$$\int_a^b d\sigma_r = -2\sigma_0 \int_a^b \frac{dr}{r},$$
$$-P = -2\sigma_0 \ln\frac{b}{a} = -\frac{2}{3}\sigma_0 \ln\frac{b^3}{a^3}.$$

But

$$\frac{b^3}{a^3} = \frac{1}{1-D}.$$

Hence

$$P = \frac{2}{3}\sigma_0 \ln \frac{1}{1-D}.$$

This equation is plotted in Figure 12.24 and compared with the particle flattening model. The pore collapse model predicts much higher pressures to achieve full densification ($P/\sigma_y > 5$). In this context, it is more realistic for high relative densities ($D > 0.9$). It should be noted that when powders are pressed in cylinders, additional frictional effects at the walls have to be considered. Another complication is that the state of stress deviates from hydrostatic. Thus, a flow criterion has to be incorporated into analysis. In summary, everything becomes increasingly complicated if all effects are incorporated.

Suggested Reading

E. P. George, M. Yamaguchi, K. S. Kumar, and C. T. Liu. *Ann. Rev. Mater. Sci*., 24 (1994) 409.

C. T. Liu, R. W. Cahn, and G. Sauthoff, eds. *High-temperature Ordered Intermetallic Alloys – Physical Metallurgy/Mechanical Behavior*. Boston and Dordrecht: Kluwer, 1992.

A. K. Vasudevan and J. J. Petrovic, eds. *High Temperature Structural Silicides*. Amsterdam: Elsevier, 1992.

J. H. Westbrook and R. L. Fleischer, eds. *Intermetallic Compounds: Principles and Practice*. New York, NY: John Wiley, 1994.

Exercises

12.1 High-temperature applications of intermetallics in air would require oxidation resistance. Comment on some possible sources of such oxidation resistance in intermetallics.

12.2 The formation of a silica film at grain boundaries in $MoSi_2$ can lead to embrittlement. Suggest some means of avoiding this phenomenon.

12.3 Order and disorder transitions are commonly associated with metals, not with polymers. Why?

12.4 An intermetallic compound of Al and Mg has a stable range of 52Mg–48Al to 56Mg–44Al (on a weight basis). What atomic ratios do these compositions correspond to? The atomic weight of Al is 27, and that of Mg is 24.31.

12.5 A metallic laminate consists of FeAl as matrix and Ti as reinforcement. If the the temperature rises from 300 K to 325 K, estimate the expansion of

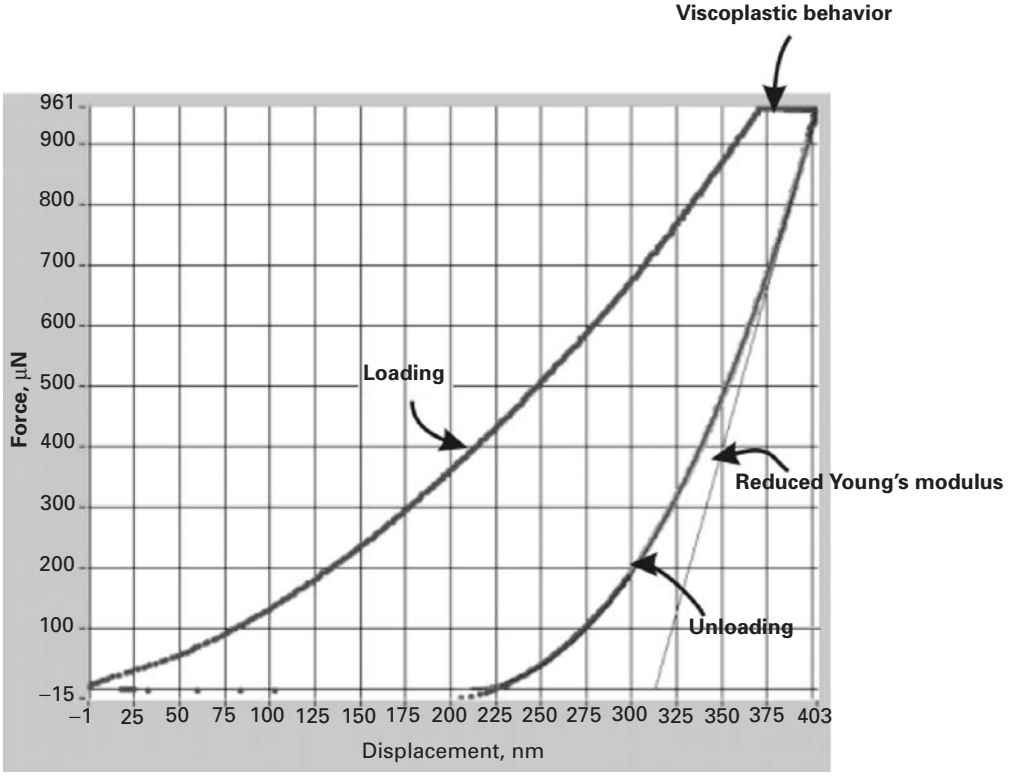

Fig. Ex12.10 Load vs. displacement from nanoindentation on keratin by use of Berkovich tip.

laminated composite. What kinds of problems do you think will be caused by this? Expalin.

12.6 Find the relationship between pressure and relative density of powder from the data shown in Figure 12.22 for Fe, Ni, Cu, and W.

12.7 Plot the strength of the cancellous bone as a function of porosity, assuming that the strength of the fully dense bone is equal to 300 MPa (assume $C1 = 3$).

12.8 Calculate C_1 in the equation:

$$\frac{\rho^*}{\rho_s} = C_1 \left(\frac{t}{\ell}\right)^2.$$

Hint: Assume fully dense material.

12.9 Determine the pressure required to densify a copper powder ($\sigma_0 =$ 100 MPa) to 90% of the theoretical density using:

(a) The Fischmeister and Arzt equation:
(b) The Carroll–Holt–Torre equation.

12.10 From load vs. displacement for keratin shown in Figure Ex12.10, calculate hardness of keratin. Hardness is given by:

$$H = \frac{p}{A},$$

where $P =$ load, $A =$ projected area. Assume Berkovich tip was used.

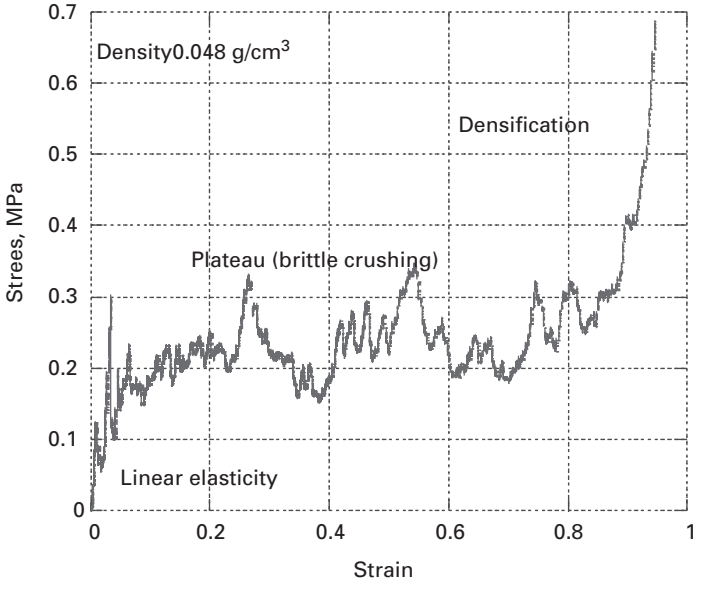

Fig. Ex12.12 Compressive stress–strain curve for foams (toucan beak).

12.11 Figure Ex12.12 shows the compressive stress–strain curve from the foam of a toucan beak. Calculate the densification strain, Young's modulus, shear modulus, and plastic collapse stress of this foam. Assume this foam is open celled.

Densification strain is given by:

$$\varepsilon_d = 1 - 1.4\left(\frac{\rho*}{\rho_s}\right).$$

Density of the foam $\rho^* = 0.04$ g/cm^3;
Density of the cell wall $\rho_s = 0.5$ g/cm^3;
Young's modulus of the cell wall $E_s = 12.7$ GPa;
Yield stress of the cell wall $\sigma_y = 90$ MPa.

Chapter 13

Creep and Superplasticity

13.1 Introduction

The technological developments wrought since the early twentieth century have required materials that resist higher and higher temperatures. Applications of these developments lie mainly in the following areas:

1. Gas turbines (stationary and on aircraft), whose blades operate at temperatures of 800–950 K. The burner and afterburner sections operate at even higher temperatures, viz. 1,300–1,400 K.
2. Nuclear reactors, where pressure vessels and piping operate at 650–750 K. Reactor skirts operate at 850–950 K.
3. Chemical and petrochemical industries.

All of these temperatures are in the range (0.4–0.65) T_m, where T_m is the melting point of the material in kelvin.

The degradation undergone by materials in these extreme conditions can be classified into two groups:

1. *Mechanical degradation*. In spite of initially resisting the applied loads, the material undergoes anelastic deformation; its dimensions change with time.
2. *Chemical degradation*. This is due to the reaction of the material with the chemical environment and to the diffusion of external elements into the materials. Chlorination (which affects the properties of superalloys used in jet turbines) and internal oxidation are examples of chemical degradation.

This chapter deals exclusively with mechanical degradation. The time-dependent deformation of a material is known as *creep*. A great number of high-temperature failures can be attributed either to creep or to a combination of creep and fatigue. Creep is characterized by a slow flow of the material, which behaves as if it were viscous. If a mechanical component of a structure is subjected to a constant tensile load, the decrease in cross-sectional area (due to the increase in length resulting from creep) generates an increase in stress; when the stress

reaches the value at which failure occurs statically (ultimate tensile stress), failure occurs. The temperature regime, in kelvins, for which creep is important in metals and ceramics is $0.5T_m < T < T_m$, the melting of the material. This is the temperature range in which diffusion is a significant factor. A thermally activated process, diffusion shows an exponential dependence on temperature. Below $0.5T_m$, the diffusion coefficient is so low, that any deformation mode exclusively dependent on it can effectively be neglected.

In glasses and polymers, creep becomes important at temperatures above T_g, the glass transition temperature. At $T > T_g$, these materials turn rubbery or leathery, and viscoelastic and viscoplastic effects become important. Section 13.3 presents the various mechanisms responsible for creep. The critical temperature for creep varies from material to material; lead creeps at ambient temperature, whereas in iron creep becomes important above 600 °C. In general, the phenomenon of creep is important at high temperatures. Some nickel-based superalloys can withstand temperatures as high as 1,500 K, and ceramics have temperature capabilities that are considerably higher (up to 2,000 K). Ice, on the other hand, also undergoes creep, which is responsible for the slow flow of glaciers.[1] Even the earth's mantle is subjected to creep, giving it an effective viscosity.

Creep in rocks has been at the center of controversy concerning the nature of geological processes on the planet Venus. The maximum height of mountains on Venus has been calculated on the basis of rock creep, assuming a certain temperature and period of time. (The mountains are subjected to compressive stresses due to their own weight.) This maximum calculated height has been compared with actual topographic observations from the space probe *Galileo*. It happens that dry rock has a creep rate orders of magnitude lower than that of hydrated rock. Weertman has performed calculations for both dry and wet rock, each resulting in a value of 10^9 years for the period of active creep in the mountains. Based on this figure, the maximum height of mountains made of quartzite would be 0.12 km (wet) and 7.6 km (dry). The calculations were done for $T = 750$ K, the surface temperature on Venus. They help to elucidate the mechanisms involved in the formation of the planetary surface.

In spite of the fact that creep has been known since 1834, when Vicat conducted the first experiments assessing the phenomenon, it is only in the twentieth century that systematic investigations have been conducted. The creep test is rather simple and consists of subjecting a specimen to a constant load (or stress) and measuring its length as a function of time, at a constant temperature. Figure 13.1 shows the characteristic curve; the ordinate shows the strain and the abscissa shows time. Three tests are represented in the figure; three constant loads corresponding to three engineering stresses, σ_a, σ_b, and σ_c, were used. The creep curves are usually divided into three stages: I, primary or transient; II, secondary, constant rate, or quasi viscous;

[1] J. Weertman, *Ann. Rev. Earth Plan. Sci.*, 11 (1983) 215.

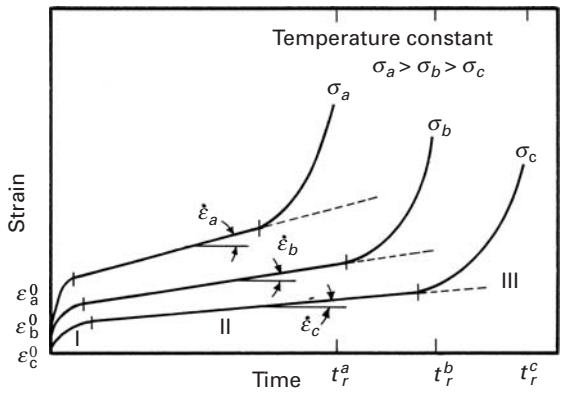

Fig. 13.1 Creep strain vs. time at different constant stress levels and temperature.

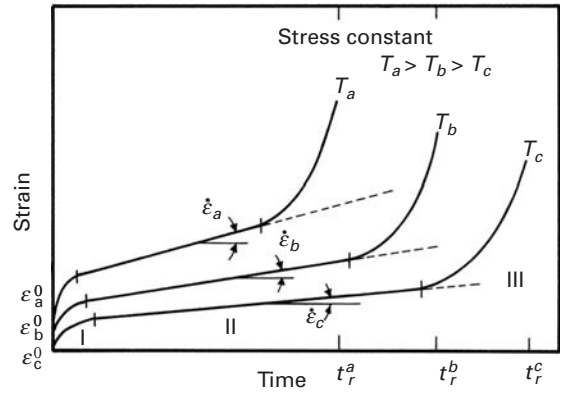

Fig. 13.2 Creep strain vs. time at a constant engineering stress and different temperatures.

and III, tertiary. This division into stages was made by Andrade, one of the pioneers in the study of creep. Stage II, in which the creep rate $\dot{\varepsilon}$ is constant, is the most important. It can be seen that $\dot{\varepsilon}_a > \dot{\varepsilon}_b > \dot{\varepsilon}_c$ as a consequence of the relationship $\sigma_a > \sigma_b > \sigma_c$. This creep rate is also known as the *minimum creep rate*, because it corresponds to the inflection point of the curve. (See Figure 13.1.) In stage III there is an acceleration in the creep rate, leading to eventual rupture of the specimen.

In Figure 13.1, the rupture times t_r^a, t_r^b, and t_r^c increase with decreasing stress. The strains ε^0 are called *instantaneous* strains and correspond to the strains at the instant of loading. In Figure 13.2, the engineering stress was kept constant and the temperature was varied. Since the tests are conducted in tension, the stress rises as the length of the specimen increases, because of the reduction in area. The dashed lines in Figures 13.1 and 13.2 represent the constant stress curves. Initially they are identical, because ε_e, the elastic strain, $= 0$. As the specimen increases in length, the stress increases and so does the creep rate, at a constant load. The failure times under constant stress and constant load can be drastically different. The curves shown in Figure 13.2 have been expressed mathematically as

$$\varepsilon_t = \varepsilon^0 + \varepsilon[1 - \exp(-mt)] + \dot{\varepsilon}_s t \tag{13.1}$$

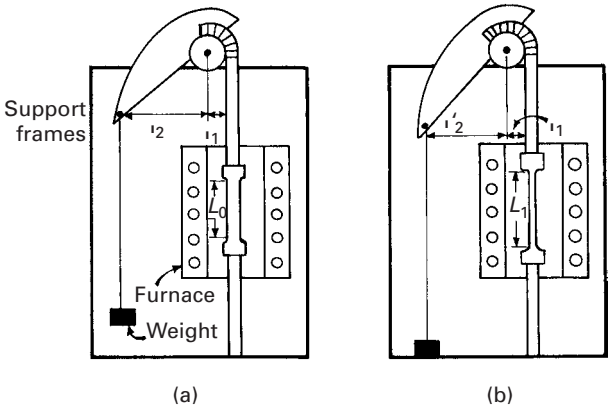

Fig. 13.3 Creep machine with variable lever arms to ensure constant stress on specimen; note that l_2 decreases as the length of the specimen increases. (a) Initial position. (b) Length of specimen has increased from L_0 to L_1.

where ε^0 is the instantaneous strain (the strain at the instant of application of load), $\dot{\varepsilon}_s t$ is a linear function of time, depicting stage II, and the term $\varepsilon[1 - \exp(-mt)]$ represents stage I in which m is the exponential time parameter and ε is the limiting transient creep strain (strain at end of that stage minus ε^0).

From a fundamental point of view, there are significant differences between the constant-load and constant-stress creep tests. Andrade realized this important difference and built a constant true-stress creep machine that used a weight which dropped gradually into a fluid as the specimen extended.[2] Thus, by Archimedes' principle, the force exerted by the weight decreased with displacement. The shape of the weight was such that a constant stress on the specimen was ensured. For this type of machine, the load should decrease with an increase in length in such a way that the true stress remains constant.

Another important difference between the two tests is that the onset of stage III is greatly retarded at constant stress. The dashed lines in Figure 13.2 show the trajectory that a constant true-stress test would follow.

From an engineering point of view, the creep test at constant load is more important than the one at constant stress because it is the load, not the stress, that is maintained constant in engineering applications. On the other hand, fundamental studies should be conducted at constant stress, with the objective of elucidating the underlying mechanisms. The reason for this is that the study of the evolution of the substructure of an alloy under increasing stress would be excessively complex.

The essential components and principles of operation of a constant-stress creep-testing machine are shown in Figure 13.3. This system contains a variable lever arm, which is a curved line that acts as a cam in such a manner that the force acting on the specimen is a function of its length. Two positions are shown in the figure. If

[2] E. N. da L. Andrade, *Proc. Roy Soc. (London)*, A84 (1911) 1.

the initial and current cross-sections of the specimen are A_0 and A_1, respectively, then

$$\sigma_0 A_0 \ell_1 = P \ell_2 \tag{13.2}$$

and

$$\sigma_1 A_1 \ell_1 = P \ell_2'$$

where P is the load and ℓ_1, ℓ_2, and ℓ_2' are lever arms defined in the figure. At constant stress, $\sigma_0 = \sigma_1$; since the volume of the specimen is constant (for stages I and II of creep),

$$A_0 L_0 = A_1 L_1,$$

where L_0 and L_1 are the initial and current lengths of the specimen, respectively. Thus,

$$\frac{L_1}{L_0} = \frac{\ell_2}{\ell_2'}. \tag{13.3}$$

The exact shape of the lever arm can be established in such a manner that Equation 13.3 is obeyed. The astute student will certainly be able to obtain the mathematical description for this curved surface.

It is important to recognize that, even at a constant stress, the creep curve will deviate from linearity at a certain point. This can be due to several causes, the most important being the formation of internal flaws such as cavities (known as creep cavitation) and necking of the specimen. The minimum creep rate, or slope of stage II of creep, is a very important parameter. This stage, also known as steady-state creep, is usually represented by the equation

$$\dot{\varepsilon}_s = \frac{AGb}{kT} D_0 \exp(-Q_c/RT) \left(\frac{b}{d}\right)^p \left(\frac{\sigma}{G}\right)^n, \tag{13.4}$$

where A is a dimensionless constant, D_0 is a frequency factor, G is the shear modulus, b is the Burgers vector, k is Boltzmann's constant, T is the absolute temperature, σ is the applied stress, d is the grain size, p is the inverse grain-size exponent, n is the stress exponent, Q_c is the appropriate activation energy, and R is the gas constant. This equation is known as the Mukherjee–Bird–Dorn equation.[3] It will be shown in Section 13.3 that the activation energy for diffusion is often equal to the activation energy for creep ($Q_c = Q_D$). The diffusion coefficient is

$$D = D_0 \exp\left(-\frac{Q_D}{RT}\right)$$

and

$$\dot{\varepsilon}_s = \frac{AGbD}{kT} \left(\frac{b}{d}\right)^p \left(\frac{\sigma}{G}\right)^n. \tag{13.5}$$

Essentially, Equations 13.4 and 13.5 express the steady-state creep rate as a function of the applied stress, temperature, and grain size. In

[3] A. K. Mukherjee, J. E. Bird, and J. E. Dorn, *Trans. ASM*, 62 (1964) 155.

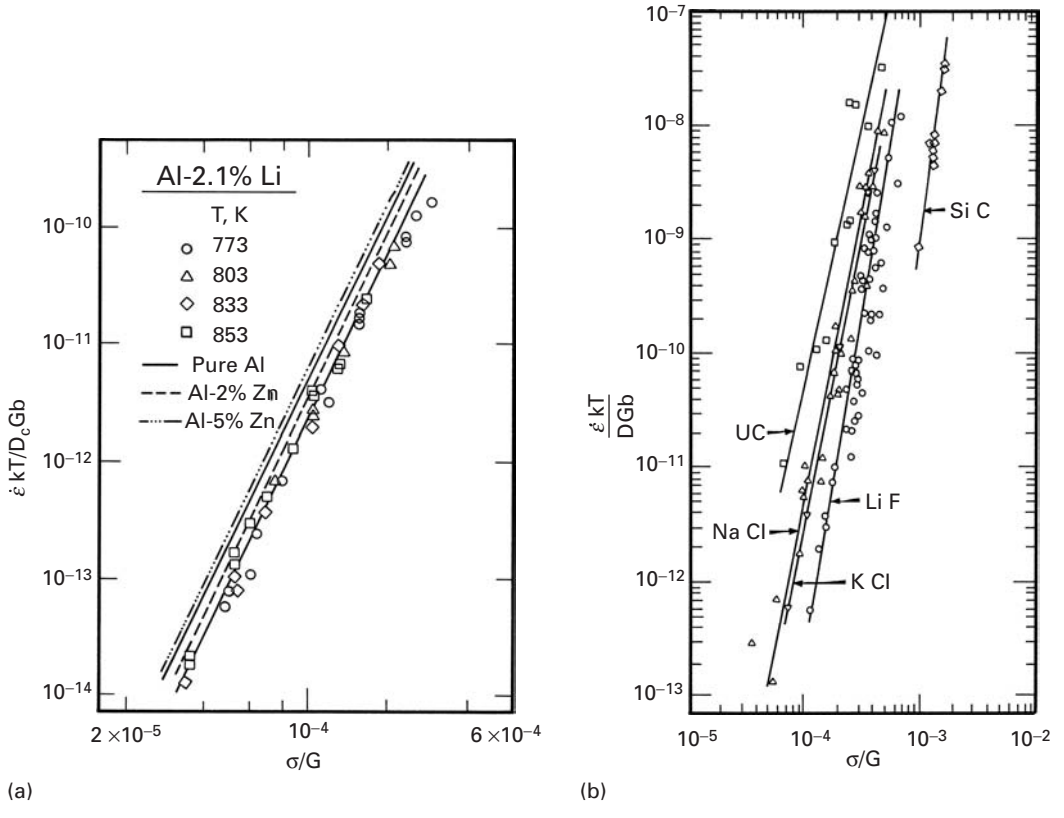

Fig. 13.4 Normalized creep rate vs. normalized stress (according to Mukherjee–Bird–Dorn equation) for (a) aluminum, Al–Zn, and Al–Li solid solutions. (Adapted from K.-T. Park, E. J. Lavernia, and F. A. Mohamed, *Acta Met. Mat.*, 38 (1990) 1837.) (b) Various ceramics. (From A. H. Chokshi and T. G. Langdon, *Mater. Sci. Techn.*, 7 (1991) 577.)

this chapter we will use d to designate the grain size, to differentiate it from D, the diffusion coefficient. Equation 13.4 is also a fundamental equation in superplasticity. Figure 13.4 illustrates the application of the Mukherjee–Bird–Dorn equation to metals (aluminum and aluminum alloys) and ceramics. This is usually done by plotting a normalized strain rate ($\dot{\varepsilon}kT/DGb$) vs. a normalized stress (σ/G). The agreement with the equation is excellent, and the slope of these plots enables the exponent n to be determined. For both cases, it is approximately equal to 5. The exponent, in its turn, can provide information on the fundamental mechanism of creep. This will be discussed at length in Sections 13.3–13.7. In ceramics, n is observed to be in two ranges: 1–3 or 5–7. The significance of these results will be discussed later.

Equation 13.4 is important because it enables strain to be predicted in a specimen under creep conditions, once the various parameters that describe its creep response are established. The creep rate is dependent on stress, temperature, grain size, and other material parameters.

Another test, commonly used in place of the creep test, is the *stress-rupture* (or *creep-rupture*) test. This consists of an accelerated creep test that leads to rupture. It is usually carried out at a constant load, for the sake of simplicity. The important parameter obtained from the

test is the time to rupture, whereas in the regular creep test, the minimum creep rate is the experimental parameter sought.

The sections that follow deal with several important aspects of creep. Section 13.2 describes the extrapolation methods used to obtain the response to creep at very large times after conducting more accelerated tests. Theories of creep are described in Sections 13.3–13.7. The very helpful deformation-mechanism maps called Weertman–Ashby maps are presented in Section 13.8. And some important heat-resisting alloys are described in Section 13.9. Section 13.10 treats polymers and Section 13.11 discusses superplasticity.

13.2 Correlation and Extrapolation Methods

The central theme of materials science and engineering is the structure–property–performance triangle. In creep, the correlation between properties and performance is very critical, because in certain applications we want to know the performance during an extended period (20 or more years), while the properties (secondary creep rate or stress-rupture life) are known for a shorter period. In general, industrial equipment operating at a high temperature is designed to have a certain lifetime. For jet turbines, 10,000 hours (about 1 year) is a reasonable value. For stationary turbines, the weight of the components is not so critical, and a life of 100,000 hours (about 11 years) is the goal. For nuclear reactions, for obvious reasons, we use the criterion of 350,000 hours (40 years). A great number of advanced alloys are used in these projects, and the engineer does not have on hand the results of lengthy tests. Hence, several extrapolation methods have been developed that seek to predict the performance of alloys based on tests conducted over a shorter period. The number of parametric methods developed exceeds 30; the three most common are the Larson–Miller, Manson–Haferd, and Sherby–Dorn methods.

In 1952, Larson and Miller proposed a method that correlates the temperature T (in kelvins) with the time to failure t_r, at a *constant* engineering stress σ.[4] The Larson–Miller equation has the form

$$\boxed{T(\log t_r + C) = m,} \tag{13.6}$$

where C is a constant that depends on the alloy, m is a parameter that depends on stress, and rupture time. Hence, if C is known for a particular alloy, one can find m in a single test. From this result, one can then find the rupture times at any temperature, *as long as the same engineering stress is applied*. Thus, the following procedure is adopted. If we want to know the rupture time at a certain stress level σ_a and temperature T_a, we conduct the test at $T_b > T_a$ and stress level σ_a. Substituting these values into Equation 13.6, we find m. The latter

[4] F. R. Larson and J. Miller, *Trans. ASME*, 74 (1952) 765.

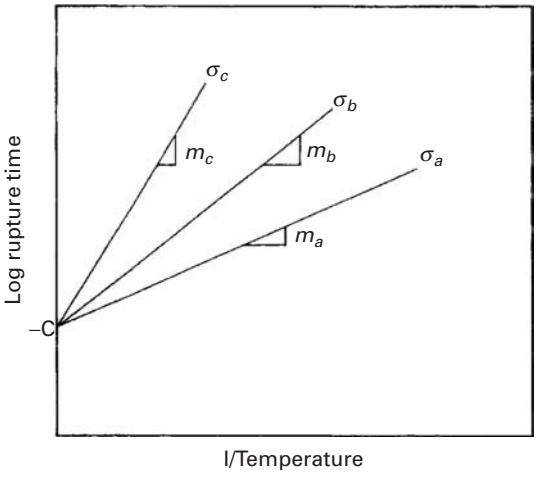

Fig. 13.5 Relationship between time to rupture and temperature at three levels of engineering stress, σ_a, σ_b, and σ_c, using Larson–Miller equation ($\sigma_a > \sigma_b > \sigma_c$).

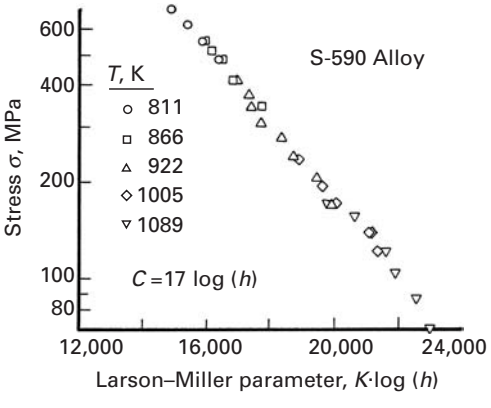

Fig. 13.6 Master plot for Larson–Miller parameter for S-590 alloy (an Fe-based alloy) ($C = 17$). (From R. M. Goldhoff, *Mater. Design Eng.*, 49 (1959) 93.)

test has a short duration, because the time to rupture decreases with temperature at a constant stress. Figure 13.5 shows schematically the family of lines for different levels of stress. This figure is the graphic representation of Equation 13.6. It can be seen that C does not depend on the stress; it is the intersection of the various lines. On the other hand, each line has a different slope m, which is dependent on the stress.

The value of C is unaltered by the units, as long as the unit of time is hours. However, m is dependent on units. In the older literature, use is made of English units (Rankine), and a conversion has to be made. At a certain stress level, we need only two data points to establish C and m. Since the value of C is constant for an alloy, we can build a "master plot" that represents the creep rupture response of an alloy over a range of temperatures and stresses. As an example, Figure 13.6 shows the master plot for the ferrous alloy S-590. The data were obtained between 811 and 1,089 K and fall on one single line, due to the correct choice of C: 17 log (hours). From this plot, we can obtain the time to rupture at any temperature and stress.

Soon after Larson and Miller proposed their parameter, Manson and Haferd presented the results of their experiments, which disagreed with Equation 13.6 on the following points:[5]

1. The family of lines intersects not on the ordinate axis ($1/T = 0$), but at a specific point (t_a, T_a).
2. A better linearization is obtained if the results are plotted as log t_r versus T instead of log t_r versus $1/T$.

This led Manson and Haferd to propose the following equation:

$$\boxed{\frac{\log t_r - \log t_a}{T - T_a} = m.} \tag{13.7}$$

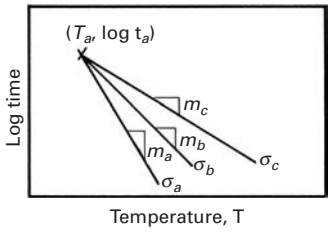

Fig. 13.7 Relationship between time rupture and temperature at three levels of stress, σ_a, σ_b, and σ_c, using Manson–Haferd parameter ($\sigma_a > \sigma_b > \sigma_c$).

Equation 13.7 is represented graphically in Figure 13.7. We use the same extrapolation procedure as that of Larson and Miller to obtain rupture times at different times and temperatures. T_a, t_r, and m are parameters to be established for a given material. T_a and t_r are constant, and m depends on the stress. In Figure 13.7, three stresses are shown, leading to three lines with different slopes $m_c > m_b > m_a$. The times t_r and t_a are usually expressed in hours. As with the Larson–Miller parameter, the early literature (up to 1980) usually reports value for the Manson–Haferd parameter in the English system, whereas the more recent literature uses SI units.

Another method that has found considerable success is the Orr–Sherby–Dorn method,[6] based on fundamental studies conducted by Sherby, Dorn, and coworkers with the objective of understanding creep better. The method is based on the fundamental result found by them these researchers, viz.,

$$\ln t_r - \frac{Q}{kT} = m, \tag{13.8}$$

where Q is the activation energy of diffusion (or creep), m is the Sherby–Dorn parameter, and t_r is the time to rupture. Figure 13.8 shows the graphical representation of this parameter. It differs from the Larson–Miller parameter in that the isostress lines are parallel. Equation 13.8 has a certain fundamental justification. Monkman and Grant[7] and others observed that, for a great number of alloys, the minimum creep rate $\dot{\varepsilon}_s$ was inversely proportional to the rupture time t_r, or

$$\dot{\varepsilon}_s t_r = k'. \tag{13.9}$$

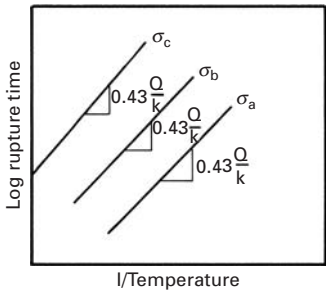

Fig. 13.8 Relationship between time to rupture and temperature at three levels of stress, $\sigma_a > \sigma_b > \sigma_c$, using Sherby–Dorn parameter.

Applying Equation 13.4, which states that creep is a thermally activated mechanism and that the minimum creep rate increases exponentially with temperature at the same value of stress, and combining

[5] S. S. Manson and A. M. Haferd, *NACA TN*, 2890, March 1958.
[6] R. L. Orr, O. D. Sherby, and J. E. Dorn, *Trans. ASM*, 46 (1954) 113.
[7] F. C. Monkman and N. J. Grant, *Proc. ASTM*, 56 (1956) 593.

Table 13.1 Some Values of Constants for Time–Temperature Parameters[a]

Material	Sherby–Dorn Q, kJ/mol	Larson–Miller C	Manson–Haferd $T_{a'}$, K	Manson–Haferd log t_a
Various steels and stainless steels	≈400	≈20	–	–
Pure aluminum and dilute alloys	≈150	–	–	–
S-590 alloy (Fe based)	350	17	172	20
A-286 stainless steel	380	20	367	16
Nimonic 81A (Ni- based)	380	18	311	16
1% Cr–1% Mo–0.25%V steel	460	22	311	18

[a] Adapted from N. E. Dowling, *Mechanical Behavior of Materials* (Englewood Cliffs, NJ: Prentice Hall, 1993), p. 699, Table 15.1.

the preexponential terms, we have

$$\dot{\varepsilon}_s = A' \exp(-Q_c/kT). \tag{13.10}$$

Substituting Equation 13.9 into Equation 13.10 yields

$$t_r = \frac{k'}{A'} \exp(Q_c/kT).$$

or, taking the logarithm of both sides,

$$\ln t_r - \ln \frac{k'}{A'} = \frac{Q_c}{kT}.$$

Converting to logarithms to the base 10 and setting $\log k'/A' = m$, we get

$$2.3\left(\log t_r - \log \frac{k'}{A'}\right) = \frac{Q_c}{kT}$$

$$\boxed{\log t_r - m = 0.43\frac{Q_c}{kT}.}$$

The slope of the lines in Figure 13.8 is $0.43Q_c/k$, which is equal to $0.43Q_D/k$. If we know the activation energy for diffusion and one point on the line, we have all the other points. The activation energy for self-diffusion can be obtained from the diffusion coefficients at two different temperatures. A thermally activated process, the diffusion obeys the equation

$$D = D_0 \exp(-Q_D/kT), \tag{13.11}$$

where D is the diffusion coefficient at T.

In this and the previous section, Q, the activation energy, is expressed as energy (joules per atom). If Q is expressed per mole, or atom gram, then R (the gas constant) should be used instead of k (Boltzmann's constant). The value of R is 8.314 J/(mol K). In Figure 13.8, the slope would be $(0.43Q)/8.314$, or $Q/19.3$ (when Q is expressed in J/mol).

Table 13.1 presents estimated values for the parameters of the three equations for a number of engineering alloys.

Example 13.1

The alloy INCONEL 718 was diligently tested by graduate student M. A. Meyers at 820 MPa and a temperature of 650 °C. Three conditions of the alloy were tested: undeformed, cold-rolled, and shock-hardened (by explosives). After days of patient data collecting (this was in the 1970s prior to automated data recording), he obtained the curves shown in Figure E13.1. Using the Larsen–Miller parameter, determine the times to rupture if this alloy will be used at (a) 550 °C and the same stress and (b) 650 °C and 600 MPa. Take $C = 18$.

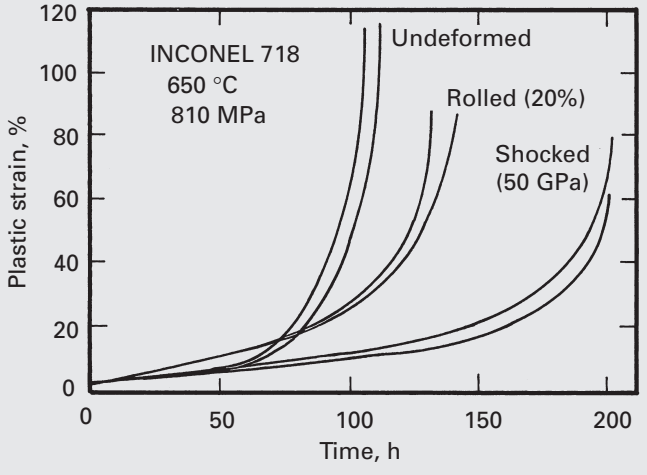

Fig. E13.1

Solution:

(a) We use the equation

$$T(\log t_r + C) = m$$

with $t_r \approx 110$ hours for the undeformed condition, $t_r \approx 130$ hours for the rolled condition, and $t_r \approx 200$ hours for the shocked condition. We have

$$T = 650 + 273 = 923 \text{ K}$$
$$923 (\log 110 + 18) = 17{,}575,$$
$$923 (\log 130 + 18) = 17{,}642,$$
$$923 (\log 200 + 18) = 17{,}814.$$

At 550 °C, $T = 823$ K, and $t_r = 22.6 \times 10^4$ hours for the undeformed condition, $t_r = 27.3 \times 10^3$ hours for the rolled condition, and $t_r = 44.2 \times 10^3$ hours for the shocked condition.

(b) No result can be obtained in this case because the stress has to be constant, for the application of the Larsen–Miller equation to two conditions.

Example 13.2

Calculate the predicted time to rupture for the undeformed INCONEL 718 superalloy, using the Sherby–Dorn correlation method.

Solution: From Table 13.1, (for the Ni-based alloy Nimonic, fairly similar to INCONEL 718):

$$Q \approx 380 \text{ kJ/mol}.$$

We obtain the Sherby–Dorn parameter m:

$$\log t_r - m = 0.43\frac{Q_c}{kT},$$

$$m = \log t_r - 0.43\frac{Q_c}{kT}.$$

Since the activation energy is expressed in J per mol, we have to use R (=8.314 J/mol K) instead of k (Boltzmann's constant). Thus,

$$m = \log 110 - 0.43 \times \frac{380 \times 10^3}{8.314 \times 923}$$
$$= 2.04 - 21.29 = -19.25.$$

Applying Sherby–Dorn's equation to 550°C (823 K) yields

$$\log t_r = m + 0.43\frac{Q_c}{kT} = -19.25 + \frac{0.43 \times 380 \times 10^3}{8.314 \times 823},$$

or

$$t_r = 42.7 \times 10^3 \text{ hours}.$$

Example 13.3

Calculate the time to rupture at 650 °C and 100 MPa stress for a 1% Cr–1% Mo–0.25% V steel, according to the Larson–Miller, Sherby–Dorn, and Manson–Haferd methods, if this alloy underwent rupture in 20 hours when tested in tension at the same stress level at a temperature of 750 °C.

Solution: The Larson–Miller equation is $T(\log t_r + C) = m$. From Table 13.1, $C = 22$. Thus, at 750 °C, $T = 750 + 273 = 1{,}023$ K and $t_r = 20$ hours. Therefore,

$$m = 1023 \times (\log 20 + 22) \approx 2.4 \times 10^4$$

At 650 °C, $T = 650 + 273 = 923$ K, and we have

$$923(\log t_r + 22) = 2.4 \times 10^4,$$

so that

$$\log t_r = \frac{2.4 \times 10^4}{923} - 22$$

and

$$t_r = \underline{6.7 \times 10^3 \text{ hours}}.$$

The Sherby–Dorn equation is $\log t_r - Q/(kT) = m$. From Table 13.1, $Q = 460$ kJ/mol. Because Q here involves moles, we must use R instead of k. At 750 °C, $T = 1{,}023$ K and $t_r = 20$ hours. Thus,

$$m = \log 20 - \frac{460 \times 10^3}{8.314 \times 1023}.$$

At 650 °C, $T = 923$ K, and we obtain

$$\log t_r = m + 0.43\frac{Q}{kT},$$

so that

$$t_r = \underline{6 \times 10^3 \text{ hours.}}$$

The Manson–Haferd equation is $(\log t_r - \log t_a)/(T - T_a) = m$. From Table 13.1, $T_a = 311$ K, so that $\log t_a = 18$. At 750 °C, $T = 1{,}023$ K, and it follows that $t_r = 20$ hours. Therefore,

$$m = \frac{\log 20 - 18}{1{,}023 - 311} = -0.023.$$

At 650 °C, $T = 923$ K, and we have

$$\frac{\log t_r - \log t_a}{T - T_a} = m,$$

$$\frac{\log t_r - 18}{923 - 311} = -0.023,$$

$$\log t_r = 3.924,$$

$$t_r = \underline{8.4 \times 10^3 \text{ hours}}.$$

This answer is very sensitive to m. For $m = -0.02345$, we get $t_r = 4.4 \times 10^3$ hours.

13.3 Fundamental Mechanisms Responsible for Creep

The history of progress in our understanding of creep can be divided into two periods: before and after 1954. In that year, Orr et al. introduced the concept that the activation energy for creep and diffusion are the same for an appreciable number of metals (more than 25).[8] Figure 13.9 shows this graphically. The activation energy for diffusion is connected to the diffusion coefficient by Equation 13.11. Note that several mechanisms can be responsible for creep; the rate-controlling mechanism depends both on the stress level and on the temperature, as will be seen in Sections 13.4–13.7. For temperatures below $0.5T_m$, half the melting point of the material, in kelvins, the activation

[8] R. L. Orr, O. D. Sherby, and J. E. Dorn, *op. cit.*, 113.

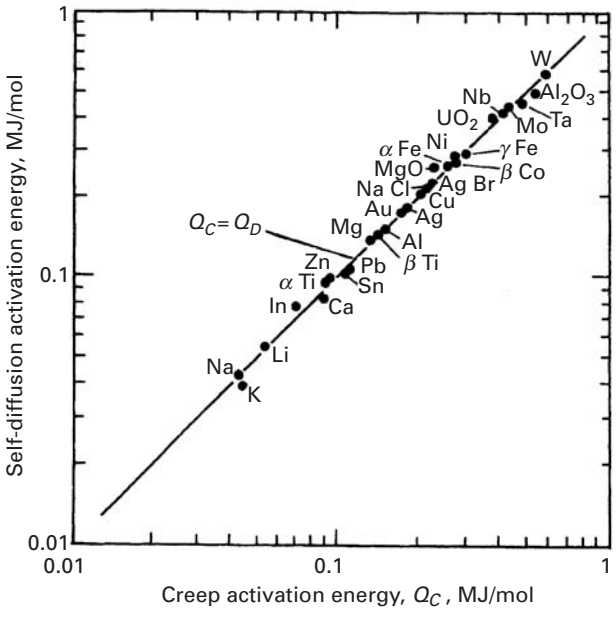

Fig. 13.9 Activation energies for creep (stage II) and self-diffusion for a number of metals. (Adapted with permission from O. D. Sherby and A. K. Miller, *J. Eng. Mater. Technol.*, 101 (1979) 387.)

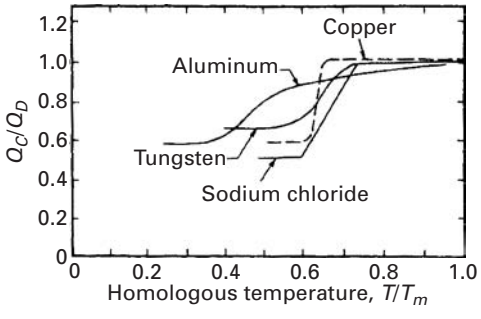

Fig. 13.10 Ratio between activation energy for secondary creep and activation energy for bulk diffusion as a function of temperature. (Adapted with permission from O. D. Sherby and A. K. Miller, *J. Eng. Mater. Technol.*, 101 (1979) 387.)

energy for creep tends to be lower than that for self-diffusion, because diffusion takes place preferentially along dislocations (pipe diffusion), instead of in bulk. Figure 13.10 shows the variation in Q_C/Q_D for some metals and ceramics. The activation energy for diffusion through dislocations is considerably lower than that for bulk diffusion.

For the temperature range $T > 0.5\,T_m$, the mechanisms responsible for creep can be conveniently described as a function of the applied stress. The creep mechanisms can be divided into two major groups: boundary mechanisms, in which grain boundaries and, therefore, grain size, play a major role; and lattice mechanisms, which occur independently of grain boundaries. In Equation 13.4, the exponent $p = 0$ for lattice mechanisms, and $p \geq 1$ for boundary mechanisms.

13.4 Diffusion Creep ($\sigma/G < 10^{-4}$)

Diffusion creep tends to occur for $\sigma/G \leq 10^{-4}$. (This value depends, to a certain extent, on the metal.) Two mechanisms are considered

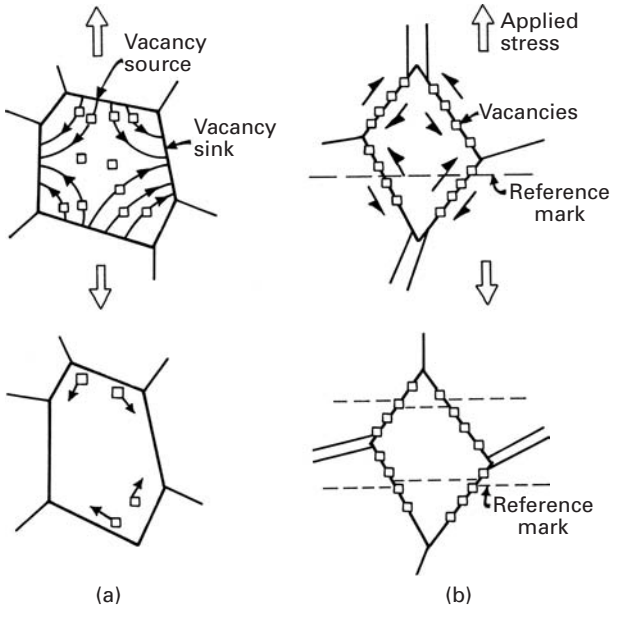

Fig. 13.11 Flow of vacancies according to (a) Nabarro–Herring and (b) Coble mechanisms, resulting in an increase in the length of the specimen.

important in the region of diffusion creep. Nabarro and Herring proposed the mechanism shown schematically in Figure 13.11(a).[9] It involves the flux of vacancies inside the grain. The vacancies move in such a way as to produce an increase in length of the grain along the direction of applied (tensile) stress. Hence, the vacancies move from the top and bottom region in the figure to the lateral regions of the grain. The boundaries perpendicular (or close to perpendicular) to the loading direction are distended and are sources of vacancies. The boundaries close to parallel to the loading direction act as sinks.

Nabarro and Herring developed a mathematical expression connecting the vacancy flux to the strain rate. They started by supposing that the "source" boundaries had a concentration of vacancies equal to $C_0 + \Delta C$ and the sink boundaries a concentration C_0. They assumed that

$$\Delta C = \frac{C_0 \sigma}{kT},$$

where σ was the applied stress and C_0 the equilibrium vacancy concentration. The flux of vacancies is therefore given by

$$J = k' D_\ell \left(\frac{\Delta C}{x} \right) = k'' D_\ell \left(\frac{\Delta C}{d} \right),$$

where x is the diffusion distance, which is a direct function of the grain size (approximately equal to $d/2$), D_ℓ, is the lattice diffusion coefficient, d is the grain diameter, and k' and k'' are proportionality constants ($k'' = 2k'$). The strain rate is related to the increase in grain

[9] F. R. Nabarro, *Report of a Conference on Strength of Solids, Physical Society*, London, 1948, p. 75; and C. Herring, *J. Appl. Phys.*, 21 (1950), 437.

size d in the direction of the applied stress:

$$\dot{\varepsilon} = \frac{1}{d}\frac{dd}{dt}.$$

The change in grain length, dd/dt, can be obtained from the flux of vacancies, each having a volume Ω:

$$\frac{dd}{dt} = J\Omega.$$

Thus, the following equation can be obtained for the creep rate:

$$\dot{\varepsilon}_{\mathrm{NH}} = k''\frac{\Omega D_\ell C_0 \sigma}{d^2 kT}.$$

("NH," of course, denotes Nabarro–Herring.) Expressing this equation in the format of Equation 13.5 (making $\Omega = 0.7b^3$), we have:

$$\boxed{\dot{\varepsilon}_{\mathrm{NH}} = A_{\mathrm{NH}}\frac{D_\ell G b}{kT}\left(\frac{b}{d}\right)^2\left(\frac{\sigma}{G}\right).} \tag{13.12}$$

A_{NH} is typically equal to 10–15.

Coble proposed the second mechanism explaining diffusion creep.[10] It is based on diffusion in the grain boundaries instead of in the bulk. This diffusion results in sliding of the grain boundaries. Hence, if a fiducial scratch is made on the surface of the specimen prior to creep testing, the scratch will show a series of discontinuities (at the grain boundaries) after testing if Coble creep is operative.

Figure 13.11(b) shows, in a schematic manner, how the flow of vacancies along a boundary generates shear. Notice that there is also additional accommodational diffusion necessary. Coble creep leads to the relationship

$$\dot{\varepsilon}_C = A_C D_{\mathrm{gb}}\frac{G b}{kT}\left(\frac{\delta}{b}\right)\left(\frac{b}{d}\right)^3\left(\frac{\sigma}{G}\right), \tag{13.13}$$

where A_c is typically equal to 30–50, δ is the effective width of the grain boundary for diffusion, and D_{gb} is the grain-boundary diffusion coefficient.

Note that in Equations 13.12 and 13.13, the strain rate is proportional to the stress – that is, $n = 1$. Also, the strain rate goes as d^{-2} for Nabarro–Herring creep and as d^{-3} for Coble creep. This enables researchers to differentiate between the two mechanisms: they establish the creep rates for specimens with different grain sizes and find the exponent on the grain size. A practical way of having an alloy with high resistance to Nabarro–Herring or Coble creep is to increase the size of the grains. This method is used in superalloys; a fabricating technique called *directional solidification* has been developed to eliminate virtually all grain boundaries perpendicular and inclined to the tensile axis.

[10] R. L. Coble, *J. Appl. Phys.*, 34 (1963) 1679.

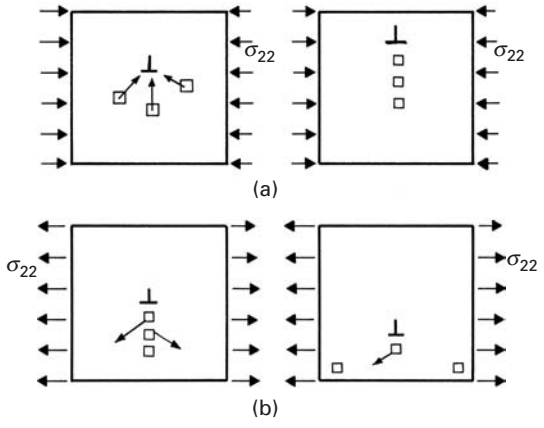

Fig. 13.12 Dislocation climb (a) upward, under compressive σ_{22} stresses, and (b) downward, under tensile σ_{22} stresses.

Harper and Dorn observed another type of diffusional creep in aluminum.[11] This occurred at high temperatures and low stresses, and the creep rates were over 1,000 times greater than those predicted by Nabarro–Herring. (Also, little Coble creep was observed.) The two researchers concluded that creep occurred exclusively by dislocation climb.

Dislocation climb is shown schematically in Figure 13.12. Under compressive loads, vacancies are attracted to the dislocation line (Figure 13.12(a)). Once a row of vacancies has joined the dislocation line, the line is effectively translated upward. Thus, the dislocation moves perpendicular to the Burgers vector during climb. In tension (Figure 13.12(b)), the opposite occurs: Vacancies move away from the dislocation line, and the dislocation effectively moves down.

Harper–Dorn creep is governed by an equation of the form

$$\dot{\varepsilon}_{\mathrm{HD}} = A_{\mathrm{HD}} \frac{D_\ell G b}{kT} \left(\frac{\sigma}{G}\right). \tag{13.14}$$

The parameter A_{HD} is typically equal to 10^{-11}. Since no grain boundaries are involved in this creep, the grain size does not appear in the equation. For Harper–Dorn creep to make a significant contribution, the grain size of the material has to be large (>400 μm); otherwise, Nabarro–Herring and Coble creep dominate.

In metals, Harper–Dorn creep has been observed in a number of systems. In ceramics, there is little evidence for this type of diffusion creep mechanism. Ceramics in general have small grain sizes, which favor other creep mechanisms. The stable, small grain size and the limited number of slip systems, as well as high Peierls–Nabarro stress, lead to the prominence of Nabarro–Herring and Coble creep. Diffusion in ceramics is more complex than in metals, because either one or two ionic species might participate, and in the case of multicomponent ceramics, more than one cation or ion might be involved. Figure 13.13 shows the different domains of creep in alumina as a

[11] J. Harper and J. E. Dorn, *Acta Met.*, 5 (1957) 654.

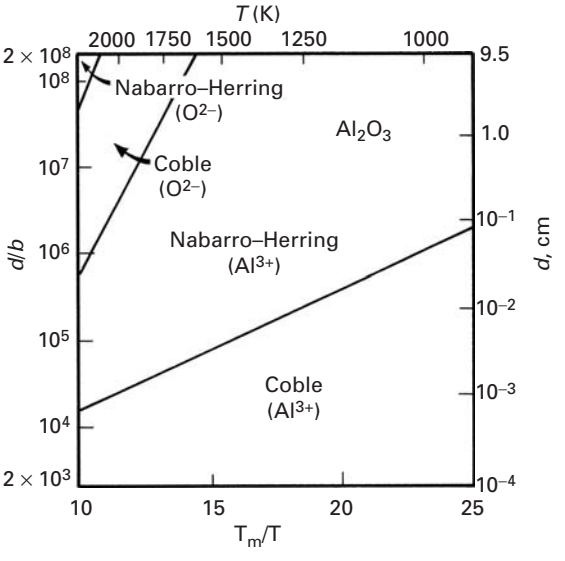

Fig. 13.13 Different regimens for diffusion creep in alumina; notice that cations (Al^{3+}) and anions (O^{2-}) have different diffusion coefficients, leading to different regimes of dominance. (From A. H. Chokshi and T. G. Langdon, *Defect and Diffusion Forum*, 66–69 (1989) 1205.)

function of grain size and temperature; the main ion is shown for each domain.

13.5 Dislocation (or Power Law) Creep ($10^{-4} < \sigma/G < 10^{-2}$)

In the stress range $10^{-4} < \sigma/G < 10^{-2}$, creep tends to occur by dislocation glide aided by vacancy diffusion (when an obstacle is to be overcome); this is called dislocation creep. This mechanism should not be confused with Harper–Dorn creep, which relies exclusively on dislocation climb. Orowan proposed that creep is a balance between work-hardening (due to plastic strain) and recovery (caused by exposure to high temperatures). Hence, at a constant temperature, the increase in stress is

$$d\sigma = \left(\frac{\partial \sigma}{\partial \varepsilon}\right) d\varepsilon + \left(\frac{\partial \sigma}{\partial t}\right) dt, \tag{13.15}$$

where $(\partial\sigma/\partial\varepsilon)$ is the rate of hardening, and $(\partial\sigma/\partial t)$ is the rate of recovery, of the material. The strain rate $\dot{\varepsilon}$ can be expressed as a ratio between the rate of recovery and the rate of hardening.

In the mid-1950s, Weertman developed a pair of theories of the minimum creep rate based on dislocation climb as the rate-controlling step.[12] In his first theory, Weertman presented Cottrell–Lomer locks as barriers to plastic deformation; his second theory applies to HCP metals, in which these barriers do not exist. Hence, he assumed different barriers, depending on the material. Figure 13.14 shows schematically how the mechanism based on Cottrell–Lomer locks operates. Dislocations are pinned by obstacles, but overcome

[12] J. Weertman, *J. Appl. Phys.*, 26 (1955) 1213; 28 (1957) 362.

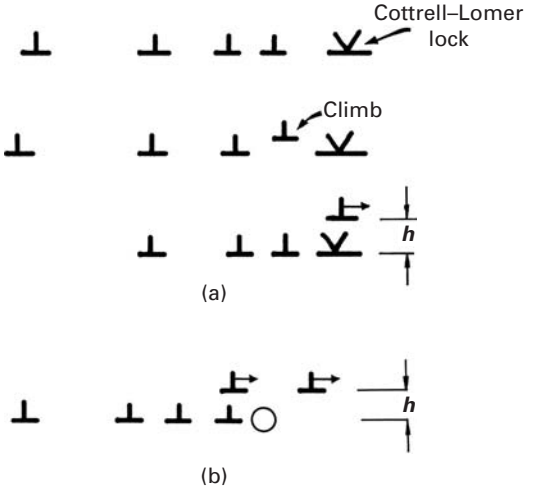

Fig. 13.14 Dislocation overcoming obstacles by climb, according to Weertman theory. (a) Overcoming Cottrell–Lomer locks. (b) Overcoming an obstacle.

them by climb, aided by either interstitial or vacancy generation or destruction. The obstacles are assumed to be Cottrell–Lomer locks, which are formed by dislocations that intersect and react. (See Section 4.4.6.) Figure 13.14(a) shows dislocations pinned between the locks and climbing over them. Note that dislocations are continuously generated by the Frank–Read source in the horizontal plane, and the ones overcoming the obstacle are replaced by others. To calculate the creep rate, we have to find the rate of escape of the dislocations from the locks. The height h a dislocation has to climb in order to pass through a lock is the position at which the applied stress on the dislocation, owing to the other dislocations in the pileup, is equal to the repulsive force due to the stress field of the lock. Other obstacles (shown in Figure 13.14(b)) can have the same effect.

The stress exerted by a dislocation due to the pileup effect is given in Section 4.4.9 and is (Equation 4.26a):[13]

$$\sigma^* = \tilde{n}\sigma, \tag{13.16}$$

where $\tilde{n}$ is the number of dislocations in the pileup (we use $\tilde{n}$ here to avoid confusion with n, the exponent in power-law creep) and σ is the stress applied on one dislocation. Now, taking the stress field around a dislocation as a function of distance (Section 4.4.3) and equating it to Equation 13.16, Weertman arrives at (this is slightly different from Equation 4.12)

$$h = \frac{Gb}{\tilde{n}\sigma 6\pi(1-\nu)}. \tag{13.17}$$

The rate of climb is determined by the rate at which the vacancies arrive at or leave the dislocation. (Weertman did the derivation for vacancies and not interstitials.) For the concentration gradient of vacancies, Weertman obtained a rate of climb

$$r = \frac{N_0 D_\ell \tilde{n}\sigma b^5}{kT}, \tag{13.18}$$

[13] Shear stresses were converted into normal stresses.

when $(\tilde{n}\sigma b^3)/kT < 1$. N_0 is the equilibrium concentration of vacancies and D_ℓ is the diffusion coefficient at the test temperature T. With a known climb height and rate of climb, it is possible to calculate the rate of creep. If M is the number of active Frank–Read sources per unit volume, L is the distance the edge portion of a dislocation loop moves after breaking away from a barrier, and L' is the portion the screw moves, then the creep rate is given by

$$\dot{\varepsilon} = \frac{r}{h} LL'M = \frac{6\pi(1-\nu)\tilde{n}^2 b^4 N_0 L\, L'\, M\, D_\ell \sigma^2}{kG\,T}. \tag{13.19}$$

If we assume, to a first approximation, that $\tilde{n}$, the number of dislocations in a pileup, and M, the number of Frank–Read sources per unit volume, are proportional to σ, we can recast Equation 13.19 in the Mukherjee–Bird–Dorn format as

$$\dot{\varepsilon} = A\left(\frac{D_\ell G\, b}{kT}\right)\left(\frac{\sigma}{G}\right)^5.$$

The stress exponent 5 is characteristic of this regimen. The term A incorporates the various parameters and proportionality coefficients. Power law creep with $n \approx 5$ has been observed at high stress levels in a number of ceramics, including KBr, KCL, LiF, NaCl, NiO, SiC, ThO_2, UC, and UO_2. (See Figure 13.4(b).) As in the case of metals, the substructure is characterized by subgrains with misorientations of approximately 2°.

Creep behavior with a stress exponent $n \approx 3$ is observed in a number of ceramics, such as Al_2O_3, BeO, Fe_2O_3, MgO, and ZrO_2 (+ 10% Y_2O_3). In this case, few or no solutes are present, and those that are do not play a role.

Dispersion-strengthened alloys are characterized by an exponent higher than 7 and by a high activation energy for creep. Dispersoids (see Chapter 10) are stable up to very high temperatures. Small particles, such as Y_2O_3 and ErO_2, are added to the alloy as dispersoids; this increases the high-temperature capability of these materials substantially, and the dispersoids act as effective barriers to dislocation motion.

Particle-reinforced composites (such as SiC and aluminum reinforced with aluminum oxide) exhibit the same effects: The stress exponent n and activation energy for creep are very high. This is illustrated in Figure 13.15, for an Al–30% SiC composite. The slope in Figure 13.15 is given by

$$n = \frac{\partial \ln \dot{\gamma}}{\partial \ln \tau} = \frac{\partial \ln 2\dot{\varepsilon}}{\partial \ln \sigma/2} = \frac{\partial \ln \dot{\varepsilon}}{\partial \ln \sigma}.$$

Taking logarithms and derivatives of both sides, we have (at constant T)

$$\begin{aligned} \dot{\varepsilon} &= A'\left(\frac{\sigma}{G}\right)^n = A''\sigma^n, \\ \ln \dot{\varepsilon}_s &= \ln A'' + n \ln \sigma, \\ \partial \ln \dot{\varepsilon}_s &= n\partial \ln \sigma, \\ n &= \frac{\partial \ln \dot{\varepsilon}_s}{\partial \ln \sigma}. \end{aligned}$$

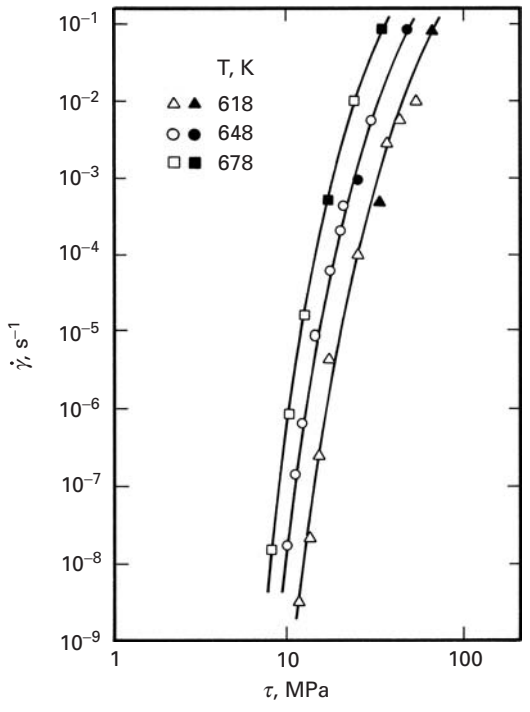

Fig. 13.15 Shear stress vs. shear strain rate in an aluminum (6061) with 30 vol.% SiC particulate composite in creep. (From K.-T. Park, E. J. Lavernia, and F. A. Mohamed, *Acta Met. Mater.*, 38 (1990) 2149.)

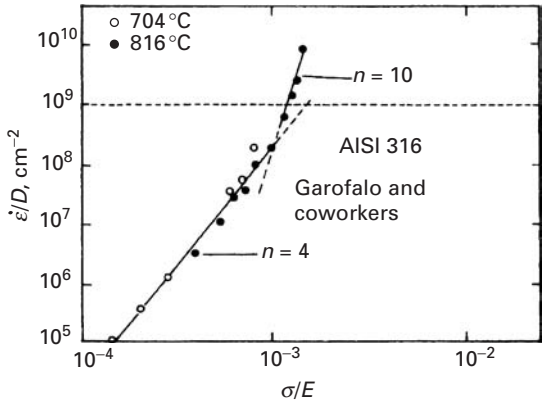

Fig. 13.16 Power relationship between $\dot{\varepsilon}$ and σ for AISI 316 stainless steel. (Adapted with permission from S. N. Monteiro and T. L. da Silveira, *Metalurgia-ABM*, 35 (1979) 327.)

Thus, the slope is equal to the stress exponent. In Figure 13.15, the slope n varies from 14.7 to 7.4 as the stress is increased. The activation energy for creep for this aluminum composite has a value of 270–500 kJ/mol; this is significantly higher than the activation energy for aluminum self-diffusion.

13.6 Dislocation Glide ($\sigma/G > 10^{-2}$)

Dislocation glide occurs for $\sigma/G > 10^{-2}$. At a certain stress level, the power law breaks down. Figure 13.16 presents the region in which the law ($n = 4$) breaks down, and n increases to 10; this occurs for $\dot{\varepsilon}_s/D > 10^9$. An analysis of the deformation substructure by transmission electron microscopy and showed that, at high stresses, dislocation

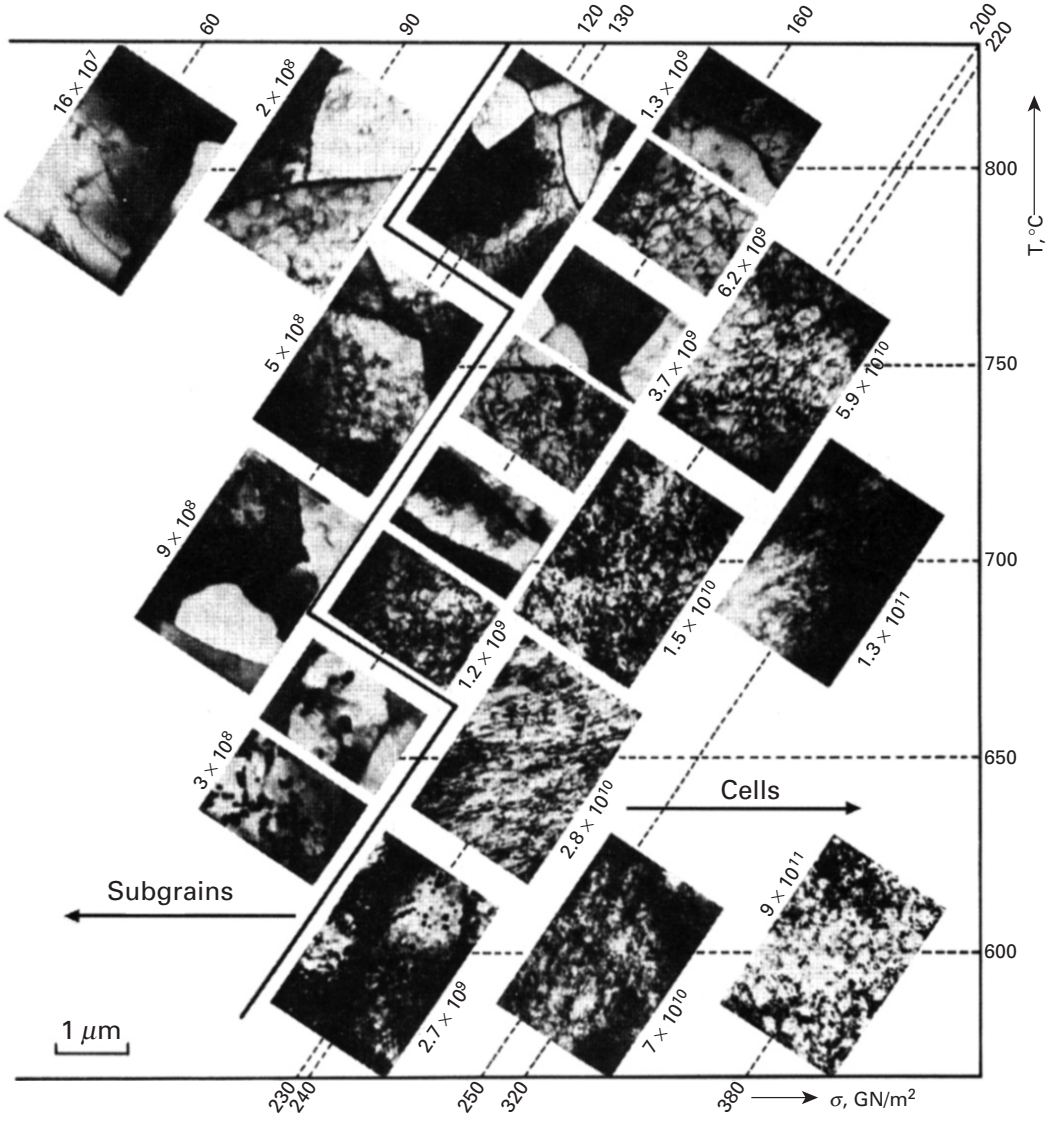

Fig. 13.17 Effect of stress and temperature on deformation substructure developed in AISI 316 stainless steel in middle of stage II. (Reprinted with permission from H.-J. Kestenbach, W. Krause, and T. L. da Silveira, *Acta Met.*, 26 (1978) 661.)

climb was replaced by dislocation glide, which does not depend on diffusion.[14] Hence, when $\dot{\varepsilon}_s/D > 10^9$, thermally activated dislocation glide is the rate-controlling step; this is the same deformation mode as the one in conventional deformation at ambient temperature. Kestenbach et al. observed that the substructure changed from equiaxial subgrains to dislocation tangles and elongated subgrains when the stress reached a critical level. A similar effect is observed when the temperature is decreased and the stress is maintained constant. Figure 13.17 shows the substructures at various values of stress and temperatures for secondary creep.

[14] H.-J. Kestenbach, W. Krause, and T. L. da Silveira, *Acta Met.* 26 (1978) 661.